EXPANDING VORTEX TRAPPING AND ELECTROPORATION CAPABILITIES TO SMALL CELLS

by

Srivathsan Kalyan

A dissertation submitted to Johns Hopkins University in conformity with the requirements for

the degree of Doctor of Philosophy

Baltimore, Maryland

October 2022

Abstract

Microfluidic Vortex devices have been commercialized for purifying rare circulating tumor cells from patient samples, enriching these rare cells by up to a 100,000-fold. These purified, viable cells can then be interrogated through live-cell assays and genetic sequencing, giving clinicians valuable insight into patient disease state and potential treatment directions. Vortex devices can also be integrated with solution exchange and electropermeabilization for on-chip susceptibility assays and biomolecular delivery. Currently these devices are limited to particles larger than 15 µm in diameter. In the biological field, cell separation and integrated electroporation is valuable for the biomolecular delivery to lymphocytes (7-9 µm), spermocytes (7-8 µm), and stem cells (~10 µm). In the pharmaceutical industry, separation integrated with solution exchange for modifying surface properties of drug microparticles (< 10 µm). These exemplify the need to expand Vortex device capabilities particles in the 7-10 µm range.

In Chapter 1, we provided background information on Vortex separation devices and integration with other functionalities.

In Chapter 2, we expanded Vortex separation capabilities, to microparticles 7-10 µm by manipulating device geometry and operational conditions. We tested device performance with polystyrene microparticles and living cells. We show that our novel trapezoidal chamber with a narrowing channel leads to a 4-fold increase over tested rectangular chambers when trapping microparticles in the 7-10 µm size range.

In Chapter 3, we confirmed that our new cell trapping device retains the capability of integrated electroporation. We designed serrated electrodes to electroporate smaller cell by

amplifying the electric field strength, without significant electrolysis. Next, we use real-time fluorescent measurement and cell viability and electroporation efficiency analysis to identify electroporation conditions for biomolecular delivery of fluorescent dye to small 7-10 μm cells.

The device discussed Chapters 2 and 3 expand the capabilities of Vortex trapping with integrated electroporation functionality. If optimized, the presented platform could potentially perform electroporation-mediated biomolecular delivery to cells in the 7-10 μm size range, with therapeutic applications to lymphocyte, sperm, and stem cell engineering.

Chapters 4-6 discuss contributions to the commercialization of electrode-integrated microfluidic devices, the development of tunable microfluidic phantoms, and inertial microfluidic devices for sorting retinal ganglion cells.

Thesis Committee

Primary Reader

Dr. Soojung Claire Hur

Assistant Professor, Department of Mechanical Engineering, Johns Hopkins University

Secondary Readers

Dr. Ishan Barman

Associate Professor, Department of Mechanical Engineering, Johns Hopkins University

Dr. Luo Gu

Assistant Professor, Department of Material Science and Engineering

Acknowledgements

The work in this document is a culmination of not only my efforts, but efforts of lab mates, collaborators, and my support system, both in and outside of Baltimore, that helped me along the way and believed in me the entire time. I would like to extend a huge thank you to those people.

First, my lab mates, who made my time in Baltimore extremely enjoyable, both in and out of lab. They are amazing people and I have had the utmost pleasure working with them, learning from them, and growing as a person and as a scientist.

Second, I would like to thank my collaborators. Dr. Gregory McKay, Dr. Nathan Scott, and Cynthia Berlinicke, all introduced me to new fields of science, with completely new challenges and that captivated my interest and made me want to become a more well-rounded scientist.

Third, I would like to thank my committee members for their time and guidance during my Ph.D. I am grateful for their support, in both my scientific and career aspirations. They have helped me look at my work through different perspectives and given me great advice in tough times.

Lastly, I would like to thank Prof. Soojung Claire Hur. She has tirelessly dedicated herself to helping me grow as a scientist, and has always made herself available to help me during my Ph.D. Her understanding, patience and dedication to science are qualities that I aspire to.

Dedication

To my friends in Baltimore, thank you so much for making my first long term excursion outside of California enjoyable, and not at all scary! I know some of these friendships will continue over my lifetime and beyond, and I will continue to cherish them.

To my parents, Kalyana Sundaram and Susheela Ramaswamy, thank you so much for always believing in me, and always reminding me to look at things as half-full and never half-empty. I would never have gotten this far without your help, and I am so thankful for you every day.

To my brother, Shreyas, you made it easy to move across the country, because you came with me. You were always available to chat or visit me and make everything better, and I really feel that we grew much closer through our experiences.

To my fiancé, Aathmika Krishnan, you have always been my rock, supporting me even when everything else is against me. You helped me find my focus in life, and will continue to be my guide, and my light. I would not be the person I am today without you. You have shaped me for the better and I look forward to our life together.

Table of Contents

List of Figures

Chapter 1. The Need to Expand the Capabilities of Microfluidic Vortex Trapping Devices

1.1. Introduction

1.1.1. The Need for Microparticle Separation

Microparticle separation and manipulation is a staple process step in many fields such as environmental sampling, agrochemicals, cosmetics, pharmaceuticals, and biological and clinical research. In environmental sampling, microparticles in samples need to be sorted to enrich target analyte concentration, to reliably detect potential biological weapons from aerosol samples [1]–[5] and biological hazards from agricultural products [4], [6], [7]. In the agrochemical, cosmetics, and pharmaceuticals industries, microparticle usually require some secondary modification or processing to reach their final product state [8]–[10]. In the agrochemical industry, it is common to fabricate a polydisperse solution of microparticles, used to spread pesticides [11] and fertilizers [8], [12]. However, pesticide and fertilizer microparticle spreading effectiveness is a function of particle size [13]. Thus, post processing of particles and separating them based on size is beneficial to ensure uniform results. Polymer particles in the cosmetic industry are of great interest for the treatment of facial lines [14], and design topical products such as lotion [10], [15]. However, these particles often require surface modifications to prevent undesirable reactions such as inflammation or contact dermatitis [10]. In the pharmaceutical industry, modifications of microparticles have been extensively used to enhance drug release times, targeted drug delivery, and bioavailability of drugs [16]–[18]. Biological and clinical research not only rely on the sorting and manipulation of inanimate microparticles, but also apply these processes to living cells. Target cells are often hidden amongst the background of millions of cells and require sample preprocessing to purify these cells. Contaminating cells can interfere with clinically relevant

1

procedures such as the diagnosis for diseases such as cancer [19], [20] and malaria [21], therapeutic predictive assays for cancer [22]–[25], and gene engineering as a therapeutic tool for diseases such as cancer [26]–[28] and HIV [29].

Within each field, specialized particle separation techniques have been developed and are certainly valuable. However, specialization constrains researchers from translating these processes freely across different fields. For example, a common method of microparticle separations in biology relies on cell surface markers [30]. However, these separation techniques are of little use in the agrochemical, cosmetics, and pharmaceutical industries where microparticle separation to processes are applied to inanimate microparticles. Thus, investigations into separation platforms that rely solely on common characteristics of microparticles, such as their physical properties and behavior under applied physical forces, such as hydrodynamic forces will have an amplified impact across different fields [31]–[33].

Another key consideration is the integration of additional functions within a device. Downstream functions such as impedance measurements (for size profiling) [34], [35], solution exchange for particle coating [33], [36], [37], and biomolecular delivery via electroporation (especially in the biological field) [38], [39] are often desirable or required post-separation processes. It is highly desirable for the same device to have the secondary functionality integrated with particle separation. This is because integration of these secondary functionalities will minimize the need for particle manipulation and handling [40], [41]. Thus, performing the required sample separation and post-processing on a single microscale device is efficient and economical.

One family of devices that rely solely on physical properties of microparticles and hydrodynamic forces for particle manipulation and has been successfully integrated with secondary functionalities is inertial microfluidic devices.

1.1.2. The Versatility of Inertial Microfluidics

Inertial microfluidic devices are a subclass of microfluidic devices that operate in laminar flow regimes, but at finite Reynolds numbers were inertial forces are significant [42]. These inertial forces, combined with particle confinement effects, cause two major lift forces to act on neutrally buoyant particles within the microfluidic channel – the shear gradient lift force (F_{SGL}) and the wall lift force (F_{WL}) [31]. These two forces act perpendicular to the flow and in opposing directions. The F_{SGL} forces directs particles towards the nearest channel wall, and F_{WL} directs particles towards the channel centerline [43]. The net lift forces acting on particles scale with particle size [32]. Critically, this means that particles of different sizes will focus to different equilibrium positions within a microfluidic channel. These differences in focusing positions are used to direct microparticles to different outlets, thus separating them [44]. Due to their separation mechanism, inertial microfluidic devices have been leveraged for a variety of uses across different fields. For example, investigations have targeted analytes from aerosolized and food samples[45]–[48], looking for pathogens and potential biohazards. Countless groups have used polystyrene microparticles as a proof of concept to test their designs and geometries [49]–[52], indicating the capability of inertial microfluidics to perform polymer microparticle separation. Finally, in biology, inertial microfluidics has been used to separate rare circulating tumor cells (CTCs) from a background of millions of blood cells [53]–[57], purify PBMCs and fractionate immune cells from whole blood [58]–[62], separate smaller sperm cells [63]–[66], extracellular

vesicles [61], [67]–[69], and pathogens from whole blood [70], [71], and even deplete blood samples of blood cells to separate plasma [72]–[74]. The flow regimes where these devices operate also allow for the rapid processing of samples, a critical feature that ensures the viability of cells.

While the versatility of these devices is unquestionable, the use of inertial microfluidics can be expanded. For this, devices with the ability to integrate other functionalities such as solution exchange to coat particles with different solvents, interrogate analytes for susceptibility to different drugs, or delivery of biomolecules to a target are attractive targets of investigation [38]. A subset of inertial microfluidics devices, known as Vortex trapping devices, offers the capability of integrating the promises of inertial microfluidics with other on-chip or inline functionalities [75]–[77].

1.1.3. Vortex Devices and the Need for Expansion

Vortex trapping is unique among inertial microfluidic devices because it allows the complete control over particle residence time, and because of its discrete capture and release steps. The control over particle residence time on-chip is critical for integrating the Vortex device with such functionalities such as multiple solution exchanges and biomolecular delivery via electroporation for cell engineering and susceptibility assays [76], [78]–[80]. The discrete capture and release steps allow captured cells to be released to inline downstream platforms with functionalities such as droplet generators for single cell encapsulation and studies [75], and impedance measurements for further morphological characterization of particles [77].

Vortex trapping uses inertial microfluidics to align microparticles within a microfluidic channel. Once focused, these particles enter an expanse region in the channel, called the Vortex trapping chamber. At high flow rates, a recirculation flow forms within this chamber [53]. Following streamlines, particles and fluid from the main channel is brought into the chamber. Particles are then trapped due to three main fluidic forces – hydrodynamic drag, particle inertia, and added mass [81]. The exact contributions of these forces remain unknown, but all three forces scale with particle size. As a result, Vortex trapping has only been investigated for its ability to trap large particles, greater than 15 μm in size [53]. However, there are other populations of smaller microparticles that can benefit from the advantages that Vortex trapping has to offer. In the pharmaceutical field, microparticle size is critical and directly affects bioavailability and drug efficacy, with particles less than 10 μm typically outperforming larger particles [82]. Water insoluble drug microparticles which could be targeted for further post processing, such as coating or surface charge modifications, are limited to 10 μm in size [83]. Glucose Oxidase microparticles of 4 μm in size were shown to be the most effective in killing breast cancer cells, compared to larger 26 and 146 μm particles [84]. Particles between 5-10 microns in size were shown to be the most effective for encapsulation into microspheres with modified surface properties that can be used for targeted delivery, or enhancing drug circulation time and efficacy [85]. In biology, cell populations such as lymphocytes [58], [86], spermatocytes [87], [88], and stem cells [89], [90] which are biomolecular delivery targets for therapeutic applications and fundamental biological studies are in the 7-10 μm range. Thus, there is a critical need to expand the capabilities of these versatile devices into the range of smaller particle sizes less than 15 μm.

Previous work has shown that by manipulating device geometry [75], [91] and operating conditions such as device flow rate [91], [92], we can manipulate the behavior of particles within vortex. While these investigations were still tailored towards efficiently trapping large particles greater than 15 µm in size, we can use them as starting points to design a device to trap smaller particles. For these investigations, a size range of interest in both the pharmaceutical and biological applications are microparticles within the 7-10 µm range.

1.1.4. Ensuring the Translation of Benefits to the New Purification Target

Vortex trapping devices were chosen as the focus of our investigations due to the ease of integration with on-chip and downstream capabilities such as solution exchange [53], drug susceptibility assays [78], [93], biomolecular delivery via electroporation [76], [79], [80], in-line impedance measurements [77] and droplet encapsulation [75]. In the work described in Chapter 2, we change a signature characteristic of the Vortex device – the size of particles that it targets, from particles > 15 µm to particles in the 7-10 µm range. It is therefore critical that we assess our new device for its ability to integrate with additional downstream functionalities without any adverse impact. Specifically, we chose to focus on electroporation as the downstream process to investigate for impact to its effectiveness.

Electroporation is the process of permeabilizing a cell by applying an external electric field and delivering biomolecules across the permeabilized cell membrane. This process has been used to successfully deliver a variety of biomolecules such as fluorescent dye, plasmids, DNA, mRNA, siRNA, and protein complexes [94] to the cell. The delivery of these molecules is relevant to vital investigative and therapeutic processes such as protein therapy [95]–[97] and genome editing [98]–[100].

In traditional electroporation, the cells to be permeabilized are loaded into a cuvette with the cargo of interest. These electrodes are typically on the order of millimeters apart. To permeabilize the cell, these devices require high voltages to produce an electric field capable of permeabilizing the cells, typically > 1 kV [38]. These high voltages are dangerous to the user, and lead to electrolysis, generating gas bubbles, hydroxyl ions, and hydrogen ions at the surface of the electrodes, creating a toxic environment for the cell [101]. Additionally, degradation of the electrodes releases toxic metal ions into the solution, further negatively impacting cell viability [102]. To address these concerns, microscale electroporation has become increasingly popular.

1.1.5. Microscale Electroporation

Microscale electroporation, in contrast to conventional cuvette electroporation, typically occurs within microfluidic devices, where the device dimensions are of the order of microns. Decreasing electrode spacing effectively reduces the required voltage to create the requisite electric field, as the electric field strength is given by:

$$E = -\nabla V \tag{1.1}$$

Here, E is the electric field and V is the applied voltage. The reduction of applied voltage minimizes hydrolysis and electrode degradation. The low voltage requirements also offer more flexibility in the design of the electric field generator, allowing for more control over the electrical signal used to create the field [103]. In addition, microscale electroporation offers superior control over cell manipulation and handling because both the cells and device features are on similar size scales [39]. Recent advances in microscale electroporation are extensively covered in this review [38].

Many microfluidic electroporation devices have been designed with the specific goal of cell electroporation only [39], [104]. However, the integration of electroporation as an additional functionality to a microfluidics device enhances the versatility of the device. For example, one study developed a microfluidic chip to culture primary cells and electroporate them, overcoming challenges associated with suspending primary cells [105]. Another study performed single cell electroporation on myoblasts and monitored protein expression and dynamics as a result of stimulation factors, thus offering single cell analysis of transfected cells [106]. These studies show that by integrating electroporation with microfluidic devices as an additional functionality, the potential impact of the device can be amplified.

1.1.6. Integration of Vortex Trapping and Electroporation

Integration of electrodes onto the Vortex trapping chip transformed a cell separation device into a versatile electroporator. The benefits of integrating these two functionalities overcame challenges of handling and manipulating rare cells, within a live temporal window [79]. These devices have previously been used to deliver a range of biomolecules such as therapeutic agents [78], fluorescent dye [76], [79], [80], plasmids [76], [80], proteins [80], siRNA [80], and mRNA [80]. Integrating electroporation with a device that separates cells based on size has the additional benefit of more uniform electroporation results. The equation that governs electroporation is:

$$\Delta V_{tm} = f * E_{ext} * r * cos(\theta) \tag{1.2}$$

where V_{tm} is the transmembrane potential across the cell membrane, f is an adjustment factor with a value of 1.5 for spherical cells, E is the applied electric field, r is the radius of the cell, and

θ is the angle between the electric field and a point on the cell. In this equation, both V_{tm} and f are constant for mammalian cells, and have values of 200 mV and 1.5, respectively [107]. The magnitude of the electric field required is hence inversely proportional to the cell radius. As Vortex trapping is a size-based method of cell separation, previous results show a homogenous size of cells to be electroporated [76], thus leading to high efficiencies.

This also leads to the challenge in integrating our new Vortex device with electroporation. The target population for the new device are cells in the range of 7-10 μm in diameter, which are smaller than cells targeted by the previous Vortex-electroporation device [54], [92].

1.1.7. Thesis Outline

The work reflected in this thesis is the culmination of the work I performed at Johns Hopkins University, alongside my colleagues and collaborators.

In Chapter 2, we investigate ways to expand the uses of vortex trapping by changing the device geometry and operating conditions and show that Vortex devices can be used to trap smaller microparticles in the 7 – 10 μm range.

In Chapter 3, we describe how we manipulated the electric field strength and used a combination of real time electroporation assessment and post-collection analysis to determine gentle conditions for electroporation of cells targeted by our new vortex device.

In Chapter 4, we investigate a new electrode-integrated Vortex device fabrication pipeline using hot embossing and electroplating. Additionally, we miniaturized the electric field generator which provides the electric field required to electroporate cells. These investigations aimed to make the electrode-integrated Vortex devices more commercialization friendly [40], [108].

In Chapter 5, we investigate the fabrication of a microfluidic phantom, with tunable properties to mimic optical properties of tissue. This novel fabrication technique allows us to image blood flow through microchannels, under a think membrane with tissue-like optical properties to simulate imaging capillaries *in vivo* [109], [110].

In Chapter 6, we investigate an inertial microfluidic deformability-based sorting device for its ability to purify retinal ganglion cells (RGCs) from a heterogeneous population. Using an inertial microfluidic device that can purify these target cells in a label-free manner would allow for their use in clinical applications, such as cell replacement therapy, to treat glaucoma [111].

Finally, we finish with a conclusion that gives us direction on the integrated Vortex trapping electroporator system, and a summary of what we accomplished in the Chapters 4-6.

Chapter 2. New Geometry Expands Vortex Capabilities to Smaller Particle Populations

2.1. Introduction

Microparticle separation is an important technology in many fields such as ceramics, polymers, and biological research [112]. Each field has developed specialized methods of particle separation based on sample- and field- specific constraints (for example, cell viability requirements in biological research), but a common separation criterion in all listed fields is microparticle size [113]–[115]. In ceramic and polymer microparticle research, microparticles have different characteristics (such as drug diffusion coefficients) based on their size [116]. However, fabrication processes for ceramic and polymer microparticles result in particles with a polydisperse size distribution [117]. Particle separation steps are performed serially using sieves or membranes with specific pore sizes, thus separating particles into homogeneous subpopulations. While this is a well-established protocol requiring minimal optimization, the unwanted particles accumulate and clog the pores, leading to contamination of the final product and lower throughput [118]. In biological research, samples often require preprocessing to concentrate analytes such as circulating tumor cells (CTCs) and pathogens from backgrounds of millions of blood cells. Critically, the analytes of interest are often different sizes than the background cells. CTCs are larger than 15 μm, compared to smaller red blood cells, white blood cells, and platelets (which range between 5-15 μm in diameter) [119]. Bacterial pathogens, such as *Escherichia coli* (*E. coli*), are between 1-2 μm in diameter [120]. Size based separation methods implemented in microfluidic devices have successfully been used to separate CTC's [121] from

11

blood with a 100-fold increase in purity, and capture living parasites [122] from blood with > 99% purity. However, these devices operate at low flow rates (< 100 uL/min), and often require long processing times to process relevant sample volumes (~10 mL) [123], possibly affecting cell viability.

One method of separating particle based on size, with minimal sample handling and high throughput is inertial microfluidics. Inertial microfluidic devices use hydrodynamic forces and particle properties to differentially focus particles at distinct locations within a microfluidic channel. Based on particle locations, different subpopulations can be directed to different outlets, thus separating them. Inertial microfluidic devices have risen to the forefront of particle separation processes due to their high throughput and versatility [31], [33], [124]. Their high throughput capability allows for large volume processing in short time [33], while their versatile sorting mechanism allows for their use in sorting different particle populations, with minimal sample handling. Previously, inertial microfluidic devices have been used to separate heterogeneous polymer microparticle populations into homogeneous sized subpopulations [32], [52], [112], [125], [126]. In environmental sampling, inertial microfluidics is used to remove contaminating dust and background food particles to concentrate analytes such as pathogens and bacteria for detection and characterization [45], [47]. In biological research, inertial microfluidics has been used to sort rare cells from biological samples, concentrating target analytes such as CTC's and pathogens from millions of background cells for more reliable downstream assays [54], or separating subpopulations of white blood cells for further morphological characterization, used in diagnosis of diabetes [57], [61], [72].

The versatility of inertial microfluidic separation can be further increased by integrating the particle separation platform with other functionalities. For example, some functionalities of interest are inline functionalities such as droplet generation for single cell studies [48] and impedance measurements for further morphological characterizations [50]. These functionalities can be added as a post-processing step to inertial microfluidic devices with discrete capture and release steps. Additional on-chip functionalities such as drug synergy assays [51], [52], susceptibility assays [81], and biomolecular delivery [49], [53], are enabled by rapid exchange of multiple solutions on-chip. These functionalities can be integrated with inertial microfluidic platforms that can precisely control particle residence time. A unique family of inertial microfluidic devices that offer both discrete capture and release steps (enabling inline functionalities), as well as control over particle residence time (enabling on-chip functionalities) is the Vortex device family.

Vortex devices have been previously used to purify large polymer and biological particles with diameters greater than 15 μm [53], [54]. These devices use inertial microfluidics to focus particles in a microchannel. The microchannel suddenly expands to a rectangular reservoir and a recirculation flow forms within this reservoir. The boundary between the main channel flow and the recirculation flow is known as the separatrix. The behavior of the separatrix is governed by the channel Reynolds number (Re$_c$), which is given by the equation $Re_c = \frac{\rho U_{Avg} D}{\mu}$, where ρ is the fluid density, U$_{Avg}$ is the average fluid velocity, D is the hydrodynamic diameter of the channel, and μ is the dynamic viscosity of the fluid [81]. At high Re$_c$ (> 75), the separatrix breaks down and allows fluid streamlines and mass to transfer into the recirculation flow from the main channel. Particles are brought into the recirculation flow due to inertial migration forces and streamline

13

curvature [127]. However, when the fluid exits the reservoir again, particles remain trapped within the recirculation flow, due to a combination of hydrodynamic forces such as drag, particle inertia, and added mass [81]. While the exact contributions of each of these forces remain unknown, all forces scale with particle size, which enables this device to selectively trap large particles (D > 15 μm).

There is a real need to expand these benefits to different target particle populations, D < 15 μm in diameter. For instance, in the pharmaceutical industry, drugs with poor water solubility are often delivered *in vivo* in polymer particles smaller than 10 μm [83]. However, these microparticles are fabricated using methods that result in heterogeneous particle sizes, and require post-fabrication purification to obtain homogeneous particle sizes [117]. Purification of these particles using Vortex trapping is only possible if we expand Vortex capabilities down to this size. Furthermore, microparticles used for drug delivery often require secondary processing, such as layer-by-layer particle coating, which can be performed by multiple solution exchange steps, possible on Vortex trapping devices [128], [129]. In biology, populations of cells ranging between 7-10 μm, such as lymphocytes [60] can benefit from Vortex trapping's on-chip benefits such as biomolecular delivery to perform cell engineering for cancer therapeutics [130] and downstream applications such as droplet encapsulation for single cell studies [131], [132]. Spermatocytes (7-9 μm) can benefit from the integrated functionalities of cell separation [87] and cell electroporation [133].Thus, expanding Vortex capabilities to different populations will increase the presence of these devices.

The geometry of Vortex trapping devices and its effect on the trapped particle population has been studied extensively to target large particles (D > 15 μm). Previous work has shown that,

by narrowing the microfluidic channel width and shortening the channel height, we can trap more particles in the 15 – 20 µm range, thus increasing capture efficiency. The downside to this is particles in the 12 - 15 µm range are also trapped, which sacrifices purity [134]. Another investigation found that by increasing Re_c, we can decrease the average size of trapped particles, from an average of 35 µm at Re_c = 125 to an average of 22 µm at Re_c = 275 [92]. While these studies were still limited to targeting particles 15 µm in diameter or larger, these results show that by changing device geometry, operating conditions affect the size of particles trapped in the chamber. These results show that the particle population trapped within the Vortex device, and the behavior of trapped particles depend on these parameters, and by modifying them further, we could potentially trap particles within our target 7 – 10 µm size range.

In this work, we designed a Vortex device to trap polystyrene beads in the 7 – 10 µm range. This size range has not been previously targeted by Vortex separation methods and is significant because polymer and drug microparticles that can benefit from secondary vortex functionalities, such as layer-by-layer particle coating, exist in these size ranges [129], [135]. It also overlaps with cell sizes such as lymphocytes [86] and spermatocytes [87], and stem cells [89] which are of clinical relevance as therapeutic options for cancer [136]–[138] and HIV [29], [139] treatment, assistive reproductive technology [133], [140], and allogenic corneal transplants [90], respectively. Lastly, we tested our device with L1210 cells which have an average diameter of 10.1 ± 1.4 µm, to purify cells within our prescribed size range from wide inlet size distribution. We believe that this work is a critical step to expanding the capabilities of Vortex trapping and applying this technology to particles in different size distributions.
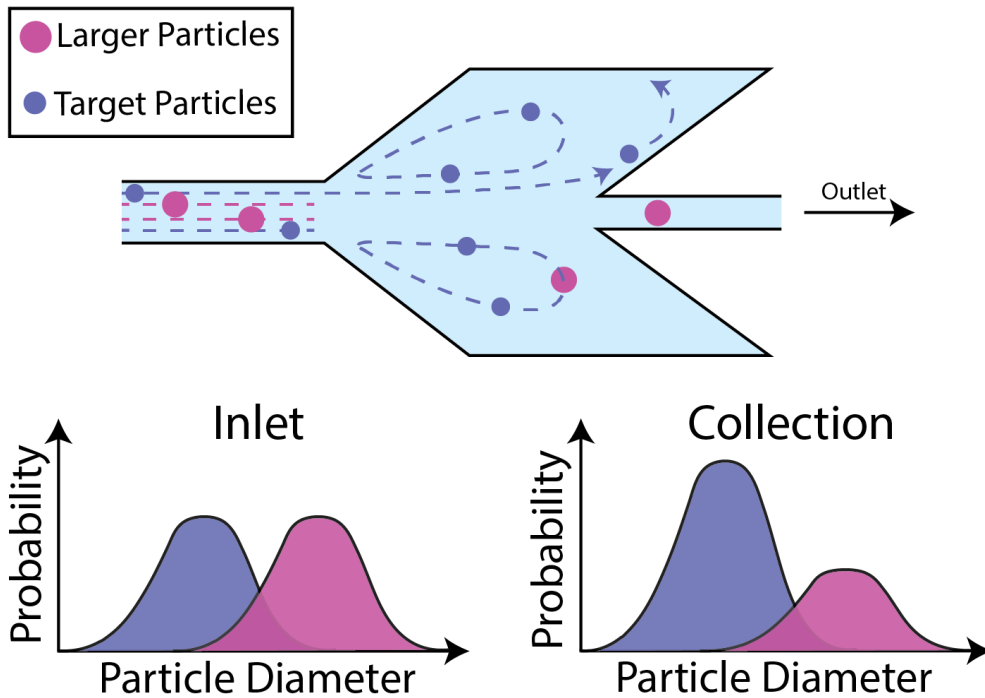
Figure 2.1: Overview of the device. (Top) A heterogeneous population is an input into the device with target particles and larger contaminating particles. We see that before the chamber, the particles are aligned into distinct streamlines based on their diameters. Once the particles reach the reservoir, target particles are more likely to populate the trapping chamber. (Bottom) representative graphs depict how we expect the device to perform. We are targeting particles at the smaller end of the distribution and expect them to be enriched amongst the trapped population for final collection.

2.2. Materials and Methods

2.2.1. Device Geometry

We designed and tested devices of varying dimensions. The final device has a trapezoidal chamber attached to a microfluidic channel. The inlet to the trapping chamber is a rectangular channel with dimensions of 25 μm x 35 μm ($W_{C,1}$ x H) and a length of 1,640 μm. At the outlet of the chamber, the channel contracts to 15 μm x 35 μm ($W_{C,2}$ x H_C), linearly increasing in width back to 25 μm over 500 μm. The chamber itself is a trapezoid on either side of the channel, each measuring 650 μm x 275μm (Ch_L x Ch_D). The trailing wall of the chamber forms a 30° angle with the wall of the channel.

2.2.2. Device Fabrication

The microfluidic device was fabricated using standard soft lithography. Briefly, a photomask was designed using AutoCAD (Autodesk, USA) software and printed (CAD/Art Services, Inc, USA). In a clean room, a negative photoresist (KMPR 1050, Kayaku Materials, USA) was spin-coated onto a four-inch silicon wafer (University Wafers, USA). The pattern was then transferred from the photomask using > 365 nm UV light. The uncured photoresist was washed away in a SU-8 Developer (Kayaku Materials, USA) bath for 6 minutes. The mold was then hard baked at 200°C for 20 minutes, and polydimethylsiloxane (PDMS, Dow Corning, USA) was cast onto it, creating the channels. PDMS was mixed in a 10:1 base to curing agent ratio, degassed for 15 minutes, and allowed to cure overnight at 80°C. The solution injection and outlet ports were created using hole punches (Pin Vise Set A, 20 punch gauge, Syneo, USA). The PDMS chip was then bonded to a microscope slide (Histobond, USA) after exposure to O_2 plasma at 0.3 Torr and 75 W for 45s.

2.2.3. Cell Preparation

L1210 cells (ATCC, USA) were grown in Dulbecco's Modified Eagle Medium (Corning, USA) supplemented with 10% horse serum (Millipore Sigma, USA), and 1% penicillin-streptomycin (ThermoFisher, USA). The cells were incubated in a humidified incubator kept at 37° C and 5% CO_2. Cells were harvested after two days and diluted to a concentration of 25k/mL for experiments.

2.2.4. Particle Imaging and Size Distribution Measurements

To evaluate device performance with polystyrene beads, we created 25k/mL solutions of polystyrene particles (Phosphorex, USA) suspended in PBS (Corning, USA). Cells were suspended

in their respective growth media. The solution was injected into the device using a syringe pump (Harvard Apparatus, PHD 2000).

Trapped particles were imaged using a highspeed camera (The Phantom1 v1210, Vision Research Inc., USA). We used an image processing code to analyze the recorded high-speed videos and obtain particle size information. Inlet data was obtained by imaging a sample of the solution in a well plate and processed using the same image processing algorithm. The code was validated by measuring particle sizes from images and comparing those from Scepter Cell Counter (Millipore Sigma, USA) (Figure 2.2).
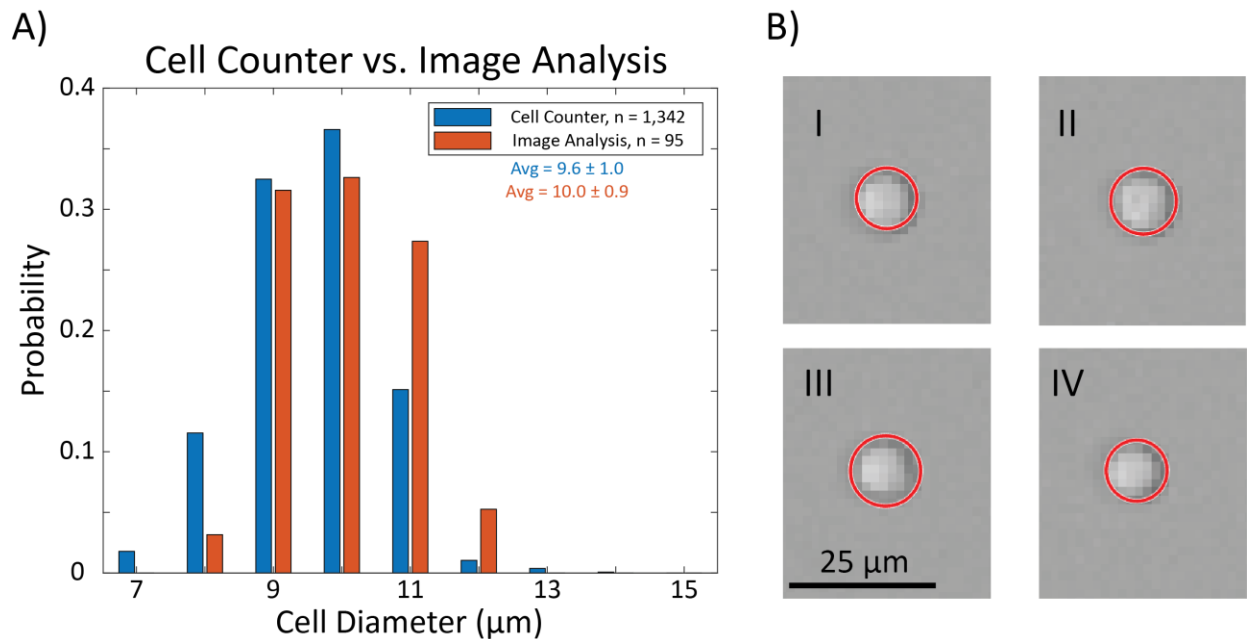
Figure 2.2: Graph comparing the diameter measurements using the Scepter Cell Counter and the image analysis code, as well as sample measurements from the image analysis code. A) shows the particle distribution using both measurement methodologies. The difference in the average is 0.4 μm, and the distributions are similar, as confirmed by a QQplot. B) shows sample cell measurements using the image analysis code for cells with diameters of I. 9.9 μm, II. 10.7 μm, III. 11.3 μm, IV. 9.9 μm.

2.2.5. Solution Exchange and Cell Viability Analysis

Similar to the solution exchange steps described previously [76], [78], [80], a custom-built pressure regulator was used to control the flow of solutions into the device. Python-controlled solenoid valves regulated the flow of nitrogen (Airgas, USA) to pressurize 3 hermetically sealed 50 mL conical tubes. These tubes, each containing a PBS wash solution, a 15 µM propidium iodide (PI) solution, and the final collection media, were connected to the device via PEEK tubing (IDEX, USA) and an inline check valve (IDEX, USA). The cell solution was input into the device from a syringe using a standard infuse/withdraw pump (Harvard Apparatus, PHD 2000, USA). The syringe was connected to the device using PEEK tubing and a shutoff valve assembly (IDEX, USA). The operational pressure of the device was 60 PSI, which translates to a flow rate of 210 µL/min. Initially, the device was fully primed with PBS at 60 PSI. DAPI stained cells were then co-injected into the device, at a flow rate of 100 µL/min, for 50 seconds, followed by a withdraw step at a flow rate of 50 µL/min for 20s. This withdraw step was critical in ensuring that cells did not contaminate the inlets of the other solutions. Every solution exchange step thereafter was performed by co-flowing the initial and the target solution, at 60 PSI for 20 seconds. This overlap ensured a continuous flow rate, which kept the cells stably trapped within the reservoir. After 20s, the initial solution was turned off, and the cells were suspended in the target solution. The solution order was PBS for initial capture and wash, PI to stain the dead cells, then media for final rinse and collection. To collect the cells, the pressure was lowered to 20 PSI for 20 seconds, then increased back to 40 PSI. Approximately 75 µL of solution was collected after each trial. The collected cells were then stained with 1 µM of Calcein-AM, and imaged. The images were

analyzed using a custom image processing pipeline using CellProfiler and Python Spyder IDE to obtain cell viability information.

2.3. Results

2.3.1. The Need to Change the Mechanism of Particle Trapping

We initially evaluated rectangular devices for their ability to trap small particles (D = 7-10 µm). For these experiments, we chose to test our devices with D_{Avg} = 10 µm polystyrene microparticles. Measurements of particle sizes showed that in the inlet population, particles ranged from 7-13 µm (Figure 2.2). The goal was to identify a device that could enrich the population of microparticles within the 7-10 µm range by selectively trapping particles within this range from a heterogenous population. Previous studies showed that individually varying channel width (C_W), chamber depth (Ch_D), chamber length (Ch_L), and Re_c, affected the size distribution of particles trapped within the reservoir (Figure 2.3). Narrowing C_W results in smaller particles trapped within the reservoir [92]. A shallower Ch_D reduces the migration distance to the vortex, which is beneficial for smaller particles that do not have as large a migration velocity as large particles [91]. A longer Ch_L allows more time for smaller particles to migrate into the Vortex. Compared to the original Vortex geometry which had dimensions of C_W = 40 µm, Ch_D = 480 µm, Ch_L = 720 µm [54], we tested narrower C_W (15 − 25 µm), shallower Ch_D (130 − 325 µm), and comparable or longer Ch_L (625 − 1,250 µm). In addition to varying device geometry, we also tested Re_c ranging from 25 to 300.
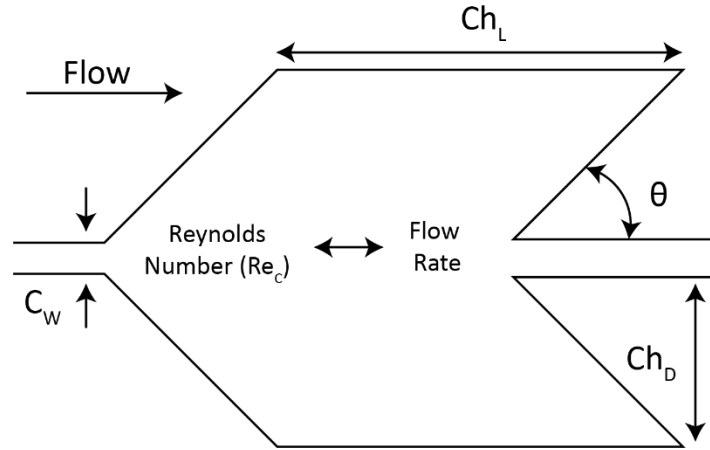
Figure 2.3 Figure showing the different geometric and operational parameters tested. C_W represents the channel width, leading up to and exiting the reservoir. Ch_L represents the chamber entry length. θ represents the angle between the trailing edge of the chamber and the channel. Ch_D represents the chamber depth. In channels where θ is not 90⁰, Ch_D is measured as the maximum distance from the channel wall to the edge of the reservoir. Reynolds Number (Re_C) is used to compare flow rates across different devices and is given by $Re_c = \frac{\rho U_{Avg} D}{\mu}$, where ρ is the fluid density, U_{Avg} is the average fluid velocity, D is the hydrodynamic diameter of the channel, and μ is the dynamic viscosity of the fluid.

We observed initial Vortex formation at Re_c = 50 - 75, consistent with previously reported results [53]. However, the average size of particles trapped within all tested reservoirs and Re_c's ($D_{Avg} \geq 11$ μm) was larger than the average size of particles in the inlet solution ($D_{Avg} = 10.4 \pm 0.48$ μm) (Figure 2.4). Additionally, from an inlet population that had 11% of the total particles in the 7 – 10 μm range, all the devices tested trapped fewer than 15% of particles within our size range. These results indicate our rectangular devices could not be used to enrich microparticles from a heterogeneous population and confirmed that we needed to change the more than just the parameters above to accomplish our goal of trapping particles in the 7 – 10 μm range.

A)

B)
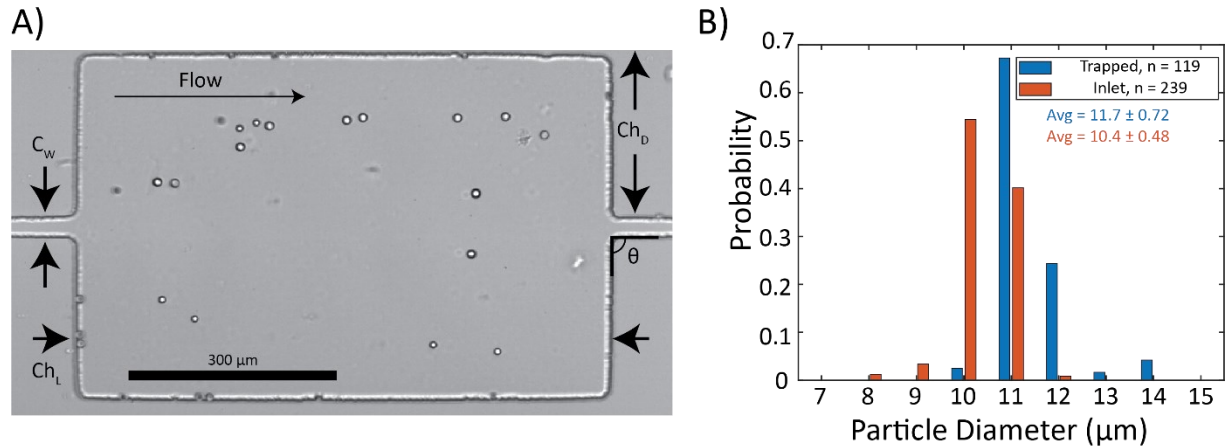
Figure 2.4: Representative image of particles trapped within the rectangle devices. A) from a solution of 10 μm particles, the device with dimensions 20 μm x 720 μm x 230 μm at a Re_c = 125 trapped large particles. The distribution of these particles are shown B) where the trapped particles have an average diameter of 11.7 μm but the inlet particles have an average diameter of 10.4 μm. This is representative of all rectangular devices tested, where the average diameter of trapped particles was larger than the average diameter of the inlet population.

2.3.2.   A Chamber Angle of 30° Changes the Particle Entrance Mechanism

Another potential avenue of investigation was the method of particle entry into the reservoir. Previous investigations have extensively studied particle entry into the reservoir, as this is a prerequisite to trapping particles [81], [91], [127], [141]–[143]. In rectangular chambers (θ = 90°), at sufficient Reynolds numbers (Re > 70), there are three methods of particle entry [81], [91]. Particles could migrate laterally into the reservoir and enter (lateral migration), contact the trailing wall and move along the microcavity wall to enter (contact entry), or collide with the trailing wall and enter without tracing the microcavity (collision entry). Lateral migration was the predominant method of particle entry observed in the rectangular chambers that we tested. This is consistent with previously reported results [91], [144], where lateral migration was shown as the method of particle entry in chambers with aspect ratios (AR = Ch_L/Ch_D) > 3. Collision and contact entry occur in rectangular geometries with AR < 3. In these chamber, at low Reynolds numbers (Re < 160), particles partially enter the reservoir and achieve a maximum lateral distance near the trailing edge of the reservoir, but then are quickly washed out [144]. However,

At higher Re (Re > 160), the change in vortex and separatrix morphology close to the trailing wall causes larger particles (D = 28, D/C_W > 0.4) to enter via collision or contact trapping [91]. Smaller particles do migrate laterally as well but have slower migration velocities and will not cross into the vortex before crossing the cavity.
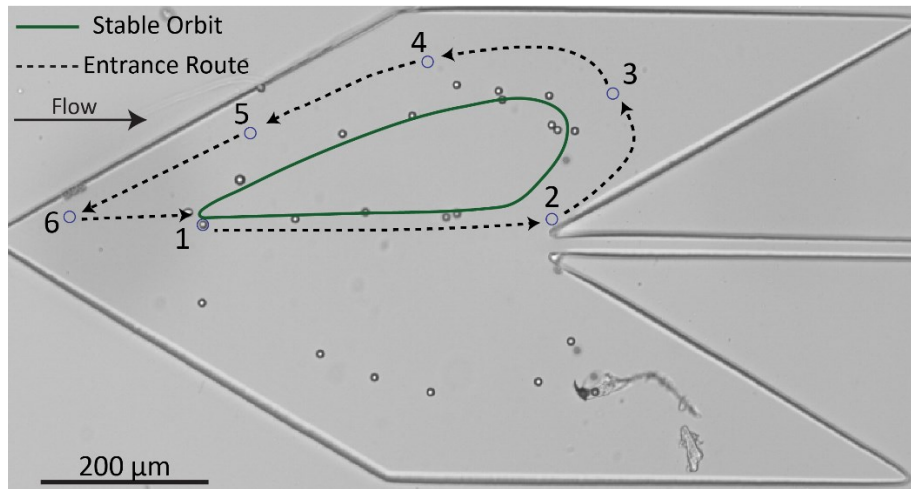
Figure 2.5: Sample image of the entrance path a 9 μm particle takes, in a device with ϑ = 30°. The particle, tracked from position 1, begins its entry trajectory at position 2. Positions 3-6 then complete the initial orbit, and the particle then enters its stable trajectory, highlighted in green.

To trap our target smaller microparticle targets, it is necessary to change the geometry to encourage these particles to enter the reservoir. When particles via collision or contact entry, previous studies showed that the trailing edge geometry plays an important role in influencing particles to enter [141]. Compared to rectangular chambers where the trailing edge abruptly stops the particle path, trailing edges that guide particles into the vortex (such as those in rounded cavities), help particles to get trapped more easily [141]. We designed a new Vortex device with trailing walls that guide particle entry into the reservoir by changing the angle between the channel wall and the trailing edge of the chamber (θ, Figure 2.3) and testing acute values of θ between 30° and 90°. Within these novel trapezoidal shaped chambers, we observed particle collision with the trailing wall (Figure 2.5, Position 2) at θ = 30°.

After collision, particles had two possible paths depending on the depth of the particle into the reservoir: it could leave the reservoir, or it could continue into the recirculation flow. We determined a minimum threshold depth that particles need to achieve to be trapped by measuring particle depth at the closest point between the particle and the wall (Figure 2.6A). We non-dimensionalzed this by dividing half the exit width, and termed this non-dimensional depth as Δ, given by $\Delta = \frac{Depth}{0.5 * Exit\ Width}$. For a device with dimensions of 20 μm x 650 μm x 275 μm x 30° (C_w x Ch_L x Ch_D x θ), the minimum threshold Δ (Δ_{th}) was found to be 2. Particles that had a Δ of 2 entered the chamber 100% of the time, but particles that had a $\Delta < 2$ entered the chamber only 43% of the time (Figure 2.6B). Evaluating the 20 μm x 650 μm x 275 μm device using the Δ metric showed that particle Δ values are proportional to the likelihood of particle entry, and a larger Δ value meant a higher probability of particle entry.

Having identified a Δ_{th} value, we focused on increasing Δ values for our target population to above Δ_{th}. In this device, where the channel had a constant width before and after the trapping chamber, particles within the 6 – 9 μm entered the reservoir 46% of the time, and none of these particles had $\Delta > 2$. As Δ is given by dividing particle depth by the exit width, we narrowed the exit width at the outlet of the chamber. By doing so, we induced an increase in Δ for particles with the same diameter; thus, increasing the probability of particle entry into the chamber. The new design had a channel width of 25 μm before the chamber, and a channel width of 15 μm after the chamber. We then examined particle entry into the reservoir and found that 75% of particles within this size range entered the reservoir, and all particles had $\Delta > 2$ (Figure 2.6C). This suggests that though these chambers have new channel widths, Δ_{th} remains constant with a value of 2. Additionally, these results indicate that the narrowed width design will successfully trap a

higher percentage of small particles (6 – 9 µm). For our geometry and Re$_C$, we established that a

Δ value of 2 can be considered a threshold Δ (Δ$_{th}$), above which particles enter the reservoir.
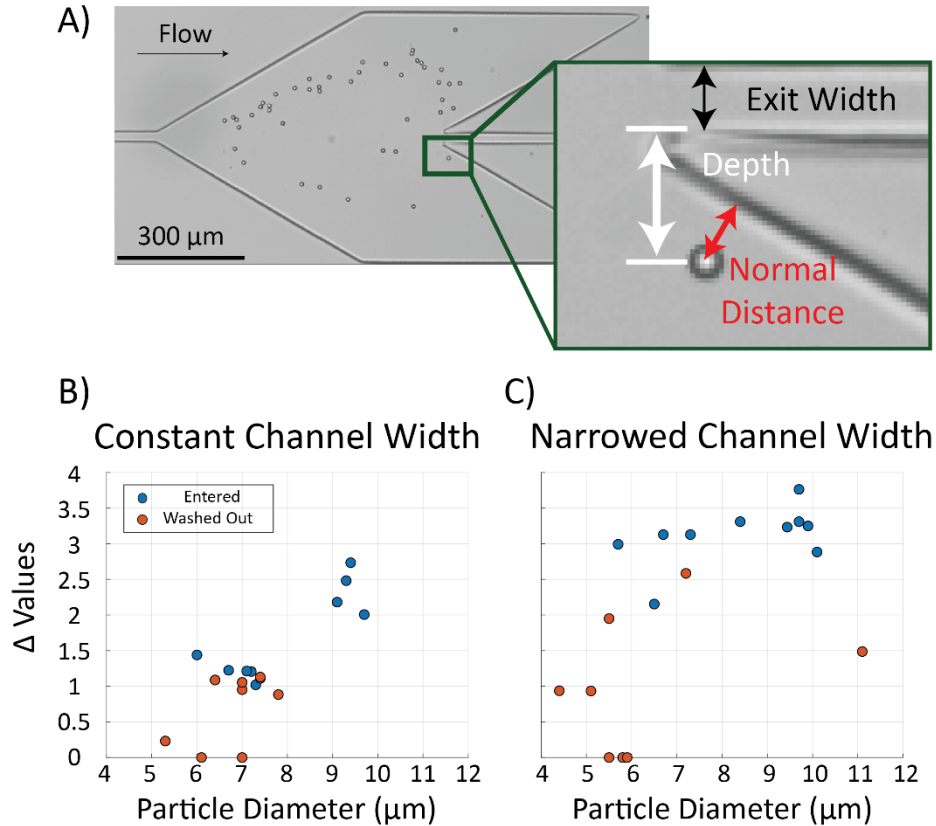
Figure 2.6: This figure demonstrates how the Δ measurements were taken and analyzed. A) represents the point that was used to get the depth value. The particle was tracked as it entered the reservoir, and at the minimum distance to the chamber, its depth was measured. This was then divided by half the exit width, and this number was the non-dimensionalzed depth, or Δ value for the particle. B) shows the Δ values for particles of different sizes, in the device with a standard channel width of 20 µm. C) shows the Δ values for particles of different sizes in the device with a narrowed channel width, from 25 µm to 15 µm. By comparing these two devices using the Δ metric, we can see that small particle between 7-10 µm in the narrowed channel achieve larger Δs, and are more likely to be trapped.

We analyzed high-speed images of trapped particles to obtain the size distribution of

particles in the chamber, validating whether enhancing the Δ value for small particles translates

to increased trapping within the reservoir. From a solution of particles with an average diameter

of 10.2 ± 0.7µm, we were able to trap particles smaller than 10 µm (Figure 2.7A). In the inlet

population, we measured 12% of the particles with D < 10 µm, but out of the trapped particles,

we measured 36% of particles with D < 10 µm, a 3-fold increase in purity from the inlet.

A) Trapped Particle Size

B) Trapped Cell Size
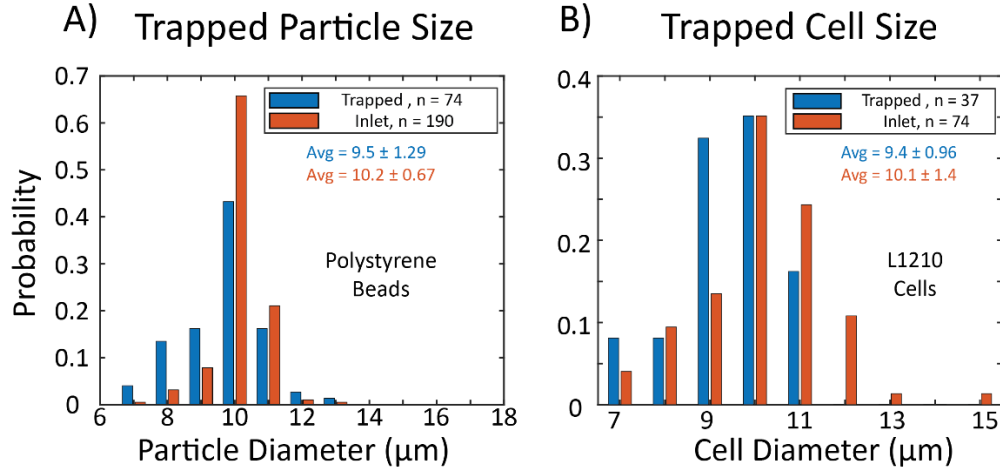
Figure 2.7: Plots showing trapped vs. inlet distributions for 10 μm particles and L1210 cell lines. A) shows the difference in trapped particle size distribution vs. the inlet particle size distribution for polystyrene particles. Particle images were captured either within the vortex (trapped), or in a well plate (inlet) and analyzed to obtain size information. This graph shows that even from a narrow size distribution of particles (STD = 0.67 μm), we can trap particles smaller than the mean inlet size. B) trapped vs. inlet population for L1210 cells plot showing that the vortex device traps a majority (86%) of cells within our 7-10 μm range, compared to the inlet population where only 66% of the population was within our target size range. Additionally, the mean diameter for the trapped population is lower than the mean diameter for the inlet population, again indicating that we are selectively purifying smaller cells.

2.3.3. The Effects of Changing Chamber Geometry and Re_c on Particle Δ Values

We investigated how changing chamber geometry, channel width, and Re_c affect Δ_{th}. We specifically used particles within 5-9 μm because we observed that these particles often had Δ values in the range of Δ_{th} and could be used to identify the value of Δ_{th}. In two devices with a narrowed channel width (from 25 μm to 15 μm) and a Re_c = 125, we increased the area of the chamber from 650 μm x 275 μm (Ch_L x Ch_D) to 725 μm x 325 μm. We found that the Δ_{th} value was unchanged, and that particles that Δ > 2 entered the reservoir (Figure 2.8). It is worth noting that in the device with a larger chamber area (725 μm x 325 μm), the total number of particles trapped were on average 10.7 ± 3.1 particles per trial, fewer than the number of particles in the smaller chamber (650 μm x 275 μm), which averaged 38 ± 1 particles per trial. We also increased Re_c from 125 to 150 and observed the effects on Δ_{th}. We found that in both devices, Δ_{th} remained at 2 (Figure 2.8), despite the increase in Re. However, in the 725 μm x 325 μm value, we observed

26

that more particles were trapped at Re = 150 than at Re = 125 (23.67 ± 2.4 at $Re_c = 150$ vs. 10.67 ± 3.1 at $Re_c = 125$). These results indicate that particle trapping is also a function of chamber area, and Re_c, but that changing these parameters do not impact Δ_{th}.

One possible physical interpretation for Δ_{th} is that it provides the maximum point of lateral convective transport of particles into the reservoir. This is also known as the separatrix, which provides the boundary that separates the recirculation flow from the main channel flow [81], [91]. For the geometries and conditions tested, Δ_{th} remains constant. However, more investigation is needed into the significance of Δ_{th}, such as using dye to determine and compare separatrix locations to Δ_{th} values. Additionally, the effects of Re_c and chamber size for trapezoidal chambers on particle trapping should be further studied to develop a comprehensive predictor of particle trapping behavior. These investigations would be extremely valuable for further modifying Vortex device target sizes, for example, to target populations such as platelets (D = 1-3 µm) where purification is necessary for transcriptomic analysis to identify disease-specific molecular signatures [145].

Re$_c$	25 μm - 15 μm x 650 μm x 275 μm	25 μm - 15 μm x 725 μm x 325 μm
Re = 125		
Re = 150		
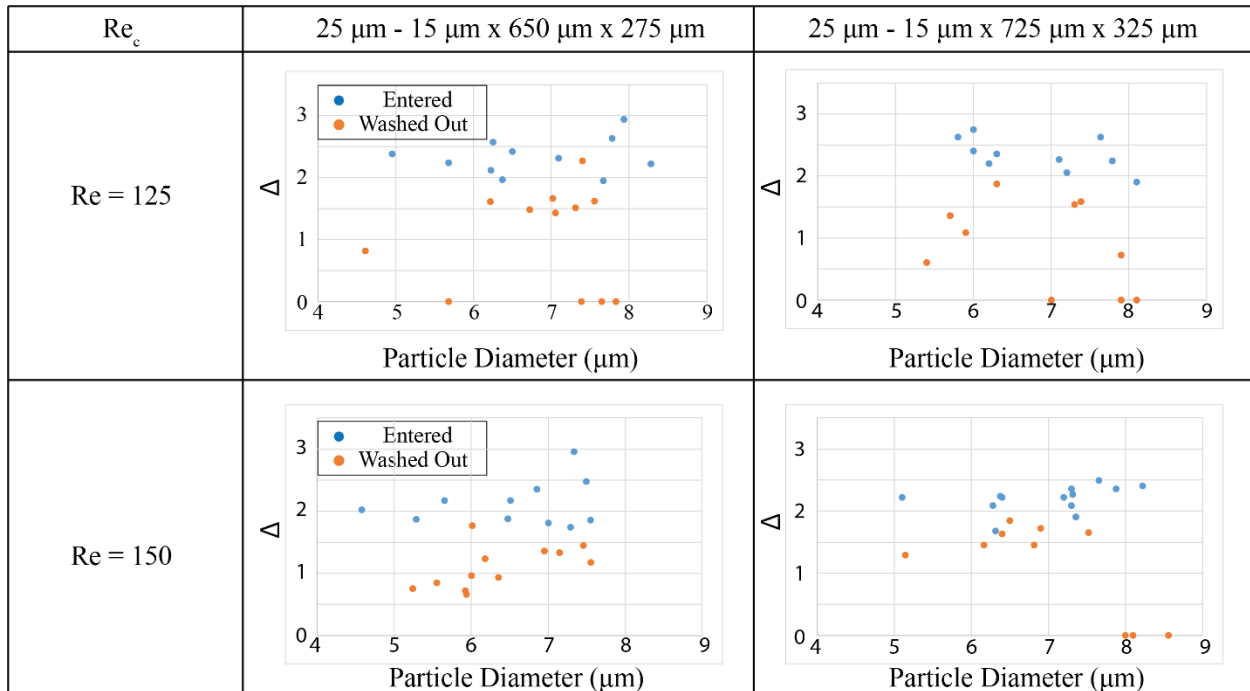
Figure 2.8: Investigation into how changing parameters such as chamber size and Re$_c$ affect Δ$_{th}$. In the top row, we can see that 82% of the particles that entered the reservoir had a Δ > 2, and only 1 particle with a Δ > 2 did not enter the reservoir, indicating that the Δ$_{th}$ value is 2. Similarly, in larger chamber, Δ analysis shows that all particles with Δ > 2 enter the reservoir. Looking at both chambers for a higher Re, we can see similar trends. These observations show despite changing Re$_c$ and chamber size, a Δ$_{th}$ remains constant at 2.

2.3.4. Offset Channel Device Traps Small cells from Cell Populations

The device was then evaluated for its performance trapping small cells (7-10 μm). This cell size distribution was chosen because it overlaps with important clinical targets such as lymphocytes [86]. Analyzing lymphocyte count, morphology, and genetic makeup, can provide valuable information about a patient such as predicting and assessing patient response to chemotherapeutics [146] and immunotherapy [147]. Lymphocytes can also be engineered as a therapeutic tool in cancer and HIV patients [148]. Previous work has shown that, due to differences in microparticle properties, such as deformability and membrane properties, cell populations trapped within the device were on average larger than trapped rigid microspheres [53]. Though we accomplished our goal of enriching polymer microparticles within the 7-10 μm

size range, to assess the utility of this device in different fields we needed to test our device performance with cell lines. L1210 cells were selected specifically for their average cell sizes of 10.1 µm ± 1.4 µm indicating a large population within our target size range. The results are shown in (Figure 2.7B). The trapped population had an average size of 9.4 ± 0.9 µm. The inlet population did have cells with diameters greater than 12 µm but these cells were not trapped within the vortex. The data also shows that our device targets cells within the target 7-10 µm range, as 58% of the trapped cells fall within this size range, compared to only 34% of the inlet population, a 0.7 – fold increase in purity of our target population. This indicates that even from a heterogenous population of cells, our device can enrich cells in the 7-10 µm size range.

2.3.5.   Cell Collection and Viability Assays

We collected the trapped cells from the devices to assess their size distribution and viability. We also analyzed size distributions of cells collected from rectangular geometries, to confirm that our novel trapezoidal geometry with a narrowed exit width outperforms rectangular devices when targeting cells in the 7-10 µm distribution (Figure 2.9, Panel A). The two rectangular devices had dimensions of 25 µm x 720 µm x 230 µm (Rectangular 1, denoted in Red) and 25 µm x 1000 µm x 230 µm (Rectangular 2, denoted in gold), and both were operated at Re_c = 125. While all rectangular devices tested trapped polystyrene beads with similar size distributions, these two devices were chosen because they had the smallest footprint. From Figure 2.9A, we can see that the distribution of cells collected from the trapezoidal chip has an average size of 11.6 ± 2.9 µm, while the distributions of cells collected from Rectangular 1 and Rectangular 2 have average sizes of 14.5 ± 3.9 µm and 17.6 ± 3.6 µm, respectively. Additionally, 50% of the cells collected from the trapezoidal device with the narrowed channel width are within the prescribed 7-10 µm size

range, while only 12% from Rectangular 1 and no cells from Rectangular 2 are in our target population. This shows that compared to the other rectangular Vortex geometry we investigated, our novel trapezoidal geometry with a narrowed channel width will give us a greater than a 4-fold increase in purification of cells 7-10 μm.
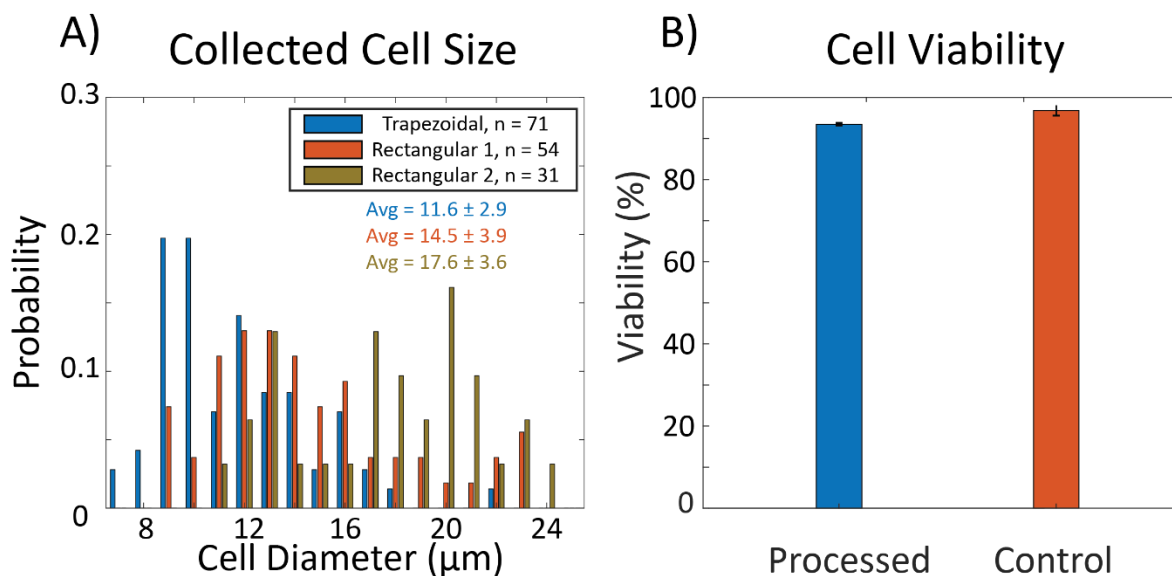
Figure 2.9: Analyses performed on cells collected from the trapezoidal and rectangular devices. A) exemplifies the size distribution in populations Trapped and collected by the trapezoidal device (shown in blue) and two rectangular devices (Rectangular 1 has dimensions of 25 μm x 750 μm x 230 μm, shown in red, and Rectangular 2 has dimensions of 25 μm x 1000 μm x 230 μm, shown in gold). The new trapezoidal device traps a smaller cell population, as shown by the averages of the collected cell sizes. B) confirms that the device does not adversely affect cell viability. Cell processed by the device had a viability of 93.5%, compared to 96% viability in the control population.

An important criterion to evaluate cell processing devices by is the viability of the final product. Devices that can enrich target cell populations and provide viable purified populations are more valuable when downstream applications require viable cells. Some examples include modifying or engineering lymphocytes for therapeutic purposes such as cancer [136]–[138], [146] or HIV therapy [29], [139], [149] or observing leukocyte rolling behavior to assess patient diabetes status [58], [62]. We stained trapped cells with propidium iodide (dead cell stain). Once we collected these cells, we added Calcein-AM (live cell stain). We found that cell viability was

minimally affected by device processing. For cells processed by the device, we saw a 93.5%

viability, compared to 96.8% viability with unprocessed cells (Figure 2.9B) showing that the device

preserves cell viability.

2.4. Conclusion and Future Works

In this work, we expanded the capabilities of Vortex trapping to trap polymer particles in

the 7-10 µm range. We explore a new geometry using trapezoidal chambers to guide polymer

particles into the reservoir. We further narrow the channel width at the exit of the reservoir and

show that this encourages more particles in our target size range to enter the reservoir.

Additionally, we introduced a new metric, Δ, which can be used to characterize particle behavior

in the reservoir. Due to the correlation between Δ_{th} and particle entry into the reservoir, we

believe Δ_{th} could represent the separatrix location, which separates main channel flow from the

recirculation flow. In addition to its performance with polystyrene microparticles, we confirm

that this device performs similarly with deformable cells, and able to enrich cells within the 7 –

10 µm range, with high viability. We also determined that this new device outperforms traditional

rectangular Vortex trapping devices when targeting particles in the 7 – 10 µm range.

This work is critical because target cell populations (lymphocytes, spermatocytes, and

stem cells) and polymer particles can be purified and from heterogeneous populations of

background cells or heterogeneous sized particles, respectively. These targets can also benefit

from the secondary functionalities that Vortex devices provide, such as biomolecular delivery for

immune cell engineering, droplet encapsulation for single cell studies, and solution exchange for

layer-by-layer particle fabrication. Future work should focus on integrating this Vortex device

with additional secondary functionalities, thus increasing the impact of this finding.

Chapter 3. A Parameter Investigation into the Vortex-Assisted Electroporation of Small Cells

3.1. Introduction

The delivery of biomolecules such as DNA, RNA, and proteins across the cell membrane is of critical importance for uses in biomanufacturing [150], fundamental biological studies [151], gene editing [152], cell therapies [153], and cell engineering [98]. The two major families of intracellular delivery methods are carrier-based methods, where the cargo is encapsulated in viral vectors [154], [155] or liposomes [156], [157], and physical membrane disruption methods such as electroporation [94], [107], [158]. While carrier-based methods have been used for decades and are well characterized, they are limited by the cargo they can deliver, and the cell types they can be used for. Viral vectors are limited to the delivery of nucleic acids, and even then, to small sequences [155], [159]. Lipofection has more flexibility with the cargo size, as the carrier is synthetically created. However, lipofection is notoriously ineffective for transfecting suspended cells [160], [161].

Physical membrane disruption methods offer a solution to both the above problems of cargo limitations and suspended cell transfection [162], [163]. Electroporation, the process of permeabilizing the cell membrane via application of an electric field, is especially of interest because of its high delivery efficiency to suspended cell lines [162], [163], and low processing times [164]. Electroporation does not have as severe cargo limitations, and has been used to deliver nucleic acid [94], [165]–[167], protein complexes and conjugates [153], [168]–[170], fluorescent molecules [171]–[173], chemotherapeutics [174], [175], and synthetic nanoparticles [176]–[178]. Due to its versatility, the integration of electroporation with devices that offer other

functionalities such as cell separation and cell focusing [38], [39], [179], [180], is a rapidly growing field of research.

The integration of electroporation with microfluidic devices has been a rapidly growing field of research for the past few decades [38], [179]. Microfluidic devices are attractive methods of cell separation and focusing [181]–[183], because device dimensions are often of the order of cell size, allowing for precise control of cells. Inertial microfluidic devices are a subclass of microfluidic devices that additionally offer label-free cell manipulation, high throughput processing [31], and the capability to be integrated with other functionalities [33] (a full review of inertial microfluidic device can be found in 1.1.2, and ref [31], [33], [42], [184]). Their feasibility as high throughput biological and clinical research tools was demonstrated for various applications, including cell purification for rare circulating tumor cells and fetal trophoblasts [54], [185], [186] and clinically relevant assays such as hydrodynamic stretching to identify and diagnose sepsis [187] and leukocyte profiling [62].

Inertial microfluidic Vortex trapping devices (previously described in 1.1.3, Chapter 2, and [54], [188], [189]) are a family of inertial microfluidic devices originally developed as a cell purification method that targets large, circulating tumor cells (CTC's) from blood. This specific inertial microfluidic device integrates well with electroporation, as the device offers a high degree of control over particle residence time. This enables the critical steps of electroporation and immersion in biomolecule solutions of interest, required for biomolecular delivery. Vortex trapping devices have previously been integrated with on-chip electroporation for intracellular delivery of plasmids [76], [80], drugs [78], [79], and nucleic acid and protein conjugates [80].

Despite these benefits, previous generations of Vortex trapping devices were limited to targeting large cells such as CTC's [54], [188] and fetal trophoblasts [54], [185], with cell diameters, D > 15 µm. In Chapter 2, we furthered the capabilities of Vortex trapping devices to target small cells (D = 7 − 10 µm). In this work, we integrate this new generation of Vortex trapping devices with electrodes for on-chip electroporation and biomolecular delivery. We optimized the electrode geometry for our new small cell trapping chamber geometry and varied the electrode geometry to enhance the average electric field strength experienced by the cells. Next, we investigated the effects of various parameters of the waveform on permeabilization of the cellular membrane and performed cell viability assessments. Finally, we attempted to transfect our target L1210 cells with ZsGreen plasmids.
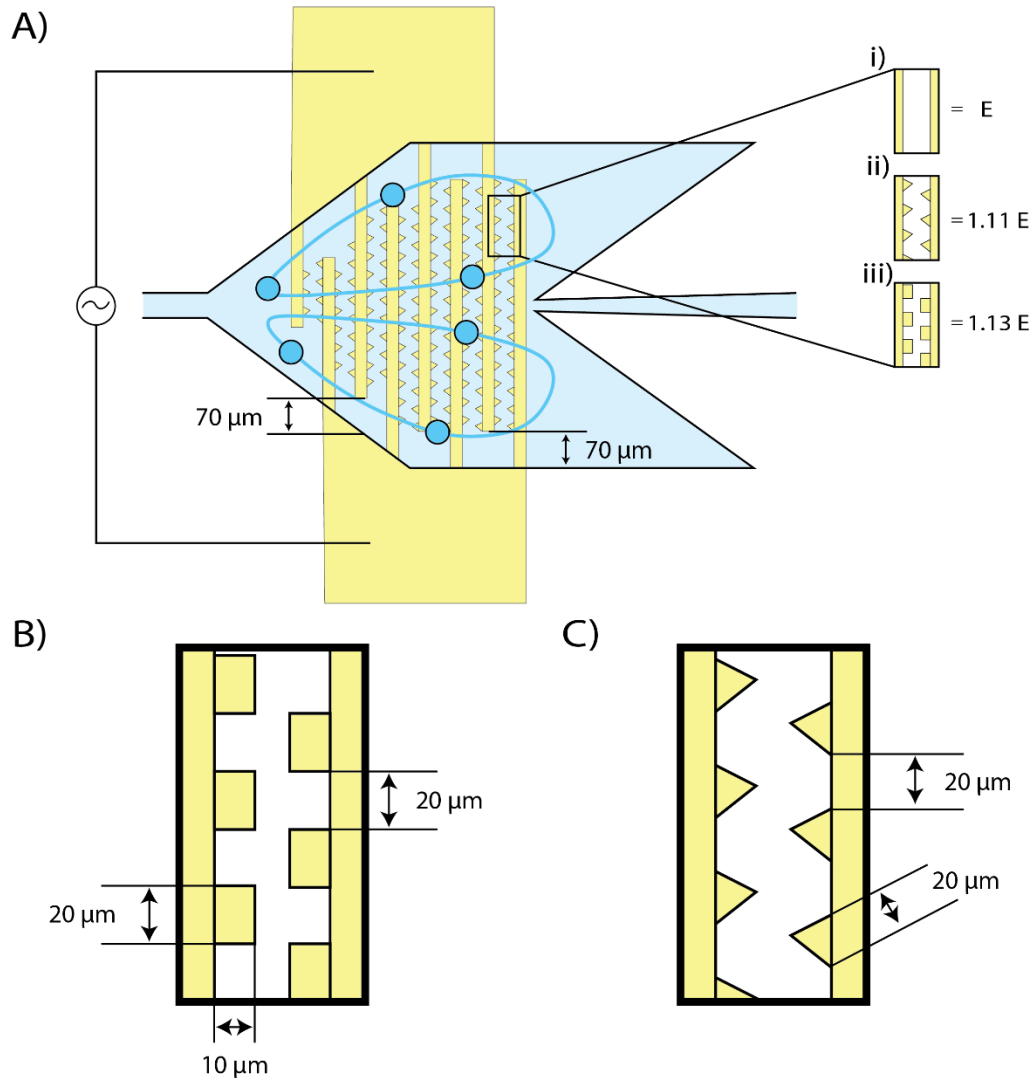
Figure 3.1: Overview of the parameter investigation into electroporating small cells (7-10 µm). A) shows the electrode scaling to accommodate the changing chamber depth in the device used to trap small cells. The large rectangles on either side are the solder points to connect the electrical signal. Within the device, cells orbit in the chambers above gold electrodes patterned on the glass slide. In addition to designing the electrodes to better fit the reservoir, we also investigated increasing the electric field, by modifying the edges. i) shows previous electrodes fabricated. ii), iii) show that by augmenting the edges of the electrodes with triangles and rectangles increases the electric field strength by a factor of 1.11 and 1.13 respectively. B) shows the dimensions of the rectangular serrations. The rectangles have a width of 20 µm, a height of 10 µm, and are spaced 20 µm apart. C) shows the dimensions of the triangular serrations, which have equal side lengths of 20 µm, and are spaced 20 µm apart.

3.2. Materials and Methods

3.2.1. Device Geometry

The small cell electroporator comprises of two layers: a fluidic layer and an electrode layer. The fluidic layer is a single microfluidic channel that leads to a reservoir in which the cells of interest are trapped. The electrode layer is made of patterned electrodes on the glass slide underneath the reservoir, positioned such that the orbits of the cells trapped in recirculation flow

are directly above the electrodes. The dimensions of the fluidic layer are discussed in Chapter 2. There are a total of 8 electrodes. The electrodes end 70 µm before the fluidic reservoir wall, to ensure sufficient room for bonding between the glass and the fluidic layer. The electrodes are interdigitated rectangles, with a width of 20 µm and a height of 10 µm. The shortest electrode was 133.3 µm long, scaling up to 504.5 µm long. The edges of the electrodes are serrated in the shape of equilateral triangles, with side lengths of 20 µm and a height of 300 nm.

3.2.2. Device Fabrication

Both the fluidic layer and the electrode layers were designed in AutoCAD. The fluidic layer mask was fabricated as a film transparency mask by (CASOutputcity, USA). The electrode layer was fabricated as a chrome mask by (Photosciences, USA). The fluidic layer was then patterned onto a silicon wafer and cast in PDMS using standard photolithography. Briefly, photoresist (KMPR, Kayaku Advanced Materials, USA) was spin coated onto a silicon wafer (University Wafers) and exposed to UV light. Excess photoresist was removed using SU-8 developer (Kayaku Advanced Materials, USA). PDMS was then cast onto the mold at a ratio of 5:1 (polymer: curing agent) and cured at room temperature. These steps were taken to ensure the fidelity of the design and to avoid deformation of the chamber during high temperature curing, minimizing the chance of misalignment. The inlet and outlet ports were created using a syringe (Becton Dickson, USA) and a 20G blunt needle (SAI, USA). The electrode layer was fabricated using standard lift off procedures. A glass slide (Histobond+ Supa Mega Slides, Histobond, USA) was spin coated with photoresist (SPR 220, Rohm and Haas, USA) and exposed to UV light through the electrode chrome mask. Excess photoresist was removed using AZK-400 developer. The developed slides were then placed into an electron beam evaporator (Sharon Vacuum CVS-6 Evaporator, USA).

Chrome and gold were deposited onto the glass, at heights of 10 nm and 300 nm (Kurt Lesker, USA), respectively. Finally, the coated slides were placed into an acetone bath and mildly agitated for 1 hour, and excess metal removed. The devices were bonded to the electrodes, using O_2 plasma. Electrical leads were connected to the electrodes using low melt solder.

3.2.3. Cell Culture

L1210 cells were cultured in Dulbecco's Modified Eagle's Medium (DMEM) (Corning, USA). The growth medium was supplemented with 10% fetal bovine serum (FBS, ThermoFisher Scientific, USA) and 1% penicillin-streptomycin (ThermoFisher Scientific, USA). The cells were grown for 2 days before they were harvested for the experiment.

3.2.4. Device Operation

Optimal conditions for cell trapping were found using methods described previously (see Chapter 2). Based on those results, we determined the operating pressure of the device to be 60 PSI, equivalent to a flow rate of 210 uL/min. The device was initially flushed and primed using DPBS (Hyclone, USA), at 60 PSI for 30 seconds. Afterwards, a co-flow of cell solution (at a concentration of 20k cells/mL) was introduced into the device in two steps, a 50 second injection step followed by a 20 second withdraw step. This withdraw step was done to ensure minimal contamination of device tubing by the cell solution. Cells were trapped in the reservoir, in vortices generated by the recirculation flow. After the cell trapping step, the solution was exchanged using methods described previously in Chapter 2. The electric field was then applied, and the cells were incubated in a solution of 15 µm Propidium Iodide (PI, ThermoFisher Scientific, USA) for 90 seconds. Another solution exchange step was then performed to the final collection media. The final media was composed of 50% FBS, 49% DMEM, and 1% penicillin-streptomycin. Previous

work showed that this increased serum concentrations post electroporation increased cell viability [190]. To collect the cells, the pressure was lowered to 20 PSI for 10 seconds, then increased back up to 40 PSI for 15 seconds. A total of ~50 uL was collected per trial.

3.2.5. Pulse Driver Mechanism

A custom-built electroporation box was used to supply the electrical energy required for electroporation. The box took in a DC signal at a predetermined voltage and output a train of pulses of square waves. The frequency of these waves was set at 20 kHz, as this was shown to provide a sufficient electric field strength, while at the same time, not creating large bubbles from electrolysis [79], [80]. Pulse durations were varied between 5 and 20 ms, and the number of pulses was between 5 and 20 pulses. There was a 1 second gap between pulses.

3.2.6. Electroporation Testing and Viability

When the cells were processed by the device, permeabilized cells were stained with 15 µM PI solution. After collection, cells were then stained with Calcein and incubated for 25 minutes. The collection media was then aspirated, and the cells resuspended in PBS for imaging. The images were then processed via a custom imaging pipeline, using CellProfiler (Broad, USA) to identify the cell outlines and Python (Spyder IDE, MIT, USA) to measure cell fluorescent intensities, previously reported in [79]. The pipeline classified cells as live, dead, or electroporated, based on expression of Calcein, PI, or both, respectively. We could then assess cell viability and electroporation efficiency for different electroporation conditions.

3.2.7. Plasmid Purification

DH5alpha competent cells were transformed with ZsGreen plasmids, by following the associated protocol. The plasmid was grown in a 5 mL starter culture of Luria Broth (Sigma Aldrich, USA), for 16 hours, then moved to a 100 mL of Luria Broth culture for another 16 hours. A Qiagen Plasmid Maxi Prep Kit (Qiagen, USA) was used to extract the plasmid

3.2.8. Conventional Cuvette Electroporation

Transfection efficiency in conventional cuvette electroporation was tested using the Eppendorf Eporator (Eppendorf, USA). Each cuvette was loaded with ~100 μL total, composed of 2 μL cell solution from a stock of 100,000 cells/mL, 50 μL Hyclone DPBS, and 50 μL Gene Pulser Electroporation Buffer (Bio-Rad, USA). The final plasmid concentration was 15 μg/mL, to match the plasmid concentration used in for on-chip transfection. The cuvettes had electrode spacings of 0.2 cm (Gene Pulser, Bio-Rad, USA).

3.3. Results

3.3.1. Electrode Optimization

The geometry of the microfluidic device described in Chapter 2 is significantly different from the geometry of previous electrode-integrated Vortex devices [79], [80], [182]. All previous Vortex trapping devices integrated with electrodes had rectangular chambers. Consequently, the electrodes in previous Vortex trapping chambers were of equal length [80]. The small cell trapping Vortex chamber presented in Chapter 2 had a trapezoidal shape, where the trailing edge formed a 30° angle with the channel wall. Therefore, the electrodes had to be of varying lengths because the electrodes are not orthogonal to the chamber wall. To accommodate this non-

orthogonality, we designed electrodes that scale in lengths from 133 μm at the inlet of the chamber to 504 μm at the outlet. The electrodes extended from either side of the chamber and stopped 70 microns before the opposing edge (Figure 3.1A). This is the closest measured distance between the cell orbits of 9 μm cells and the edge of the chamber, thus placing the electrodes under potential cell orbits and maximizing the electric field experienced by the cell.

Additionally, the target cells of this device are smaller than previous Vortex-based electroporation targets [76] and require a stronger electrical field for successful electroporation. The relationship between the cell size and external electric field required is given by the governing equation for electroporation:

$$\Delta V_{tm} = f * E_{ext} * r * cos\ (\theta) \qquad\qquad (3.1)$$

where ΔV_{tm} is the transmembrane potential required, f is a form factor related to cell type, E_{ext} is the external electric field, r is the radius of the cell, and cos (θ) is the cosine of the angle between a point on the membrane and the electric field [162]. For mammalian cells, ΔV_{tm} and f have nearly constant values of 200 mV and 1.5, respectively [107]. Analyzing the remaining variable, we can determine that the external electric field and the radius of the cell have an inverse relationship. According to the equation, electroporating small cells (D = 7-10 μm) will require a stronger electric field than previous Vortex-based electroporation targets (D > 15 μm) [76].

One way to create a stronger electric field is to simply increase the input voltage. However, when high voltages (and consequently, high currents) are applied, electrolysis occurs at the edges of the electrodes creating gas bubbles. The proximity of these bubbles to each other causes them to aggregate and generate large bubbles that displace cells from their orbits within

the vortex. Another approach that we investigated to increase the electric field was augmenting the electrode geometry. The electric field along the edges of smooth electrodes has a constant magnitude (Figure 3.2). However, at sharp edges, such as those in the serrated electrodes, the electric field is more concentrated, locally increasing the magnitude. This increase in magnitude is observable at heights of 17.5 μm (the approximate plane of the orbiting cells), and at locations along the anticipated trajectories of the cells. By locally increasing the magnitude of the electric field at these points, we can increase the average electric field strength along the anticipated trajectory of the cells. This method of increasing the electric field also localizes bubble formation, thus reducing bubble proximity and aggregation, which prevents large bubbles from forming and disturbing the stability of the trapped cells.

	Traditional Electrode	Serrated Rectangles	Serrated Triangles
Electrode Mask Design			
COMSOL Simulation V$_{in}$ = 7.5 V (kV/cm)			
Average E-Field Value (% increase from traditional electrodes) (kV/cm)	0.77 (+0%)	0.87 (+13%)	0.86 (+11%)
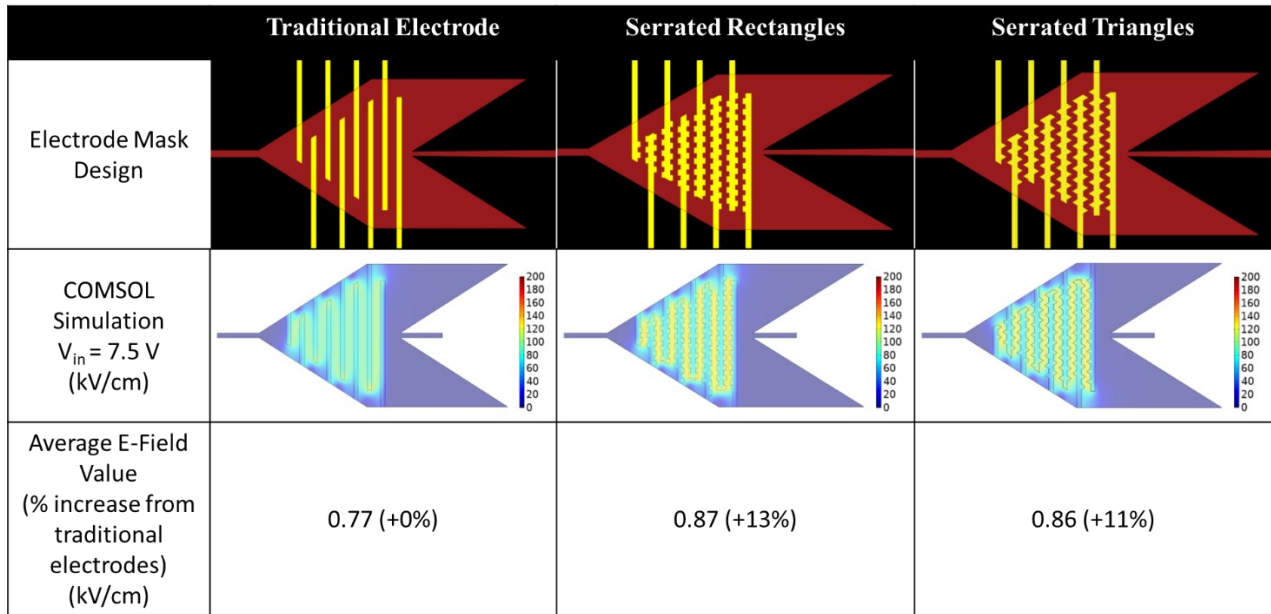
Figure 3.2: COMSOL modeling results of electrode geometry variations. In the column titled traditional electrodes, the electrode geometry shown are traditional smooth electrodes, previously shown in [79], [80] that have been minimally redesigned to fit under the new trapezoidal cell trapping chamber. The column labeled serrated rectangles shows the traditional electrodes, augmented with rectangles along the edges. These serrations were added to locally increase the electric field, thus increasing the average electric field experienced by the cells.

The sharp corners along the electrodes were created by serrating the edges of the electrodes with rectangles and triangles (Figure 3.2). The rectangles measured 20 μm in height and 10 μm in width, spaced 20 μm apart (Figure 3.1B). The triangles were equilateral triangles with a side length of 20 μm, spaced 20 μm apart (Figure 3.1C). Using COMSOL Multiphysics, we computed the electric field strength at locations along the anticipated cell trajectory at a height of 17.5 μm, half the total height of the chamber, where the cells are expected. Adding rectangular or triangular teeth increased the electric field by 13 and 11%, respectively, to 0.87 and 0.86 kV/cm. These increases were sufficient to permeabilize the trapped cells (Figure 3.3). Even though we observed electrolysis, the distance between serrations prevented aggregation of these bubbles, which prevented large bubbles from forming and displacing trapped cells out of the recirculation flow. However, consistent fabrication of the serrated rectangle electrode design was not possible. The narrow clearance between adjacent rectangular teeth leads to residual gold between electrodes of opposite polarity, creating a short circuit. Serrated triangle electrodes created comparable electric field increases and could be consistently fabricated. Therefore, further experiments were continued with the serrated triangle electrodes.
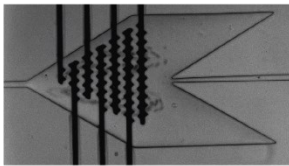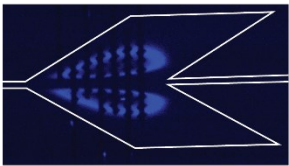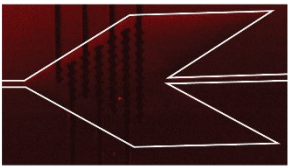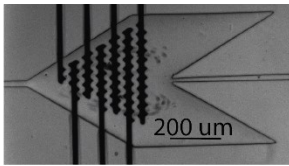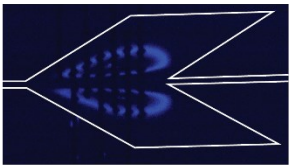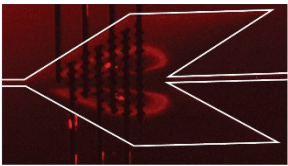
20 V P-P	BF	DAPI	TRITC
Pre Electroporation			
Post Electroporation	200 um		

Figure 3.3: This figure shows successful electropermeabilization of L1210 cells with serrated triangle electrodes. In the top row, we see that cells are trapped from both the brightfield and DAPI channels, however, there is no TRITC signal, indicating that cells

3.3.2. Real Time Evaluation of Electroporation

A membrane impermeable dye, such as Propidium Iodide (PI), can be used for real-time evaluation of electroporation performance by measuring the fluorescent intensity. This is because PI will enter the cell, bind to DNA, and fluoresce only if the cell is electropermeabilized. We calibrated the change in fluorescent intensity of the system by measuring the increase in fluorescent signal when no voltage is applied (negative control) and when a cytotoxic electric field was applied. By observing the time of onset of the fluorescent signal increase, and the increase in intensity after electroporation, we were able to rapidly evaluate different parameters for cell permeabilization.

The on-chip negative control had no applied electric field and we observed no increase over time in PI signal intensity (Figure 3.4A). In contrast, at an applied peak to peak (P-P) voltage of 25V, a pulse count of 10, and a pulse width of 1 ms, we saw an immediate and sustained increase in signal, with high final signal intensity (~5,000 AU, Figure 3.4C). We confirmed this electroporation parameter combination condition results in low viability (6.5 ± 1.5%) using post-collection Calcein-AM staining. The real time fluorescent signal analysis of this condition

confirmed that when cells died due to cytotoxic electric field strengths, irreversible pores formed

on the membrane and caused these cells to die and uptake large quantities of PI [171], [191].

Varying Voltage

Varying Pulse Width at 15 V

Varying Pulse Count at 15 V
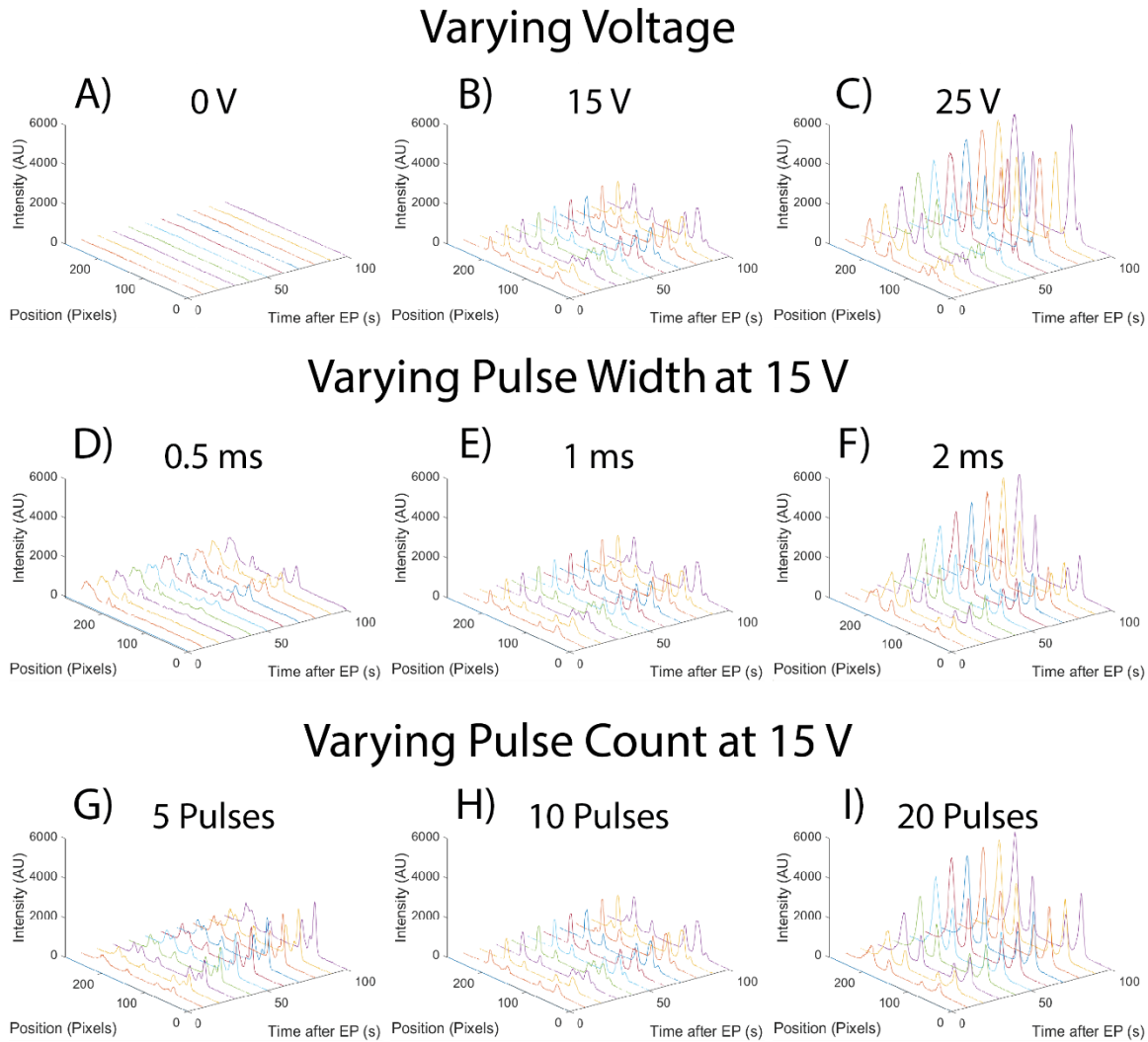
Figure 3.4: These plots show how the PI signal varies with time, as a function of changing the electroporation waveform. A-C demonstrate that by increasing the P-P voltage, we observe larger intensity changes, going from no detectable increase at 0 V in panel A, to 5,338 AU in panel C. These were used as our live and dead standards, respectively. All other experiments were done at P-P voltage of 15 V. D-F demonstrate the effect of varying P_W. At a P_W of 0.5 ms, the signal growth is detectable initially, indicating that some cells died during tlectroporation. However, this signal remains unchanged for 30s, and then begins to grow again, indicating dye is taking time to diffuse into the cell. In contrast, at P_W of 1 and 2 ms, the signal is growing over the course of the 100 s, and reaches maximum intensities 1,707 and 4,949 respectively. G-I show similar results to when changing P_C. When $P_C = 5$, the growth in intensity is observable only after 30 s. At pulse counts of 10 and 20, the growth in intensity is observeable over the course of the 100 s. At $P_C = 20$, the maximum intensity is 5,024 indicating increased amounts of PI uptake due to cell death.

Previous Vortex electroporation devices showed successful electroporation using a P_W of

1 ms and a P_C of 10 pulses [80]. At these values, we found an immediate increase in fluorescence,

45

and constant growth throughout the 90 second imaging time. This behavior is also observed at higher pulse counts (20 pulses) and longer pulse widths (2 ms), but the intensity peaks were considerably higher (5,024 and 4,949, respectively) (Figure 3.4 I, F). The immediate and sustained increase in fluorescent intensities, as well as the high final intensities were also characteristic of our dead control. These observations indicate that at increased P_C values (20 pulses) and P_W values (2 ms), we should expect high cell mortality.

In contrast, at lower P_C (5 pulses) and shorter P_W (0.5 ms) we see that the fluorescent signal remains consistent through the first 30 s after the pulse; and then increases in magnitude. These conditions also had lower final intensities of 1,154 and 1,043 AU, respectively (Figure 3.4 G, D). The increase in signal indicates that the cells are successfully permeabilized and PI entered the cell, but in contrast to dead signals, PI diffuses into the cells only after 30 s. This behavior indicates that dye is slowly diffusing through the pores created by electroporation, as opposed to flooding the cell immediately following cell death. Through this real-time analysis, we were able to narrow our investigations to a P-P voltage of 15V, change the P_W for electroporation from 1 ms to 0.5 ms, and vary P_C between 5, 10, and 20 pulses.

3.3.3. Optimizing P_W and P_C to Minimize Cell Death

Once we identified promising conditions from our real-time fluorescent intensity analysis, we collected cells to test cell viability after electroporation. Cells were electroporated on chip to deliver membrane impermeable PI, collected, and stained with Calcein-AM as a live cell stain. By measuring the fluorescent intensities of both PI and Calcein-AM in each cell, we created 2D intensity maps for each electroporation condition (Figure 3.5). We used CellProfiler to identify cell outlines in fluorescent channels. Using Python, we calculated the average PI and Calcein-AM

46

intensities in the identified regions. Cells that were only Calcein-AM positive were classified as live. Cells that were only PI positive were classified as dead. If a cell was stained with both Calcein-AM and PI, it was classified as electroporated.
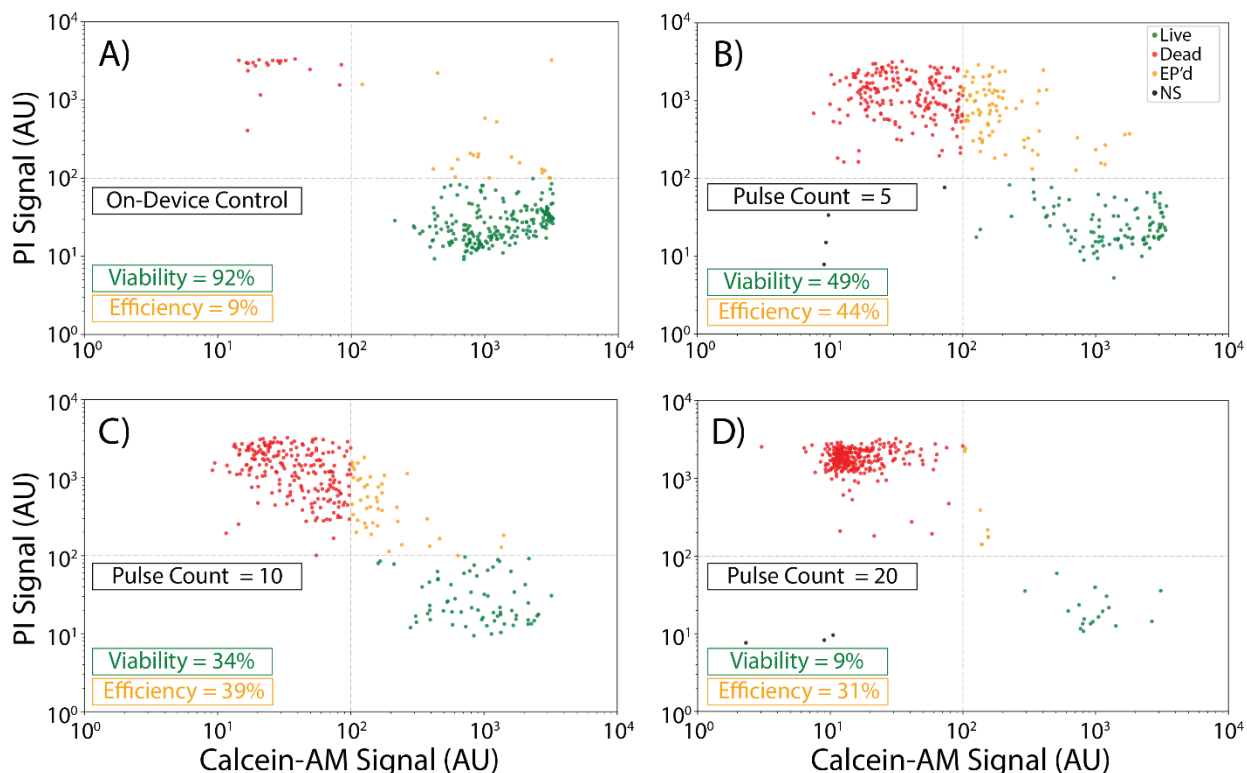
Figure 3.5: Plots showing the PI and Calcein-AM signal intensities, and the classification system used to identify live, dead, and electroporated cells. A-D) show the results of staining with different pulse count conditions of no applied electric field (A) 5 pulses (B) 10 pulses (C) and 20 pulses (D). These results show that at 5 pulses, we see electroporation of cells (44%) with minimal cytotoxicity. For conditions with more than 5 pulses, we see significant decreases in viability (15% and 9% at 10 and 20 pulses respectively) and no increase in electroporation efficiency. These results indicate that 5 pulses will provide a gentle electric field, capable of permeabilizing the cell.

When no electric field was applied, we found that the cells had a high viability of 93.5% (Figure 3.6). This was in good agreement with the control cells, which had a viability of 96%. Importantly, there was minimal false electroporation at 9%, which indicates that the delivery of PI is due to successful electropermeabilization, and not lysis due to fluidic forces. All experiments were done with a 15 V P-P voltage, 0.5 ms P_W, and P_C values of 5, 10, or 20 pulses. At 5-pulses, the results show that the cells have a viability of 55.6% and an electroporation efficiency of

33.3%. Further increasing P_C showed minimal increase in EP efficiency, but a significant decrease

in cell viability (< 50% viability). These results indicate that the electrical signal for gentle delivery

of membrane impermeable dye is 5 pulses of a 20 kHz square wave, with a P-P voltage of 15V,

and a pulse width of 0.5 ms.
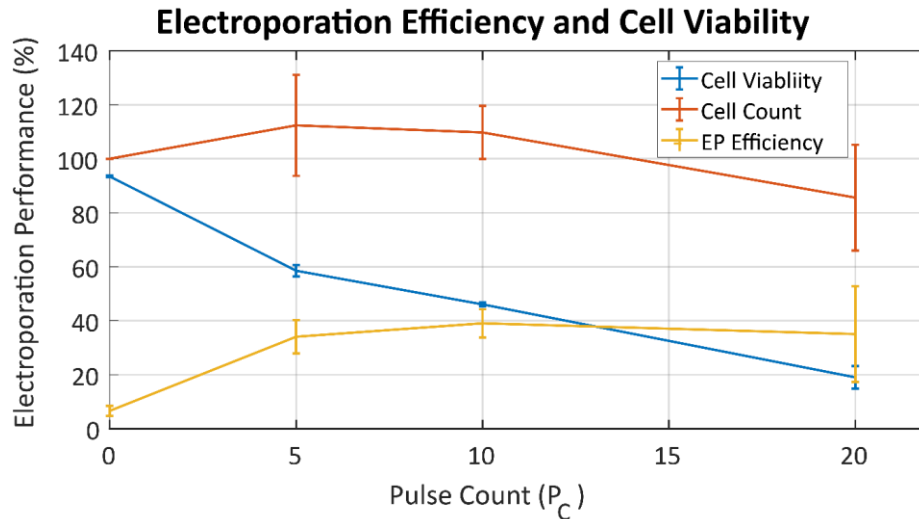
Figure 3.6: Shows the analysis of collected cells for viability and electroporation efficiency. At $P_C = 5$, we see the gentlest electroporation results, with 34.1% efficiency and 58.6% viability. At larger P_C values of 10 and 20, the viability decreases significantly to 46.1 and 19% respectively. Efficiency increases slightly at $P_C = 10$ to 39.2% but decreases to 35.0% at $P_C = 20$. The high standard deviation at $P_C = 20$ can be explained by the low cell viability, as efficiency is calculated by dividing the electroporated cells by the total viable cells. Cell count was normalized to the 00V condition for each trial.

3.3.4. Transfection via Cytosolic Plasmid Delivery

We further attempted to transfect our L1210 cells with ZsGreen, a plasmid for creating a

fluorescent protein. We chose ZsGreen because fluorescent proteins enable easy identification

of transfection events. As a control, we tested transfection efficiency on an Eppendorf

Electroporator. However, in contrast to our customized electroporation setup, the only variable

we could change was the applied voltage, and thus the magnitude of the electric field. To test

comparable conditions, we matched the electric field values of the device on the Eppendorf

Eporator. We tested conditions of 0.5 kV/cm, 1 kV/cm, and 1.5 kV/cm. We found that at 1 and

1.5 kV/cm, we could transfect cells with a 3% and 7% transfection efficiency, respectively. While

these efficiencies are low, this could reflect intracellular degradation or insufficient nuclear targeting of the plasmid [76], [192].

We then tested our on chip transfection efficiency with conditions we had identified from the PI delivery experiments (15 V P-P voltage, a 0.5 ms P_W, and 5 and 10 pulse P_C). However, we saw no events of transfection in collected cells. Previous work had shown that due to an increase in cargo size, from fluorescent molecules to plasmid, we would need a stronger electric field to transfect trapped cells [80]. Based on the results of the real-time electroporation results, we increased the pulse width to 1 ms, and observed transfection events. While we did not achieve the 7% efficiency observed using traditional cuvette electroporation, these results show it is possible to transfect cells with our device. Further work should be done to increase transfection efficiency, such as increasing plasmid concentration and plasmid incubation time.

3.4. Conclusion

In this work, we designed electrodes to integrate electroporation with new microfluidic Vortex trapping devices to deliver biomolecules to L1210 cells. We next use real-time fluorescent intensity images to narrow the scope of our investigation from three parameters of the electric field (pulse width, pulse count, and voltage) to one: fixing pulse width and voltage, only varying the pulse count. We then analyzed the cells and found that at a condition of 15 V P-P, with a pulse width of 0.5 ms, and a pulse count of 5, we could gently electroporate cells, and deliver membrane impermeable PI, with a 64% viability and 30% efficiency. Finally, using the knowledge gained from our real time fluorescent imaging investigations, we were able to modify our electric

field by increasing the pulse width to 1 ms and observe transfection of L1210 cells with the ZsGreen plasmid.

Future work can be done to further optimize plasmid transfection, by increasing external parameters such as plasmid concentration and incubation time. More efficient transfection vectors such as protected plasmids or ribonucleoproteins should be investigated for a higher transfection efficiency [76].

Chapter 4. Modifying the Electrode – Integrated Vortex Chip Fabrication Protocol with a Commercialization - Friendly Processes

4.1. Introduction

Microfluidic devices have been investigated in academic settings for many purposes, such as analyte concentration for reliable diagnostic assays [193], [194] and detection of chemical ions in environmental sampling looking for hazardous compounds [195]. While these devices are widely used in academia, they face challenges during the translation to commercial settings, due to difficulties in scaling up fabrication, and the integration of supporting components required to operate microfluidic devices, such as electric field generators.

A pivotal moment in microfluidic research was the development of the soft lithography, which uses polydimethylsiloxane (PDMS) to cast microfluidic devices [196]. This was significant because it removed time and cost limitations of creating microfluidic devices from silicon [197]. Additionally, PDMS offers unparalleled flexibility for rapid prototyping, with its low fabrication cost (< $100) and quick turnaround time (days, if not hours) [198]. However, PDMS critically limits the ability to scale up manufacturing of microfluidic devices due to time and cost requirements of PDMS manufacturing, compared to manufacturing processes of more established commercial materials such as polycarbonate (PC) and polymethyl methacrylate (PMMA) [40], [41], [199], [200]. Thus, the fabrication of microfluidic devices using PMMA and PC is a topic attracting research interest [201]. Based on the needs of the device (integration of electrodes, integration of immunoassay, need for a dielectric, or placement of valves), the fabrication of each device will vary drastically [201]–[203] .Thus, a critical step to commercializing microfluidic devices is to

design a fabrication pipeline using materials such as PMMA that have established commercial manufacturing processes.

Another consideration for commercializing microfluidic devices is the consolidation and packaging of required components to operate a microfluidic device (such as syringe pumps, pressure drivers for the fluid, and electric signal generation) in a single self-contained unit [40], [108]. This is particularly true when these components are used to provide a secondary functionality, such as on-chip electroporation. In an academic setting, these secondary functionalities are provided by large, bulky equipment such as waveform generators, that cannot be integrated into a self-contained unit [76], [80]. However, to commercialize these valuable, multifunctional microfluidic devices, it is critical to miniaturize the equipment needed to provide these functionalities, such that they can be consolidated and packed in a self-contained unit.

Vortex microfluidic devices have been commercialized by Vortex Biosciences, successfully transitioning from PDMS devices to PMMA devices, and housing all associated hardware in a single self-contained unit [204]. This device provides the critical functionality of isolating circulating tumor cells (CTCs) in a label free manner [54], [205], [206]. These devices have continued to be developed in academia to investigate integrating electrodes to perform on-chip electroporation and biomolecular delivery of nucleic acids [76], [80], drugs [78], [79], and protein conjugates [80]. However, the integration of these electrodes with the Vortex devices has only been done with PDMS based devices, which enables rapid prototyping for channel design modification. PMMA and PC fabrication methods such as injection molding require molds that are often machined and complex to fabricate [200]. Critically, this means that the electrode fabrication protocol was optimized PDMS fabrication but not with PMMA or PC fabrication

processes, limiting the integration of these features and functionalities to an academic setting. Additionally, the waveform for electroporation is generated using large, bulky, and costly equipment that cannot be packaged with the device in a commercial setting [76], [80]. It is desirable to modify the electrode-integrated Vortex chip fabrication protocol and the waveform generation such that they are compatible with commercial processes. This means that the fabrication process should be compatible with standardized industrial processes such as hot-embossing, photolithography, and electroplating. Additionally, a waveform generator should be designed such that it does not require large, external equipment, but rather miniaturized so that it can be included in a self-contained unit.

In this work, we conceived of a fabrication pipeline that uses lithography, embossing, and electroplating to fabricate a PMMA microfluidic device with embedded electrodes. Critically, these processes were chosen because they are compatible with current industrial fabrication processes and can be easily scaled up for commercialization. We further investigate the effects of varying process parameters in the fabrication processes. For these investigations, we use the microfluidic device described in Chapter 2. Second, we miniaturize the waveform generator, from two large independent instruments costing >$6,000 to two printed circuit boards (PCBs) that measure 63 mm x 78 mm, cost <$150, and operates in a wider voltage range than its commercial counterpart. We believe that these are critical steps towards the commercialization of integrated on-chip electroporation for Vortex devices, thus expanding their capabilities in commercial and clinical settings.

4.2. Materials and Methods

4.2.1. Fabrication of Embossed Vortex Device

To fabricate the copper master mold of the device described in Chapter 2, we performed traditional photolithography on a copper substrate, with one caveat. Compared to a mask for a silicon/photoresist master mold which results in positive features, the mask for photolithography for copper mold fabrication resulted in negative features. This is critical because the positive features on the copper mold will be created using electroplating, to create a durable mold with high fidelity over multiple device fabrications. Briefly, mirror-like 110 copper was purchased (McMaster-Carr, USA), spin-coated with KMPR 1050 photoresist (Kayaku Advanced Materials, USA) to a height of 50 μm, and exposed to UV through a patterned mask (CasOutput City, USA). The exposed photoresist was cured, and excess photoresist was removed by SU-8 Developer (Kayaku Advanced Materials, USA).

To create the positive features used for embossing, we electroplated copper onto the exposed regions of the master. For electroplating, a current source (E3630A Triple Output DC, Hewlett Packard, USA) was connected to the mold and a copper source. The mold and the copper source were held at a constant distance by a custom-built 3D printed sample holder. The plating solution used was EarthGold Plating Solutions – Bright Copper (Gesswein, USA). The electroplating took place in a 1 L beaker, and a stir bar was used to provide constant agitation of the solution, at a current density of 0.21 mA/mm^2. After the electroplating, the photoresist was removed using Remover 1165 (Kayaku Advanced Materials, USA).

To create a flat surface, the final sample was polished in an Allied Multi-Prep Polisher (Allied High Tech Products Inc., USA), using 3-micron aluminum oxide lapping paper. The master was embossed into a 1/8" PMMA sheet (McMaster-Carr, USA) using a Strongway Benchtop Hydraulic Shop Press (Northern Tool + Equipment, USA) and Rosin Heated Press Plate Kit (Vevor, USA).

4.2.2. Electric Waveform Generator Miniaturization

The electroporation box that provides the waveform required to electroporate cells was designed using an MSP430F5529 (MSP430) (Texas Instruments) and a custom printed PCB (OSHPark). The integrated IC chips were sourced from DigiKey and Mouser Electronics. The housing case for the box was sourced from Polycase. A custom PCB was designed using EagleCAD (AutoDesk, USA), and sent to OSHPark (USA) for fabrication. On one panel of the housing, there is an input for a MicroUSB cable to power the MSP430, and an input each for the negative and positive high voltage supply (E3630A Triple Output DC, Hewlett Packard, USA). On the adjacent panel, there are two output slots for the output waveform. There are also two lights on this panel, one to indicate if the box is plugged in, and an in-operation light that will turn on only when the box is in operation. The in-operation light is activated by a button on that same panel, that also triggers the electroporation waveform.

4.3. Results and Discussion

4.3.1. Designing the Fabrication Pipeline

We created a pipeline to fabricate our electrode integrated Vortex trapping device that uses lithography, electroplating, and hot embossing. These processes were chosen because they

can be scaled up to manufacture devices in bulk, thus in-line with our goal of designing a commercialization friendly protocol [199].

Previous work showed that electrodes can be anchored into a PMMA substrate, and the device mold can then be embossed into the PMMA, bending the electrodes to create a fluidic channel surrounded by electrodes [207], [208]. By embedding the electrodes first then embossing the channel into PMMA, this creates a 3-D electrode configuration which would provide a more uniform electric field. However, this was used to pattern electrodes in narrow microfluidic channels and could be done by simply patterning one side of the PMMA with electrodes. To emboss electrodes around our wider cell trapping chambers, we designed electrodes such that they are embedded into both sides of the PMMA. In doing so, we could take advantage of the 3-D electrode configuration and increase the uniformity of our electric field.

When we evaluated this protocol for our device, we identified a potential improvement to the pipeline. In the original fabrication process, the group used Si wafers as the substrate for hot embossing the channel mold [208]. However, due to the brittle nature of Si wafers, it is desirable to make the master out of a more robust material, capable of withstanding multiple embossing and de-embossing steps [209], [210]. Previous groups investigated nickel as a robust material as a material for the master mold [211], [212]. However, de-embossing nickel was difficult, and often resulted in stiction. Another group investigated copper as the master mold material. The channel mold was created using photolithography to create the pattern and electroplating to create the features to be embossed [213]. Their investigation showed that compared to nickel, copper performed better in the embossing and de-embossing process. Thus, we investigated a protocol to fabricate the master mold out of copper.

The final protocol used lithography, electroplating, and polishing to fabricate both the channel mold and the electrodes. A schematic of the final protocol can be found in Figure 4.1 and Figure 4.2. Figure 4.1 depicts the process of creating the molds for the channel and the electrode. For both, we start with a substrate. The channel mold will use a copper substrate to promote good adhesion, creating a robust and durable channel mold. The electrodes will use a stainless-steel substrate because electroplated copper has poor adhesion to the stainless-steel surface [214] and will facilitate electrode lift-off and anchoring into the PMMA surface. The substrates are coated with KMPR 1050 and using traditional photolithography, the patterns are created on the photoresist. The exposed surfaces are then plated with copper. Critically, the copper plated onto the device mold is plated to a height less than the photoresist (Figure 4.1C). However, for the electrodes, the plating height is taller than the photoresist, to encourage the growth of hook-like features and facilitate the anchoring of the electrodes in the PMMA (Figure 4.1D). Lastly, after the deposition, the KMPR was stripped, leaving the plated features. These features on the channel mold were then polished to ensure the evenness of the plating profile.

After the mold fabrication process was defined, we turned to the embossing step. First, the electrodes are embedded into a blank PMMA substrate using hot embossing. The hook-like features and poor adhesion between the copper and the stainless steel promote the anchoring of electrodes into the PMMA (Figure 4.2B). After embedding, the exposed areas of the electrodes are then plated first with Ni, then with Au. This is critical because Au is the preferred metal for electrodes as it will not degrade and leach toxic metal particles into the device [38]. Ni is added to act as a barrier between copper and gold, to prevent diffusion of copper into the gold surface [215].After the electrodes are embedded into matching pieces of PMMA, the channel mold is

57

embossed into the PMMA, bending the electrodes. Lastly, the two matching pieces of PMMA are bonded together using thermal bonding methods to create a sealed microfluidic channel.
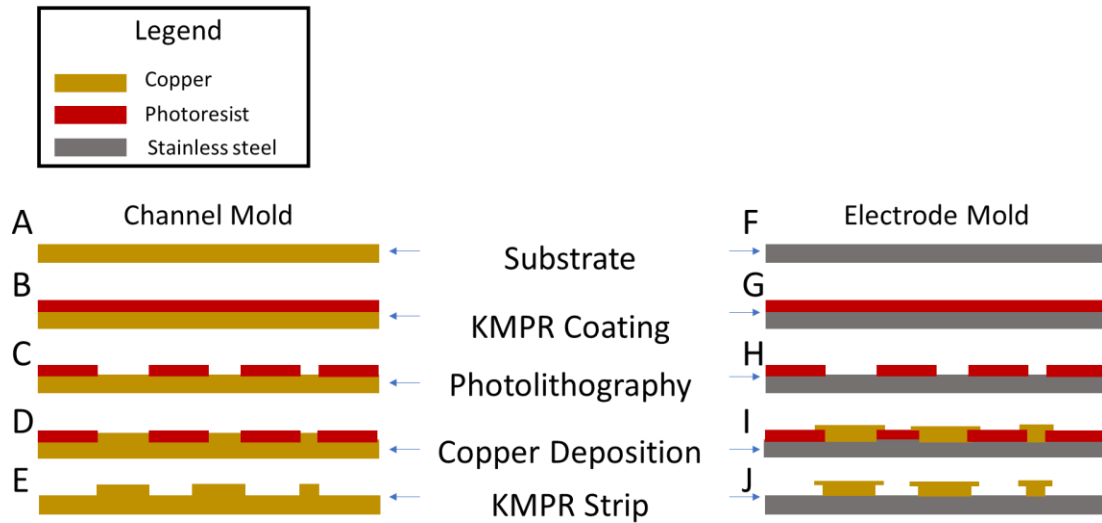
Figure 4.1 Overview of the channel mold and electrode fabrication. A) shows the substrates for the different fabrications. For the channel mold, the substrate is a copper wafer, but for the electrodes, the substrate is a stainless steel. This is done to facilitate the lift off of the electrodes into the PMMA, as copper electroplated onto stainless steel would have poor adhesion. However, for the channel mold, we want the master to remain intact after the embossing and de-embossing process. B-C) show the KMPR lithography step. KMPR is spin coated at a prescribed height and lithography is used to pattern the photoresist. D) is the result of copper deposited on the exposed area of the substrates. Note, in the channel mold fabrication, the plating is shorter than the photoresist but in the electrode mold, the plating is taller than the photoresist, allowing for hook like features to form. E) is the final photoresist stripping using Remover 1165.
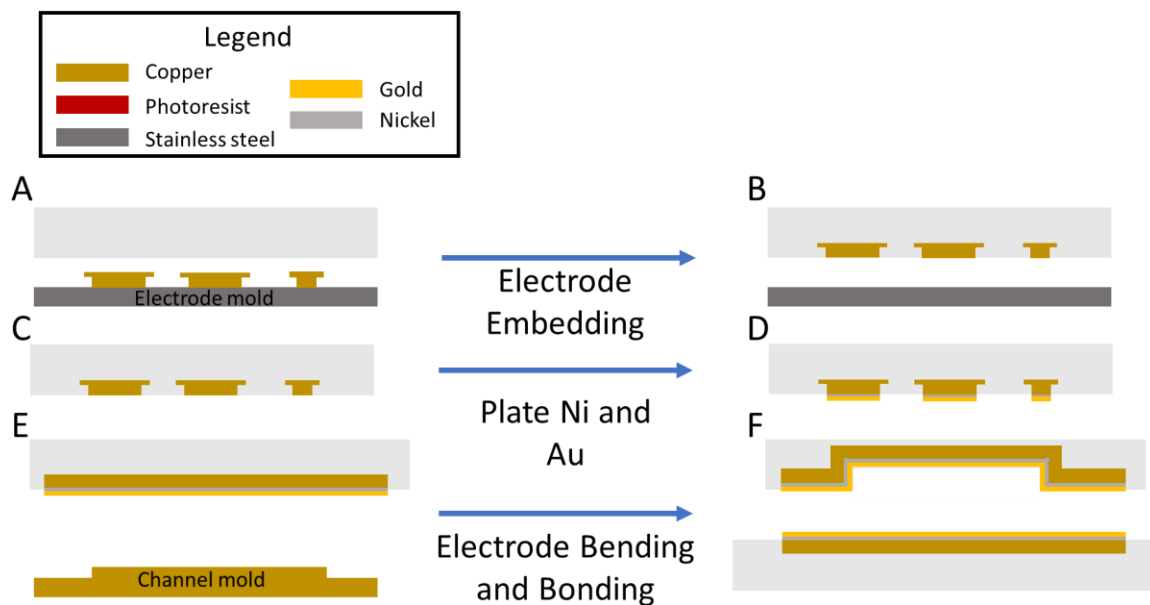
Figure 4.2 Overview of the embossing and electrode bending process. A-B) shows that the electrodes are embedded into the PMMA, due to the hook-like features and the poor adhesion between the stainless steel and copper. C-D) shows that the

58

4.3.2. Optimization of KMPR Lithography on Copper Plating

The first step of the fabrication process was to use UV lithography to create the desired pattern in the photoresist. This is critical because the photoresist is used as a masking material, protecting regions of the mold from electroplating. The target photoresist height was 50 μm, which required spin rate was found to be 2,000 RPM, and an exposure energy of 1,250 mJ/cm^2. Critically, we used a long pass filter to block UV radiation below 350 nm, as wavelengths below 264 nm could induce a photoelectric effect from copper [216]. Preliminary results showed that the KMPR had poor adhesion to the copper, and the cured photoresist washed off the substrate. Attempts to enhance the adhesion through harsh surface plasma treatment (300W, 5 minutes), while initially thought to be successful, resulted in copper nitride forming on the copper substrate. Unfortunately, these defects could not be overlooked as at they caused the electroplating to fail at these locations. Finally, we limited the development time to 6 minutes and could remove most of the uncured photoresist. However, there was still some residual photoresist in the microfluidic channel. This residue was significant as it would prevent copper from plating in the microchannel. To remove this, we exposed the mold to more gentle plasma treatment (150 W, 3 min). This was shown to remove the residue in the microchannel, without leaving copper nitride residue.

4.3.1. Investigating Parameters of Electroplating and Polishing

The next step in the process was to electroplate the copper and create the features on the master mold toe emboss into the PMMA. We constructed a sample holder that would hold

two 3" x 3" plates of copper at a constant distance of 1" apart. This was critical in ensuring that the distance, and thus, the electric field between the anode and the cathode was constant. For these experiments, the mold was connected to the positive terminal of the power supply and acted as the cathode. A blank 3" x 3" copper plate was used as the anode, or the copper source, and connected to the negative terminal of the power supply. The sample holder was 3-D printed, and the back of the anode and cathode were taped, to prevent those surfaces from plating and distorting the electric field.

We tested a variety of conditions both for the applied current and voltage, and the setup itself. In previous electroplating investigations, the parameters for current and voltage were reported in terms of current density and had shown that a current density of 0.21 mA/mm^2 was optimal for plating copper [213]. A higher current density would lead to faster plating, but also results in hydrogen bubble formation which would then be trapped within the plated copper, leading to bubble like structures. At an area of 1,104.3 mm^2, the applied current to reach a density of 0.21 mA/mm^2 was 231.9 mA. At these conditions, we observed that the plating surface in the middle of the device was even, and the plating rate was found to be 0.03 mm^3/mAh. At this rate, it took approximately 2.5 hours to reach a height of 15 μm. However, we noticed that towards the edges of the device, the plating height was taller than the plating height at the center, likely due to the current edge effect. In a device with a height of 15 μm, we found that the edge heights were approximately 23 μm, or 53% greater than the height at the center of the device. To overcome this, we polished the sample to increase the evenness of plating height. We reduced the maximum height at the edge of the channel to 18 μm, or 20% greater than the height at the center of the device. Importantly, in a region of the device that is 800 μm wide, heights of

> 16 μm is only observed 50 μm from either edge (Figure 4.3). Thus, the portion of the device with a height variation of > 1 μm is observable in 12% of the width of the device. This variation in height was also only observed in the widest portions of the device (the inlet and the chamber). The microchannel (25 and 15 μm wide) heights were found to be consistent with the heights in the center of the device.

Further work to optimize this should be focused on achieving a more uniform plating result. Other reported ways to improve plating uniformity include increasing agitation, plating at higher temperatures, using pulsed plating, or using a baffle plate [217]. Increasing agitation and pulsed plating both disrupt the diffusion layer (the region close to the material to be plated, depleted of Cu^{2+} ions) [218], [219]. Heating the solution has been shown to reduce the thickness of this zone. A baffle plate more evenly distributes the electric field, reducing the current concentration at the edge of the feature [220]. While these optimizations offer improvements, our results show promise that even with our current electroplating system and post-electroplating polishing step, we can minimize device height variation and fabricate a functional master mold.
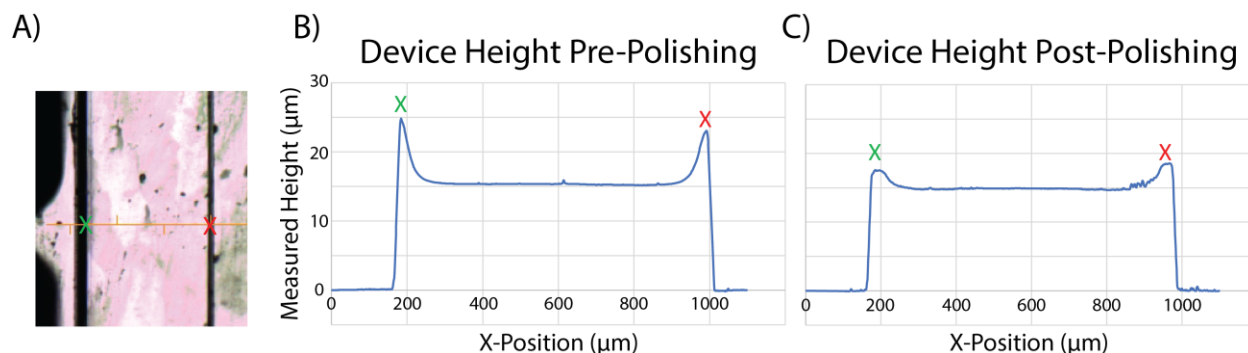
Figure 4.3 Heights of plated copper pre – and post – polishing. A) Shows the location of measurements. Approximately 1,250 μm were measured in the lateral direction. The green cross and red cross correspond to X-Positions of ~ 160 μm and ~980 μm respectively. B) shows the height profile of the copper, just after electroplating. C) shows the height profile of the copper post

4.3.2. Investigating Embossing Parameters

The final process step we investigated was embossing the mold into PMMA. This investigation would be useful in both the electrode and channel embossing steps. Previous work had shown that the surface pretreatment, embossing pressure, temperature, and time all affected the quality of the final product [207], [213].

To match previous work, our target embossing force was 1,350 N (42.96 PSI for a 3" x 3" plate), at a temperature of 130°C, for 5 minutes [213]. However, this resulted in very poor imprint into the PMMA. For features with heights of >20 μm, the embossed PMMA had depression depths of only 3 μm. One possible explanation for this is that due to limitations in the gauge resolution of our press, it failed to accurately resolve pressures under 4,500 N. To overcome this, we first increased embossing pressure to the minimum 4,500 N (143.2 PSI), however this still resulted in poor imprinting.

In addition to increasing the pressure, we also investigated the effects of the embossing temperature. PMMA has a wide range of glass transition temperatures, the temperature above which the polymer becomes a viscous liquid and thus more malleable [221]. We further increased the temperature to 140°C and were able to observe depressed, embossed PMMA depths consistent with feature heights. However, there was a slight protrusion outside of the feature. Further investigation showed that this was a result of stiction and could be eliminated by holding the pressure until the PMMA and copper plates cooled to below 80°C. This allows the PMMA to solidify, before releasing the pressure, and the stiction is not as prominent.

Future work into embossing parameters should seek to optimize the embossing result, free of defects. After the embossing step has been optimized, the learning should be translated to the bonding step, to ensure that two pieces of PMMA can be bonded together to create a sealed microfluidic device. Previous work has used pretreatment of the PMMA pieces using organic solvents (isopropanol, acetone) and plasma treatment to increase bonding strength and efficiency, thus ensuring a sealed channel capable of withstanding high pressures up to 11 MPa [222], [223], more than sufficient to operate the Vortex device [79], [80].

4.3.3. Miniaturization of Electrical Waveform Generation

We separately worked to miniaturize the waveform generator required to produce the electric field to permeabilize the cells. Previous work used an Agilent 33120A Arbitrary Waveform generator and an Agilent 8110A pulse driver [80]. Combined, these instruments cost more than $6,000 and have a minimum footprint of 462 mm x 521 mm, which makes integration into a self-contained packaging difficult. A solution to this is to miniaturize the circuitry and facilitating integration into a self-contained package, but without compromising on the functionality and programmability of the waveform (see Chapter 3 for more information regarding the programmable parameters of the waveform).

To accomplish this, we used an MSP430 microcontroller for the signal control. Using an internal pulse width modulation (PWM) waveform on the MSP430, we were able to create a square wave, and modulate its frequency. This signal, as well as other MSP430 outputs and logic chips, controlled 8 optocouplers that separated the low voltage and high voltage side of the chip. These optocouplers were then used to drive larger power metal-oxide semiconductor field-effect transistors (MOSFETs). The MOSFETs create an H-Bridge on the high voltage side of the chip that

switches the polarity of the voltage supplied to the microfluidic chip. This allowed us to miniaturize the circuitry required from two large instruments that have a minimum footprint of 462 mm x 521 mm, to two printed circuit boards, measuring 63 mm x 78 mm, and can be easily integrated into existing instrumentation.

4.3.4. Increasing the Operational Voltage Ranges

Critically, while redesigning the pulse driver mechanism, we also wanted to increase the voltage ranges we could test for electroporation. Previously, this was limited to 40 V peak to peak (P-P) with the Agilent 8110A [80], but the custom bipolar pulse driver mechanism increased those limits to 60 V P-P. To create a versatile device capable of driving electroporation of smaller cells without concerns about the maximum voltage applied, we designed a device that could operate at ranges from 10 V P-P to 120 V P-P. The important feature that we had to redesign was the voltage regulator that regulates the gate voltage of the MOSFETs. Commercial linear regulators often use variable resistors, whose values need to be mechanically changed to change the effective resistance.

An attractive alternative to the traditional linear regulator is the Zener diodes. These diodes operate as traditional diodes with one caveat – in the breakdown region, these diodes provide a constant voltage drop for a wide range of currents. This means a single value resistor can regulate the voltage drop across the Zener diode for a wide range of input voltages and provide a sufficient voltage differential to drive the gates of the four MOSFETs. We selected Zener diodes that can provide a voltage drop of 15 V, and are rated for 1 W. These were used in series with a 1.3 kΩ resistor. The resistance was calculated according to the following equations:

$$P_Z = V_Z * I_{Z,MAX} \tag{4.1}$$

$$V_R = 0.5 * I_{Z,MAX} * R \tag{4.2}$$

In Equation $P_Z = V_Z * I_{Z,MAX}$ (4.1, P_Z is the maximum

Zener power rating (1 W), V_Z is the Zener voltage required (15 V) and $I_{Z,MAX}$ is the maximum

current through the Zener diode (67 mA). In Equation $V_R = 0.5 * I_{Z,MAX} * R$

(4.2, V_R is the voltage drop across the resistor (for a 60 V input, 120V P-P, we desire a 45 V drop

across the resistor), and R is the resistance of the resistor. To ensure that the Zener diode will

work across the range of voltages we require, we fix R and V_R, and calculate I_Z which is the current

across the Zener diode (note, not 0.5*$I_{Z,MAX}$). We can then compare the I_Z value to the minimum

I_Z value for the Zener diode ($I_{Z,MIN}$) to ensure that it is still within the operating range of the Zener

diode. In this case, at a minimum of 5 V input (10 V P-P), I_Z = 3.5 mA, while $I_{Z,MIN}$ < 2.5 mA. Thus,

we were able to construct a voltage regulator capable of regulating the voltage in the range of

10 – 120 V P-P, without the need for mechanical tuning of the resistor.

4.4. Conclusion

In this work, we investigated how we could better facilitate the adoption of electrode

integrated Vortex devices in industry. Previous electrode integrated Vortex chips were fabricated

using PDMS microfluidic devices and electrodes patterned on glass slides using the traditional

lift-off fabrication process [79], [80]. However, these devices are not compatible with the

commercial needs of standardization and are difficult to scale up. We conceived of a new pipeline

for fabricating the electrode integrated Vortex device using the standard industrial processes of

lithography, electroplating, and hot embossing. We further investigated parameters of these

processes to optimize the fabrication of the master mold and the embossed chip. Lastly, we

miniaturized our waveform generator such that the final product can be easily integrated into a

unified instrument.

Chapter 5. Development of a Physiologically Similar Phantom for Oblique Back-Illumination Capillaroscopy

5.1. Introduction

In vivo imaging can be used to non-invasively examine organs [224], [225] and blood vessels [226] for signs of damage and infection. When developing *in vivo* imaging modalities, a key step in technology evaluation is testing the proposed technique on an *in vitro* phantom that mimics the relevant properties of the tissue [227]–[229].

Recently, an optical imaging method known as oblique back-illumination capillaroscopy was developed to image blood cells flowing within capillaries *in vivo* [230]. This technique allows clinicians to determine complete blood counts (CBCs) without the need for drawing blood samples in a traditional hospital setting. Thus, clinicians may perform CBCs without requiring immunocompromised patients to come into the hospital and risk infection, or to remove precious milliliters of blood from neonates, risking iatrogenic anemia [109]. One possible way to do this is to use a recently developed imaging technique known as oblique back-illumination capillaroscopy to identify blood cell subpopulations to perform *in vivo* CBCs. A critical step to achieve this is to obtain ground truth data of visualizing blood cells *in vivo* using oblique-back illumination capillaroscopy [231], [232]. This ground truth data can be obtained with the aid of optical phantoms, through which known subpopulations of blood cells can be flown, imaged, and classified.

Many phantoms have successfully mimicked the optical properties of bulk tissue [228]. However, phantoms that allow blood flow at physiologically relevant rates and mimic the optical properties of the tissue have been difficult to fabricate. Previous groups have used embedded

glass microcapillaries or plastic tubing to create these capillaries [233], [234]. However, these channels tend to be wider than the single capillaries that oblique back-illumination capillaroscopy seeks to image. Additionally, these microcapillaries distort the optical properties of the phantom by introducing non-scattering material surrounding the fluidic channel.

An attractive alternative is the use of microfluidic phantoms, which allow unparalleled control over the channel widths and designs [235]–[237]. These devices are often cast in polydimethylsiloxane (PDMS), a polymer that is easy to mold and dope with scattering and absorption agents. Additionally, they do not require glass or plastic microcapillaries to create channels for fluid flow, thus preserving the optical properties of the phantom. One significant drawback of current designs, however, is that to create a sealed channel, these devices are often bonded to glass slides [235]. Any imaging is done on these devices are done through a non-scattering medium, again distorting the imaging properties.

In this work, we investigated the fabrication of tissue realistic phantoms that permit blood flow at physiologically relevant rates. We created a microfluidic device cast in PDMS doped with TiO_2 and India Ink to mimic the optical properties of bulk tissue. We sealed the microfluidic channel with a thin, height controlled PDMS membrane (Figure 5.1). This allowed us to image capillary sized microchannels at depths similar to capillaries under the oral mucosa (~100 μm) or the nailfold (~500 μm) [109], through membranes with tissue-like optical properties. Critically, by changing the concentration of dopant, we mimicked absorption and scattering properties of different skin types [238]–[240]. The fabrication methodology also allowed the capillary height and optical properties to be changed by adjusting the membrane height and dopant concentration, respectively. We believe that this work is a significant step in the development of

tissue realistic capillary phantoms that allow us to image flowing blood cells through microchannels sealed with a doped PDMS membrane, as it closely mimics *in vivo* imaging conditions.
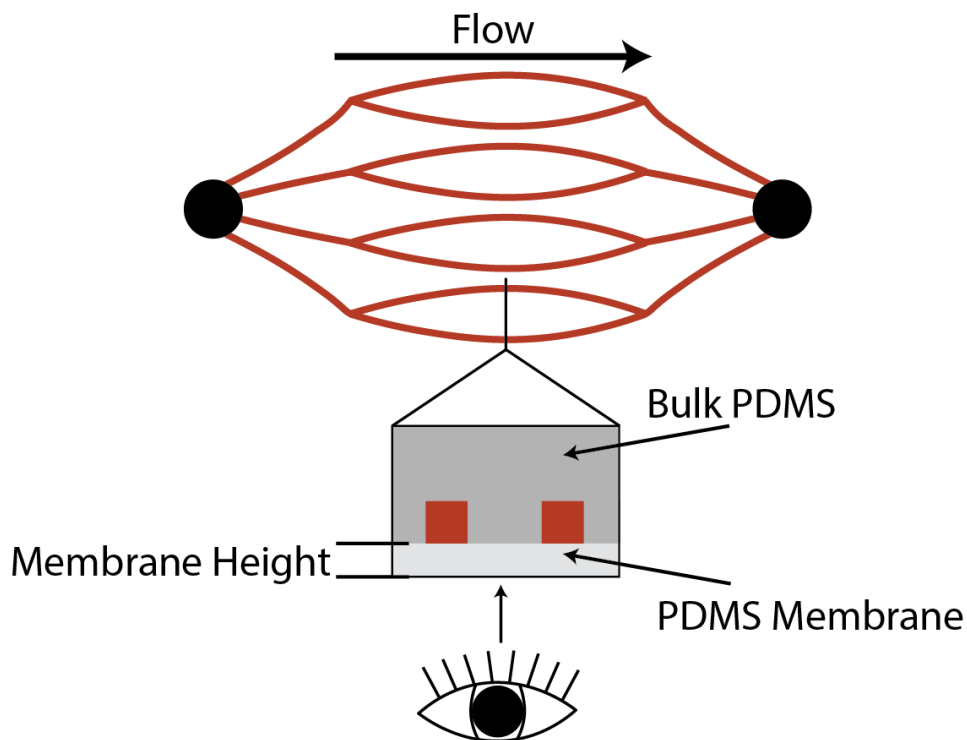
Figure 5.1 Overview of the PDMS platform to simulate imaging blood in capillaries in vivo. The bulk PDMS is doped with TiO_2 and India ink to mimic bulk tissue and cast on top the channel mold. The membrane is PDMS doped with a different ratio of TiO_2 and India Ink, spin coated on a wafer and bonded to the bulk PDMS, creating a sealed microfluidic channel capable of sustaining blood flow at physiologically relevant rates. The dopant concentration and spin speed of the PDMS membranes can be varied to mimic different skin types and capillary depths, respectively. The capillary is then imaged through the membrane, to mimic imaging of in vivo capillaries.

5.2. Materials and Methods

5.2.1. Microfluidic Device Fabrication

The microfluidic device was designed by the Durr Lab at Johns Hopkins University (Figure 1). The device had an initial channel width of 1 mm, which then narrows into 32 branches of 15 µm widths. These channels then recombine towards the outlet. The height of the device was a uniform 15 µm to form microcapillaries with square cross sections. Devices were fabricated using

standard soft lithography. Briefly, a photomask of the channel was designed using SOLIDWORKS, and fabricated by CASOutputcity (USA). KMPR1035 photoresist (Kayaku Advanced Materials Inc., USA) was spin coated onto a silicon wafer, and the photomask pattern was transferred to the photoresist using photolithography. To create the base, a 1:10 ratio of PDMS prepolymer: curing agent mixture was prepared with a fixed ratio of 50% (w/v) TiO2 and 18% (v/v) India ink and then cast onto the patterned wafer to create the microchannel. PDMS replicates were cut and separated from the wafer, and inlet and outlet holes were punched using a blunt 20-gauge needle.

To create the membrane, another silicon wafer was coated with S1813 photoresist (Shipley, USA) to a height of 2 μm and cured. Different ratios of TiO_2 and India Ink were mixed with 1:10 PDMS to obtain different optical properties. The doped PDMS was spin coated on top the wafer. The exact heights of the spin coated membrane and dopant material determined the depth of the capillary and the optical properties of the material to be imaged through, respectively.

Once the membrane had cured, the bulk PDMS channel was bonded to the membrane using O_2 plasma bonding to create a sealed microfluidic channel. (O2 plasma bonding conditions?) The entire device (wafer, membrane, and bulk channel) was placed in the oven at 80°C overnight. To detach the wafer from the device, the membrane was cut, and the entire device was placed in an acetone bath, where acetone levels were lower than the inlet.

5.3. Results and Discussion

5.3.1. Creating a Biologically Realistic Phantom

Previous microfluidic phantoms were sealed with glass slides that had a fixed height/capillary depth because the microfluidic device was sealed using a glass slide [241] and only permitted imaging through non-physiologically relevant non-scattering mediums [235]. To address these issues, we conceived of a fabrication process to create a microfluidic device, cast entirely in PDMS. The channel was fabricated using standard photolithography techniques. The bulk PDMS was also doped with 50% (w/v) TiO_2 and 18% (v/v) India Ink to completely absorb and/or scatter the incident light. The microchannel is then sealed by a PDMS membrane, as opposed to the traditional glass slide. This PDMS membrane was doped with different concentrations of TiO_2 and India Ink to closely match the scattering and absorption of different skin types. Doping concentrations to match optical properties of skin have previously been reported elsewhere [238]–[240]. Furthermore, the thickness of the PDMS membrane can be tuned to create phantoms for capillaries at different depths (50-500 μm) to mimic capillary depths in oral mucosa (~100 μm) or the nailfold (~500 μm) [109]. By creating a sealed microfluidic channel enclosed completely in doped PDMS, we can create a microfluidic phantom to resemble imaging capillaries for persons with different skin types, and at different locations in the body.

5.3.2. Characterizing the Height of the PDMS Membrane

The ability to vary the membrane properties allows for complete tunability of this device. By varying the membrane height and dopant concentration, we can vary the depth at which the microcapillaries are imaged and the optical properties (scattering and absorbance) of the medium through which they are imaged, respectively. To create a reliable protocol, the height of

the PDMS membrane had to be carefully calibrated at different spin rates. Previous work had

provided a starting point, with the final height given by the equation from [242]:

$$s = 115,900 * (t^{-0.9985}) - 15.09 \qquad\qquad (5.1)$$

where s is the spin speed (rpm) and t is the desired thickness of the membrane (μm). To minimize

the impact of other variables, we standardized the spin time to 1 minute, the ramp speed to 312

RPM/s, and the volume of PDMS to 10 mL. The calibration curve is shown in Figure 5.2.

PDMS Spin Rates vs Membrane Heights, Experimentally Determined
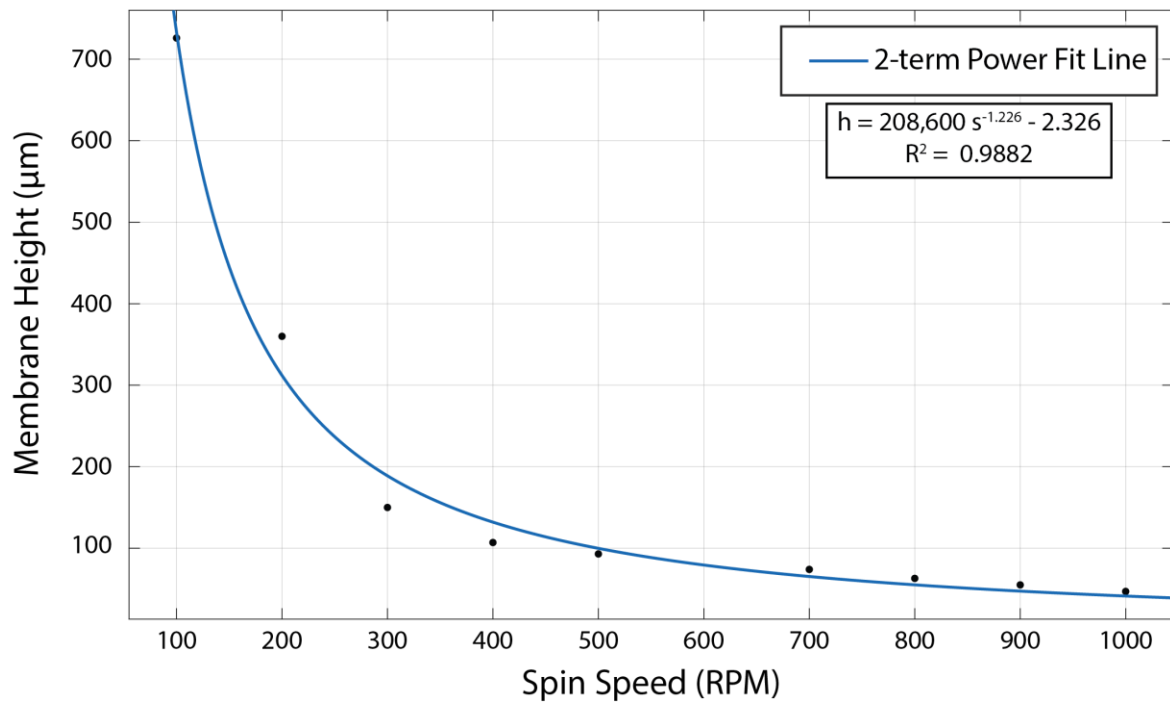
Figure 5.2: Experimental calibration curve for determining spin speed to PDMS membrane heights. Box in the top right also shows the power fit equation, where h is the membrane height in μm, and s is the spin speed in RPM.

Experimentally, for our setup, we found that the height of the membrane was given by:

$$h = 208,600 \ s^{-1.226} - 2.326 \qquad\qquad (5.2)$$

where h is the membrane height in μm and s is the spin speed in RPM. Using this equation, we

could determine the required spin speed to fabricate membranes with desired heights, and thus

capillaries of desired depths. We fabricated doped PDMS membranes with heights ranging from 70 µm to 470 µm to closely mimic the capillary depths ranging from the oral mucosa (~100 µm) to the nailfold (~500 µm) [109]. These membranes were then bonded to the microchannels cast in bulk, doped PDMS using oxygen plasma bonding.

5.3.3. Final Phantom Evaluation

The final phantoms were evaluated by the Durr Lab for their similarity to *in vivo* imaging conditions. Evaluation criteria was based on the ability to maintain physiologically relevant flow rates of blood through the microchannel, and the optimal lateral offsets (ΔX) of the illumination source for given capillary depths. This is critical because the contrast to noise ratio (CNR) is a function of ΔX, and by comparing ΔX of our phantom that maximizes CNR with the ΔX of the tissue that maximizes CNR, we can determine if the phantom and the tissue have similar optical properties (the significance of ΔX is further discussed in [109]). Fresh human blood treated with EDTA was flown through the device at rates ranging from 0 to 6 mm/s. This is encouraging because with the thinnest membrane of 70 µm, we were able to sustain a flow rate of 6 mm/s, which is 6x greater than actual physiological flow in capillaries (< 1 mm/s) [243]. Additionally, the optimal lateral offset of the illumination source, as determined by the highest contrast to noise ratio in the image, for a capillary depth of 70 µm was found to be $\Delta X = 280$ µm. This is similar to the *in vivo* lateral offset of $\Delta X = 225$ µm [230]. These results show that the phantom developed mimics realistic *in vivo* imaging conditions (in terms of physiological flow conditions and optical properties) and can be used to obtain ground truth data for oblique back-illumination capillaroscopy.

5.4. Conclusion

In this chapter, we develop a fabrication technique to create realistic phantoms that can simulate capillary depth and optical properties of the imaging medium, capable of sustaining blood flow at physiologically relevant rates. This is significant because past work relied on either microcapillaries which introduced artifacts into the imaging pathway, or were sealed using a glass slide, which meant imaging had to be done through a fixed-depth, non-scattering medium. In this work, we present a way to create a microfluidic phantom, fully sealed by PDMS. The bulk PDMS and the PDMS membrane can be separately doped with TiO_2 and India Ink to closely resemble the optical properties of the bulk tissue and imaging medium, respectively. The height of the sealing membrane can also be finely tuned to mimic *in vivo* capillary depths, by fabricating membranes with heights ranging from 70 – 470 μm. We believe that with these advances, we can create more robust and realistic phantoms for optical capillaroscopic imaging.

Chapter 6. Investigating the Potential for Using Inertial Microfluidics to Separate Retinal Ganglion Cells in a Label-Free Manner

6.1. Introduction

Glaucoma is a wide-spread degenerative disease affecting approximately 76 million people worldwide in 2020. This number is only predicted to grow, with estimates as high as 111.8 million cases by 2040 [244]. Currently, there is no way to reverse the impacts of glaucoma, namely blindness.

Glaucoma is characterized by the loss of retinal ganglion cells (RGCs), which eventually leads to degeneration and blindness [245]. Until recently, all treatments for glaucoma focused on preventing RGC death, thus slowing the progression of the disease [246], [247]. A major reason for this was the inability to repair or regenerate a damaged nerve. However, recent studies have shown that it is possible to grow complete RGC organoids from induced pluripotent stem cells (iPSCs). This is promising because it opens the possibility to treat glaucoma using cell-replacement based therapies aimed at repairing the optic nerve.

Differentiating iPSCs into retinal cells often result in a variety of retinal and non-retinal ganglion cells (RGCs and nRGCs). Thus, a challenge for further pursuing this technique is differentiating RGCs from nRGCs [248]. Current methods of cell separation rely on identification of biomarkers and attaching labels such as magnetic or fluorescent tags that can then be used to separate out cells identified by these labels. However, these processes, known as magnetic and fluorescent activated cell sorting (MACS and FACS, respectively), are incompatible with current FDA good manufacturing practices, and limit the use of RGC to *in vitro* studies, without the possibility of readministering these cells as for therapeutic purposes [249]. Thus, it is imperative

to develop a label-free method of purification to separate RGCs and nRGCs and overcome a critical barrier in the use of RGCs as a therapeutic tool.

Inertial microfluidic devices have risen to the forefront of cell separation techniques particularly for this reason – these devices rely on biophysical properties of the cell and hydrodynamic forces to separate cells [31], [32]. The inertial hydrodynamic forces act in directions perpendicular to the primary flow direction, and focus cells at distinct equilibrium positions (a full review of these forces can be found in [31], [42], [184]). As the magnitude of these hydrodynamic forces vary with differences in cell properties, cells with different biophysical properties are focused at different equilibrium positions. Once cells are focused, it is possible to direct them to different outlets, thus separating them [44], [250].

In this work, we use a previously reported inertial microfluidic device [44] and evaluate it on its ability to sort RGCs and nRGCs from a heterogeneous mixture, by varying Reynolds numbers. We hypothesized that due to differences in biophysical properties between RGC and nRGC cells, we will be able to direct them to different outlets in the microfluidic device, effectively separating them. We believe that this is critical in overcoming the problem of sorting RGCs for therapeutic purposes to combat the impacts of glaucoma.

6.2. Materials and Methods

6.2.1. Differentiated iPSCs

Frozen mouse iPSCs that had been differentiated into RGCs and nRGCs were obtained from the Zack Lab at Johns Hopkins University. RGC populations were engineered to express

tdTomato. Two different flow solutions were also provided. We tested both Stain buffer FBS (Beckton Dickinson, USA) and Hibernate A (Transnet Tissue YX, USA).

6.2.2. Microfluidic Device Fabrication, Operation, and Analysis

The inertial microfluidic device that was used for sorting RGCs and nRGCs was previously reported in [44]. Inlet and outlet holes were punched using a blunt 20-gauge needle. The inlet was connected to a 10 mL syringe (Becton Dickinson, USA) mounted on a syringe pump (Harvard Apparatus, USA). All experiments were done with initial cell concentrations (both RGC and nRGC populations combined) of 50,000 cells/mL. A syringe pump was used to control the flow rate, and the five separate outlets were collected into 3 different wells. This is because particle behavior was expected to be symmetrical across the channel centerline, thus we expect that outlets in mirrored positions across the channel centerline to have similar cell compositions. The flow rates we tested were calculated based on Re previously used [44]. During device operation, the desired flow rate was entered, and the solution was allowed to flow for 5 minutes to flush the device of unfocused particles. After 5 minutes, we collected 200 μL of solution. The cells were then stained with DAPI and analyzed on a well plate reader for fluorescent signatures. The ratio of RGC to nRGC cells was obtained by calculating the tdTomato^{+}: tdTomato^{-} cells out of all DAPI^{+} cells.

6.3. Results and Discussion

6.3.1. Experiments Varying the Reynolds Number

Based on prior work, we started by calculating the flow rates for different Reynolds numbers (Re). The average flow rate was given by:

$$Q_{Avg} = \frac{Re * \mu * H * W}{2 * \rho * D_H} \tag{6.1}$$

where Q_{Avg} is the average flow rate, Re is the channel Reynolds number calculated using the max flow rate and the hydraulic diameter, μ is the viscosity of the fluid, ρ si the density of the fluid H and W are the channel height and channel width, respectively, and D_H is the hydraulic diameter of the channel. We calculated 3 different Re's – 15, 40, and 50 and assessed these flow conditions on their ability to separate RGC from nRGCs. The collected cells were analyzed via fluorescent imaging. RGC cells were classified as DAPI$^+$/tdTomato$^+$ whereas nRGC cells were classified as DAPI$^+$/tdTomato$^-$. The RGC purity and collection were then determined, and the results are shown in Figure 6.1.

	Re = 15			Re = 40			Re = 50		
Outlets	1 & 5	2 & 4	3	1 & 5	2 & 4	3	1 & 5	2 & 4	3
% RGC	1.1	1.9	0.2	6.0	2.9	0.9	5.2	2.9	1.1
Fold↑ (2.9)	0.4	0.7	0.1	2.1	1	0.3	1.8	1	0.4
RGC Dist%	7	91	2	71	29	0	67	32	1
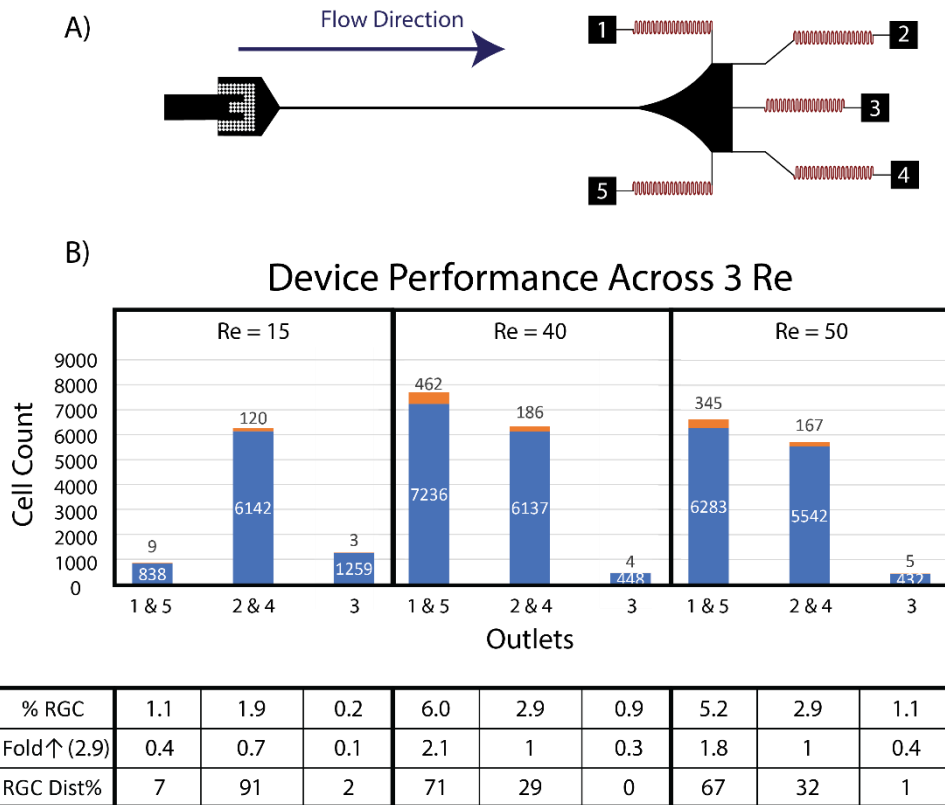
Figure 6.1: Shows the device schematic, as well as the results of cell sorting. A) shows a schematic of the device. B) At Re = 15, we can see that the cells are primarily collected at outlets 2 & 4. However, as Re increased at Re = 40 and Re = 50, more cells were collected from outlets 1 & 5, indicating that cells were focused closer to wall of the channel. Collecting cells at outlets 2&4

At an operational Re = 40, we found that we could collect 70% of the RGCs with a 2-fold increase in purity. This was identified as a promising condition, as we collected the majority of RGCs, along with an increase in purity. While the purity was not high (< 6%), the > 2-fold increase showed promise that the cells could be processed in multiple passes resulting in an increase in purity with each pass. However, when we re-ran the experiment with another population of cells, the results were inconsistent with the preliminary experiment. The comparative results are shown in Figure 6.2.

Comparative Performance at Re = 40

% RGC	2.9	6.6	6.0	9.8	2.9	4.4	5.2	0.9
Fold↑	1.0	1.0	2.1	1.5	1.0	0.7	0.8	0.3
RGC Dist%	-	-	71	92	29	7	1	0
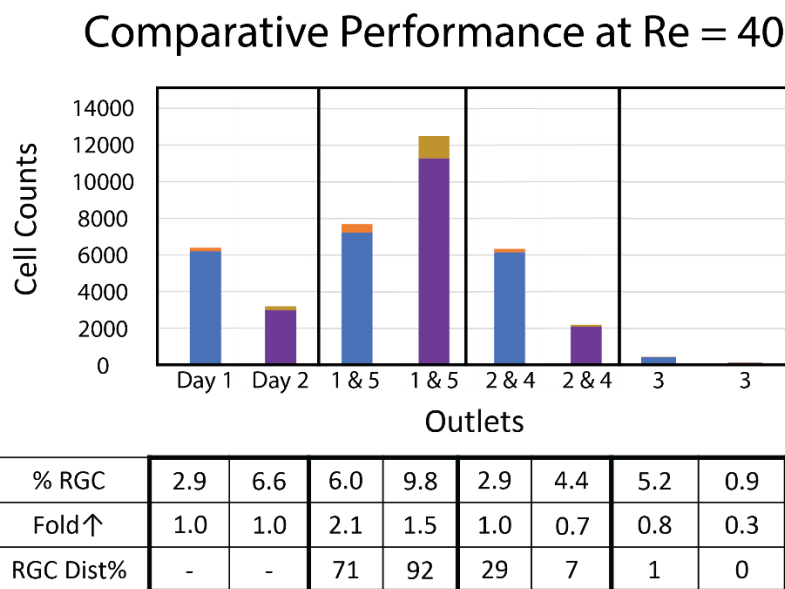
Figure 6.2: Comparison of the experimental results from 2 different days. Day 2 represents the data previously shown in Figure 6.1. The results for the cells collected at outlets 1 & 5 are consistent, however the distribution of the cell population is not consistent. Of the total cell count, on Day 1, roughly 86% of the total cells are collected from outlets 1 & 5, but on Day 2, the only 56% of the total cells were collected at outlets 1 & 5. This indicates that the cells are not focused at the collection, and thus, this is not a reliable and method of sorting RGCs and nRGCs.

Figure 6.2 demonstrates a significant variation in the count at the collection from the outlets over two different days. While the RGC distribution and the purity increase were similar, the percentage of the total cells collected from outlets 1 & 5 were inconsistent. This indicates that cells were not focused at the outlet, as the results were not reproducible.

The results of this investigation show that manipulating flow conditions alone, are not sufficient to separate out RGCs from nRGCs. Further investigations should focus on exploring other avenues of separation. Previous work has shown that it's possible to use non-Newtonian fluids [251], [252] to enhance the focusing position of cells. Additionally, if we can focus these cells at different locations, it is possible that we can achieve the required purity (> 80 %) and recovery efficiency (> 80 %) with multiple sequential separation steps. This is a promising method of separation as it is compliant with the FDAs good manufacturing practices and should be further investigated as a method of separating RGCs and nRGCs, with the end goal of using these cells for therapeutic purposes.

6.4. Conclusion

In this work, we investigated the possibility of separating RGCs and nRGCs from a heterogenous population of differentiated iPSCs, using an inertial microfluidic device, previously used to sort cells based on deformability [44]. However, it was shown that the conditions tested with this device were unable to separate RGCs and nRGCs from a heterogenous population. A potential avenue for further investigation is to use additional forces to focus and these cells at differential focusing positions, such as non-Newtonian fluid forces, and Dean drag forces. Further investigation into separation techniques of RGC and nRGC cells that are approved by the FDA for therapeutic applications would significantly improve the prospects for therapeutic applications of RGCs.

Chapter 7. Conclusion

In Chapter 2, we expanded the capabilities of Vortex trapping to new microparticle populations, specifically targeting microparticles within the 7-10 μm size range, showing that we can achieve a 4-fold increase of particles within this size range trapped within our novel Vortex\ device. We achieved this by manipulating the channel geometry and electrode design within the vortex inertial microfluid devices. This size range is of particular interest because microparticle subpopulations in the pharmaceutical and biological fields that could benefit from Vortex capabilities are in this range. For example, drug particle coating requires multiple solution exchange steps, which can be performed on particles trapped within the Vortex device and minimize the need for sample handling. In biology, cells such as lymphocytes and sperm cells, are within this size range as well and are targets of cell separation, and other downstream capabilities that Vortex trapping offers such as electroporation for biomolecular delivery. By expanding the capabilities of Vortex trapping to these new particle sizes, we can extend the benefits of this robust device to previously unexploited populations.

In Chapter 3, we investigated how changing key features of the Vortex device – the geometry, and target population size, affect the performance of the integrated electroporation process. We redesigned electrodes to better fit our new geometry and amplify the electric field to permeabilize our smaller cell targets. We also investigated the parameters of the electric field and understood how to modify them to better electroporate our smaller cells, and showed that we can electropermeabilize cells with a 34% efficiency and a 56% viability, when delivering fluorescent dye. The integration of electroporation with a Vortex trapping device that targets

cells in the 7-10 µm size range is of particular interest when electroporating and delivering biomolecules to cells such as lymphocytes, sperm cells, and stem cells for therapeutic purposes.

In Chapters 4-6 we explored contributions to the commercialization of electrode integrated microfluidic devices, optical phantoms, and label free RGC sorting. In Chapter 4, we conceived of a new fabrication pipeline compatible with commercialization, and the miniaturization of the required equipment to electroporate cells. In Chapter 5, we designed a new optical phantom with tunable properties, designed to mimic shallow capillaries imaged through thin (100-400 µm) membranes such as those in the oral mucosa or the nailfold. In Chapter 6, we explored the inertial microfluidic, label-free separation of RGC cells, compatible with good manufacturing practices for their use in cell-replacement therapies.

References

[1] H. O. Fatoyinbo, M. P. Hughes, S. P. Martin, P. Pashby, and F. H. Labeed, "Dielectrophoretic separation of Bacillus subtilis spores from environmental diesel particles," *J Environ Monit*, vol. 9, no. 1, pp. 87–90, Jan. 2007, doi: 10.1039/b614556f.

[2] B. Mondal, N. Bhavanashri, S. P. Mounika, D. Tuteja, K. Tandi, and H. Soniya, "Chapter 6 - Microfluidics application for detection of biological warfare agents," in *Handbook on Biological Warfare Preparedness*, S. J. S. Flora and V. Pachauri, Eds. Academic Press, 2020, pp. 103–131. doi: 10.1016/B978-0-12-812026-2.00006-2.

[3] Y. Huang *et al.*, "Separation of Simulants of Biological Warfare Agents from Blood by a Miniaturized Dielectrophoresis Device," *Biomedical Microdevices*, vol. 5, no. 3, pp. 217–225, Sep. 2003, doi: 10.1023/A:1025760209483.

[4] J. Shah and E. Wilkins, "Electrochemical Biosensors for Detection of Biological Warfare Agents," *Electroanalysis*, vol. 15, no. 3, pp. 157–167, 2003, doi: 10.1002/elan.200390019.

[5] A. H. Peruski and L. F. Peruski, "Immunological Methods for Detection and Identification of Infectious Disease and Biological Warfare Agents," *Clinical and Vaccine Immunology*, vol. 10, no. 4, pp. 506–513, Jul. 2003, doi: 10.1128/CDLI.10.4.506-513.2003.

[6] L. Yang *et al.*, "A multifunctional micro-fluidic system for dielectrophoretic concentration coupled with immuno-capture of low numbers of Listeria monocytogenes," *Lab Chip*, vol. 6, no. 7, pp. 896–905, Jun. 2006, doi: 10.1039/B607061M.

[7] A. P. Wacoo, D. Wendiro, P. C. Vuzi, and J. F. Hawumba, "Methods for Detection of Aflatoxins in Agricultural Food Crops," *Journal of Applied Chemistry*, vol. 2014, pp. 1–15, Nov. 2014, doi: 10.1155/2014/706291.

[8] J. O. Chagas *et al.*, "Polymeric microparticles for modified release of NPK in agricultural applications," *Arabian Journal of Chemistry*, vol. 13, no. 1, pp. 2084–2095, Jan. 2020, doi: 10.1016/j.arabjc.2018.03.007.

[9] H. Ullah, M. Badshah, A. Correia, F. Wahid, H. A. Santos, and T. Khan, "Functionalized Bacterial Cellulose Microparticles for Drug Delivery in Biomedical Applications," *Current Pharmaceutical Design*, vol. 25, no. 34, pp. 3692–3701, Sep. 2019, doi: 10.2174/1381612825666191011103851.

[10] M. N. Abu Hajleh, A. AL-Samydai, and E. A. S. Al-Dujaili, "Nano, micro particulate and cosmetic delivery systems of polylactic acid: A mini review," *Journal of Cosmetic Dermatology*, vol. 19, no. 11, pp. 2805–2811, 2020, doi: 10.1111/jocd.13696.

[11] B. Perlatti, P. L. de S. Bergo, M. F. das G. F. da Silva, J. B. Fernandes, and M. R. Forim, *Polymeric Nanoparticle-Based Insecticides: A Controlled Release Purpose for Agrochemicals*. IntechOpen, 2013. doi: 10.5772/53355.

[12] D.-D. Castro-Enríquez *et al.*, "Development of microparticles from wheat glutenins by electrospray and potential application as controlled-release fertilizers," *Bull Mater Sci*, vol. 42, no. 1, p. 41, Feb. 2019, doi: 10.1007/s12034-018-1716-x.

[13] F. Z. Belmokhtar, Z. Elbahri, M. Elbahri, F. Z. Belmokhtar, Z. Elbahri, and M. Elbahri, "Preparation and Optimization of Agrochemical 2,4-D Controlled Release Microparticles using Designs of Experiments," *Journal of the Mexican Chemical Society*, vol. 62, no. 1, Mar. 2018, doi: 10.29356/jmcs.v62i1.579.

[14] D. Vleggaar and U. Bauer, "Facial enhancement and the European experience with Sculptra (poly-l-lactic acid)," *J Drugs Dermatol*, vol. 3, no. 5, pp. 542–547, Sep. 2004.

[15] D. Gittleman, "Composition comprising biodegradable polymers for use in a cosmetic composition," US8968787B2, Mar. 03, 2015 Accessed: Aug. 06, 2022. [Online]. Available: https://patents.google.com/patent/US8968787B2/en

[16] P. K. Sehgal and A. Srinivasan, "Collagen-coated microparticles in drug delivery," *Expert Opinion on Drug Delivery*, vol. 6, no. 7, pp. 687–695, Jul. 2009, doi: 10.1517/17425240903025736.

[17] E. S. K. Tang, L. W. Chan, and P. W. S. Heng, "Coating of multiparticulates for sustained release," *Am J Drug Deliv*, vol. 3, no. 1, pp. 17–28, Mar. 2005, doi: 10.2165/00137696-200503010-00003.

[18] Y. Kaku, S. Fujisawa, T. Saito, and A. Isogai, "Synthesis of Chitin Nanofiber-Coated Polymer Microparticles via Pickering Emulsion," *Biomacromolecules*, vol. 21, no. 5, pp. 1886–1891, May 2020, doi: 10.1021/acs.biomac.9b01757.

[19] A. van de Stolpe, K. Pantel, S. Sleijfer, L. W. Terstappen, and J. M. J. den Toonder, "Circulating Tumor Cell Isolation and Diagnostics: Toward Routine Clinical Use," *Cancer Research*, vol. 71, no. 18, pp. 5955–5960, Sep. 2011, doi: 10.1158/0008-5472.CAN-11-1254.

[20] C. Alix-Panabières and K. Pantel, "Circulating Tumor Cells: Liquid Biopsy of Cancer," *Clin Chem*, vol. 59, no. 1, pp. 110–118, Jan. 2013, doi: 10.1373/clinchem.2012.194258.

[21] P. Gascoyne, J. Satayavivad, and M. Ruchirawat, "Microfluidic approaches to malaria detection," *Acta Tropica*, vol. 89, no. 3, pp. 357–369, Feb. 2004, doi: 10.1016/j.actatropica.2003.11.009.

[22] G. Benton, G. DeGray, H. K. Kleinman, J. George, and I. Arnaoutova, "In Vitro Microtumors Provide a Physiologically Predictive Tool for Breast Cancer Therapeutic Screening," *PLOS ONE*, vol. 10, no. 4, p. e0123312, Apr. 2015, doi: 10.1371/journal.pone.0123312.

[23] M. J. Duffy, "Predictive Markers in Breast and Other Cancers: A Review," *Clinical Chemistry*, vol. 51, no. 3, pp. 494–503, Mar. 2005, doi: 10.1373/clinchem.2004.046227.

[24] S. J. L. Payne, R. L. Bowen, J. L. Jones, and C. A. Wells, "Predictive markers in breast cancer – the present," *Histopathology*, vol. 52, no. 1, pp. 82–90, 2008, doi: 10.1111/j.1365-2559.2007.02897.x.

[25] J. M. Reuben, S. Krishnamurthy, W. Woodward, and M. Cristofanilli, "The role of circulating tumor cells in breast cancer diagnosis and prediction of therapy response," *Expert Opinion on Medical Diagnostics*, vol. 2, no. 4, pp. 339–348, Apr. 2008, doi: 10.1517/17530059.2.4.339.

[26] C. Berger, M. Berger, J. Feng, and S. R. Riddell, "Genetic modification of T cells for immunotherapy," *Expert Opinion on Biological Therapy*, vol. 7, no. 8, pp. 1167–1182, Aug. 2007, doi: 10.1517/14712598.7.8.1167.

[27] A. Ribas, "Tumor Immunotherapy Directed at PD-1," *New England Journal of Medicine*, vol. 366, no. 26, pp. 2517–2519, Jun. 2012, doi: 10.1056/NEJMe1205943.

[28] M. Sadelain, I. Rivière, and S. Riddell, "Therapeutic T cell engineering," *Nature*, vol. 545, no. 7655, p. 423, May 2017, doi: 10.1038/nature22395.

[29] S. Lam and C. Bollard, "T-cell therapies for HIV," *Immunotherapy*, vol. 5, no. 4, pp. 407–414, Apr. 2013, doi: 10.2217/imt.13.23.

[30] K. Bacon, A. Lavoie, B. M. Rao, M. Daniele, and S. Menegatti, "Past, Present, and Future of Affinity-based Cell Separation Technologies," *Acta Biomaterialia*, vol. 112, pp. 29–51, Aug. 2020, doi: 10.1016/j.actbio.2020.05.004.

[31] D. D. Carlo, "Inertial microfluidics," *Lab Chip*, vol. 9, no. 21, pp. 3038–3046, Nov. 2009, doi: 10.1039/B912547G.

[32] J. Zhang *et al.*, "Fundamentals and applications of inertial microfluidics: a review," *Lab Chip*, vol. 16, no. 1, pp. 10–34, 2016, doi: 10.1039/C5LC01159K.

[33] S. Kalyan *et al.*, "Inertial Microfluidics Enabling Clinical Research," *Micromachines*, vol. 12, no. 3, Art. no. 3, Mar. 2021, doi: 10.3390/mi12030257.

[34] Y. Feng, L. Huang, P. Zhao, F. Liang, and W. Wang, "A Microfluidic Device Integrating Impedance Flow Cytometry and Electric Impedance Spectroscopy for High-Efficiency Single-Cell Electrical Property Measurement," *Anal. Chem.*, vol. 91, no. 23, pp. 15204–15212, Dec. 2019, doi: 10.1021/acs.analchem.9b04083.

[35] S. Kim *et al.*, "A Review of Advanced Impedance Biosensors with Microfluidic Chips for Single-Cell Analysis," *Biosensors (Basel)*, vol. 11, no. 11, p. 412, Oct. 2021, doi: 10.3390/bios11110412.

[36] W.-Y. Lin, Y. Wang, S. Wang, and H.-R. Tseng, "Integrated microfluidic reactors," *Nano Today*, vol. 4, no. 6, pp. 470–481, Dec. 2009, doi: 10.1016/j.nantod.2009.10.007.

[37] J. de Jong, R. G. H. Lammertink, and M. Wessling, "Membranes and microfluidics: a review," *Lab Chip*, vol. 6, no. 9, pp. 1125–1139, Aug. 2006, doi: 10.1039/B603275C.

[38] S.-E. Choi, H. Khoo, and S. C. Hur, "Recent Advances in Microscale Electroporation," *Chem. Rev.*, vol. 122, no. 13, pp. 11247–11286, Jul. 2022, doi: 10.1021/acs.chemrev.1c00677.

[39] M. B. Fox *et al.*, "Electroporation of cells in microfluidic devices: a review," *Anal Bioanal Chem*, vol. 385, no. 3, pp. 474–485, Jun. 2006, doi: 10.1007/s00216-006-0327-3.

[40] L. R. Volpatti and A. K. Yetisen, "Commercialization of microfluidic devices," *Trends in Biotechnology*, vol. 32, no. 7, pp. 347–350, Jul. 2014, doi: 10.1016/j.tibtech.2014.04.010.

[41] B. K. Gale *et al.*, "A Review of Current Methods in Microfluidic Device Fabrication and Future Commercialization Prospects," *Inventions*, vol. 3, no. 3, Art. no. 3, Sep. 2018, doi: 10.3390/inventions3030060.

[42] H. Amini, W. Lee, and D. D. Carlo, "Inertial microfluidic physics," *Lab Chip*, vol. 14, no. 15, pp. 2739–2761, 2014, doi: 10.1039/C4LC00128A.

[43] A. J. Chung, "A Minireview on Inertial Microfluidics Fundamentals: Inertial Particle Focusing and Secondary Flow," *BioChip J*, vol. 13, no. 1, pp. 53–63, Mar. 2019, doi: 10.1007/s13206-019-3110-1.

[44] S. C. Hur, N. K. Henderson-MacLennan, E. R. B. McCabe, and D. D. Carlo, "Deformability-based cell classification and enrichment using inertial microfluidics," *Lab Chip*, vol. 11, no. 5, pp. 912–920, Mar. 2011, doi: 10.1039/C0LC00595A.

[45] J. Choi, S. C. Hong, W. Kim, and J. H. Jung, "Highly Enriched, Controllable, Continuous Aerosol Sampling Using Inertial Microfluidics and Its Application to Real-Time Detection of Airborne Bacteria," *ACS Sens.*, vol. 2, no. 4, pp. 513–521, Apr. 2017, doi: 10.1021/acssensors.6b00753.

[46] S. C. Hong, J. S. Kang, J. E. Lee, S. S. Kim, and J. H. Jung, "Continuous aerosol size separator using inertial microfluidics and its application to airborne bacteria and viruses," *Lab Chip*, vol. 15, no. 8, pp. 1889–1897, Mar. 2015, doi: 10.1039/C5LC00079C.

[47] K. R. Ganz, L. Clime, J. M. Farber, N. Corneau, T. Veres, and B. R. Dixon, "Enhancing the Detection of Giardia duodenalis Cysts in Foods by Inertial Microfluidic Separation," *Applied and Environmental Microbiology*, vol. 81, no. 12, pp. 3925–3933, Jun. 2015, doi: 10.1128/AEM.03868-14.

[48] L. Clime *et al.*, "Microfluidic filtration and extraction of pathogens from food samples by hydrodynamic focusing and inertial lateral migration," *Biomed Microdevices*, vol. 17, no. 1, p. 17, Feb. 2015, doi: 10.1007/s10544-014-9905-x.

[49] G.-B. Lee, C.-J. Chang, C.-H. Wang, M.-Y. Lu, and Y.-Y. Luo, "Continuous medium exchange and optically induced electroporation of cells in an integrated microfluidic system," *Microsyst Nanoeng*, vol. 1, no. 1, Art. no. 1, Jun. 2015, doi: 10.1038/micronano.2015.7.

[50] A. J. Mach and D. D. Carlo, "Continuous scalable blood filtration device using inertial microfluidics," *Biotechnology and Bioengineering*, vol. 107, no. 2, pp. 302–311, 2010, doi: 10.1002/bit.22833.

[51] X. Wang, J. Zhou, and I. Papautsky, "Vortex-aided inertial microfluidic device for continuous particle separation with high size-selectivity, efficiency, and purity," *Biomicrofluidics*, vol. 7, no. 4, p. 044119, Jul. 2013, doi: 10.1063/1.4818906.

[52] S. S. Kuntaegowdanahalli, A. A. S. Bhagat, G. Kumar, and I. Papautsky, "Inertial microfluidics for continuous particle separation in spiral microchannels," *Lab Chip*, vol. 9, no. 20, pp. 2973–2980, Oct. 2009, doi: 10.1039/B908271A.

[53]   S. C. Hur, A. J. Mach, and D. Di Carlo, "High-throughput size-based rare cell enrichment using microscale vortices," *Biomicrofluidics*, vol. 5, no. 2, Jun. 2011, doi: 10.1063/1.3576780.

[54]   E. Sollier *et al.*, "Size-selective collection of circulating tumor cells using Vortex technology," *Lab on a Chip*, vol. 14, no. 1, pp. 63–77, 2014, doi: 10.1039/C3LC50689D.

[55]   H. W. Hou *et al.*, "Isolation and retrieval of circulating tumor cells using centrifugal forces," *Sci Rep*, vol. 3, no. 1, Art. no. 1, Feb. 2013, doi: 10.1038/srep01259.

[56]   E. Ozkumur *et al.*, "Inertial focusing for tumor antigen-dependent and -independent sorting of rare circulating tumor cells," *Sci Transl Med*, vol. 5, no. 179, p. 179ra47, Apr. 2013, doi: 10.1126/scitranslmed.3005616.

[57]   M. Zeinali *et al.*, "High-Throughput Label-Free Isolation of Heterogeneous Circulating Tumor Cells and CTC Clusters from Non-Small-Cell Lung Cancer Patients," *Cancers (Basel)*, vol. 12, no. 1, p. E127, Jan. 2020, doi: 10.3390/cancers12010127.

[58]   C. Petchakup *et al.*, "Label-free leukocyte sorting and impedance-based profiling for diabetes testing," *Biosens Bioelectron*, vol. 118, pp. 195–203, Oct. 2018, doi: 10.1016/j.bios.2018.07.052.

[59]   H. M. Tay, R. Dalan, K. H. H. Li, B. O. Boehm, and H. W. Hou, "A Novel Microdevice for Rapid Neutrophil Purification and Phenotyping in Type 2 Diabetes Mellitus," *Small*, vol. 14, no. 6, p. 1702832, 2018, doi: 10.1002/smll.201702832.

[60]   C. Petchakup, H. M. Tay, K. H. H. Li, and H. W. Hou, "Integrated inertial-impedance cytometry for rapid label-free leukocyte isolation and profiling of neutrophil extracellular traps (NETs)," *Lab Chip*, vol. 19, no. 10, pp. 1736–1746, May 2019, doi: 10.1039/C9LC00250B.

[61]   H. W. Hou *et al.*, "Rapid and label-free microfluidic neutrophil purification and phenotyping in diabetes mellitus," *Sci Rep*, vol. 6, no. 1, Art. no. 1, Jul. 2016, doi: 10.1038/srep29410.

[62]   B. Jundi *et al.*, "Leukocyte function assessed via serial microlitre sampling of peripheral blood from sepsis patients correlates with disease severity," *Nat Biomed Eng*, vol. 3, no. 12, Art. no. 12, Dec. 2019, doi: 10.1038/s41551-019-0473-5.

[63]   J. Son, K. Murphy, R. Samuel, B. K. Gale, D. T. Carrell, and J. M. Hotaling, "Non-motile sperm cell separation using a spiral channel," *Anal Methods*, vol. 7, no. 19, pp. 8041–8047, Sep. 2015, doi: 10.1039/C5AY02205C.

[64]   J. Son, R. Samuel, B. K. Gale, D. T. Carrell, and J. M. Hotaling, "Separation of sperm cells from samples containing high concentrations of white blood cells using a spiral channel," *Biomicrofluidics*, vol. 11, no. 5, Sep. 2017, doi: 10.1063/1.4994548.

[65]   R. Samuel *et al.*, "Microfluidic System for Rapid Isolation of Sperm From Microdissection TESE Specimens," *Urology*, vol. 140, pp. 70–76, Jun. 2020, doi: 10.1016/j.urology.2019.12.053.

[66]   A. Jafek *et al.*, "Optimization of Dean flow microfluidic chip for sperm preparation for intrauterine insemination," *Microfluid Nanofluidics*, vol. 24, no. 8, p. 60, Jul. 2020, doi: 10.1007/s10404-020-02366-y.

[67]   Y. Zhou, Z. Ma, M. Tayebi, and Y. Ai, "Submicron Particle Focusing and Exosome Sorting by Wavy Microchannel Structures within Viscoelastic Fluids," *Anal Chem*, vol. 91, no. 7, pp. 4577–4584, Apr. 2019, doi: 10.1021/acs.analchem.8b05749.

[68]   C. Liu *et al.*, "Field-Free Isolation of Exosomes from Extracellular Vesicles by Microfluidic Viscoelastic Flows," *ACS Nano*, vol. 11, no. 7, pp. 6968–6976, Jul. 2017, doi: 10.1021/acsnano.7b02277.

[69]   H. M. Tay *et al.*, "Rapid purification of sub-micrometer particles for enhanced drug release and microvesicles isolation," *NPG Asia Mater*, vol. 9, no. 9, Art. no. 9, Sep. 2017, doi: 10.1038/am.2017.175.

[70]   M. E. Warkiani, A. K. P. Tay, B. L. Khoo, X. Xiaofeng, J. Han, and C. T. Lim, "Malaria detection using inertial microfluidics," *Lab Chip*, vol. 15, no. 4, pp. 1101–1109, Feb. 2015, doi: 10.1039/C4LC01058B.

[71] M. A. Faridi, H. Ramachandraiah, I. Banerjee, S. Ardabili, S. Zelenin, and A. Russom, "Elasto-inertial microfluidics for bacteria separation from whole blood for sepsis diagnostics," *J Nanobiotechnol*, vol. 15, no. 1, p. 3, Jan. 2017, doi: 10.1186/s12951-016-0235-4.

[72] N. Xiang and Z. Ni, "High-throughput blood cell focusing and plasma isolation using spiral inertial microfluidic devices," *Biomed Microdevices*, vol. 17, no. 6, p. 110, Dec. 2015, doi: 10.1007/s10544-015-0018-y.

[73] M. G. Lee *et al.*, "Inertial blood plasma separation in a contraction–expansion array microchannel," *Appl. Phys. Lett.*, vol. 98, no. 25, p. 253702, Jun. 2011, doi: 10.1063/1.3601745.

[74] J. Zhang, S. Yan, D. Yuan, G. Alici, N.-T. Nguyen, and W. Li, "High Throughput Cell-Free Extraction of Plasma by an Integrated Microfluidic Device Combining Inertial Focusing and Membrane," *Journal of Heat Transfer*, vol. 139, no. 5, Feb. 2017, doi: 10.1115/1.4035588.

[75] M. Dhar, J. N. Lam, T. Walser, S. M. Dubinett, M. B. Rettig, and D. Di Carlo, "Functional profiling of circulating tumor cells with an integrated vortex capture and single-cell protease activity assay," *Proc Natl Acad Sci U S A*, vol. 115, no. 40, pp. 9986–9991, Oct. 2018, doi: 10.1073/pnas.1803884115.

[76] H. Yun and S. C. Hur, "Sequential multi-molecule delivery using vortex-assisted electroporation," *Lab Chip*, vol. 13, no. 14, pp. 2764–2772, Jun. 2013, doi: 10.1039/C3LC50196E.

[77] C. Raillon *et al.*, "Toward Microfluidic Label-Free Isolation and Enumeration of Circulating Tumor Cells from Blood Samples," *Cytometry Part A*, vol. 95, no. 10, pp. 1085–1095, 2019, doi: 10.1002/cyto.a.23868.

[78] D. A. L. Vickers, M. Ouyang, C. H. Choi, and S. C. Hur, "Direct Drug Cocktail Analyses Using Microscale Vortex-Assisted Electroporation," *Anal. Chem.*, vol. 86, no. 20, pp. 10099–10105, Oct. 2014, doi: 10.1021/ac501479g.

[79] H. W. Sung *et al.*, "Sensitizing drug-resistant cancer cells from blood using microfluidic electroporator," *PLOS ONE*, vol. 17, no. 3, p. e0264907, Mar. 2022, doi: 10.1371/journal.pone.0264907.

[80] M. Ouyang, W. Hill, J. H. Lee, and S. C. Hur, "Microscale Symmetrical Electroporator Array as a Versatile Molecular Delivery System," *Scientific Reports*, vol. 7, p. 44757, Mar. 2017, doi: 10.1038/srep44757.

[81] H. Haddadi and D. D. Carlo, "Inertial flow of a dilute suspension over cavities in a microchannel," *Journal of Fluid Mechanics*, vol. 811, pp. 436–467, Jan. 2017, doi: 10.1017/jfm.2016.709.

[82] S. Bale, A. Khurana, A. S. S. Reddy, M. Singh, and C. Godugu, "Overview on Therapeutic Applications of Microparticulate Drug Delivery Systems," *CRT*, vol. 33, no. 4, 2016, doi: 10.1615/CritRevTherDrugCarrierSyst.2016015798.

[83] N. Rasenack and B. W. Müller, "Micron-size drug particles: common and novel micronization techniques," *Pharm Dev Technol*, vol. 9, no. 1, pp. 1–13, 2004, doi: 10.1081/pdt-120027417.

[84] J. Cheng, Q. Liu, A. J. Shuhendler, A. M. Rauth, and X. Y. Wu, "Optimizing the design and in vitro evaluation of bioreactive glucose oxidase-microspheres for enhanced cytotoxicity against multidrug resistant breast cancer cells," *Colloids and Surfaces B: Biointerfaces*, vol. 130, pp. 164–172, Jun. 2015, doi: 10.1016/j.colsurfb.2015.04.002.

[85] T. Morita, Y. Horikiri, T. Suzuki, and H. Yoshino, "Preparation of gelatin microparticles by co-lyophilization with poly(ethylene glycol): characterization and application to entrapment into biodegradable microspheres," *International Journal of Pharmaceutics*, vol. 219, no. 1, pp. 127–137, May 2001, doi: 10.1016/S0378-5173(01)00642-1.

[86] D. E. Lewis and S. E. Blutt, "2 - Organization of the Immune System," in *Clinical Immunology (Fifth Edition)*, R. R. Rich, T. A. Fleisher, W. T. Shearer, H. W. Schroeder, A. J. Frew, and C. M. Weyand, Eds. London: Elsevier, 2019, pp. 19-38.e1. doi: 10.1016/B978-0-7020-6896-6.00002-8.

[87]   J. M. Bryant, M. L. Meyer-Ficca, V. M. Dang, S. L. Berger, and R. G. Meyer, "Separation of Spermatogenic Cell Types Using STA-PUT Velocity Sedimentation," *J Vis Exp*, no. 80, p. 50648, Oct. 2013, doi: 10.3791/50648.

[88]   S. Zullo and L. Caenazzo, "Gene editing and gender-specific medicine: a challenge for dementia research," *Palgrave Commun*, vol. 6, no. 1, Art. no. 1, Mar. 2020, doi: 10.1057/s41599-020-0416-5.

[89]   C. S. De Paiva, S. C. Pflugfelder, and D.-Q. Li, "Cell Size Correlates with Phenotype and Proliferative Capacity in Human Corneal Epithelial Cells," *Stem Cells*, vol. 24, no. 2, pp. 368–375, Feb. 2006, doi: 10.1634/stemcells.2005-0148.

[90]   N. Zakaria, N. Cools, Z. Berneman, and M.-J. Tassignon, "Electroporating Human Corneal Epithelial Cells With Interleukin 10 and Fas Ligand pDNA," *The Asia-Pacific Journal of Ophthalmology*, vol. 3, no. 1, pp. 56–63, Feb. 2014, doi: 10.1097/APO.0000000000000034.

[91]   F. (申峰) Shen, S. (薛森) Xue, M. (徐旻) Xu, Y. (逄燕) Pang, and Z. M. (刘赵淼) Liu, "Experimental study of single-particle trapping mechanisms into microcavities using microfluidics," *Physics of Fluids*, vol. 31, no. 4, p. 042002, Apr. 2019, doi: 10.1063/1.5081918.

[92]   R. Khojah, R. Stoutamore, and D. D. Carlo, "Size-tunable microvortex capture of rare cells," *Lab Chip*, vol. 17, no. 15, pp. 2542–2549, Jul. 2017, doi: 10.1039/C7LC00355B.

[93]   H.-Y. Tseng, C.-J. Chen, Z.-L. Wu, Y.-M. Ye, and G.-Z. Huang, "The non-contact-based determination of the membrane permeability to water and dimethyl sulfoxide of cells virtually trapped in a self-induced micro-vortex," *Lab Chip*, vol. 22, no. 2, pp. 354–366, Jan. 2022, doi: 10.1039/D1LC00846C.

[94]   J. Shi *et al.*, "A Review on Electroporation-Based Intracellular Delivery," *Molecules*, vol. 23, no. 11, Art. no. 11, Nov. 2018, doi: 10.3390/molecules23113044.

[95]   M. Ray, Y.-W. Lee, F. Scaletti, R. Yu, and V. M. Rotello, "Intracellular delivery of proteins by nanocarriers," *Nanomedicine (Lond)*, vol. 12, no. 8, pp. 941–952, Apr. 2017, doi: 10.2217/nnm-2016-0393.

[96]   A. Dinca, W.-M. Chien, and M. T. Chin, "Intracellular Delivery of Proteins with Cell-Penetrating Peptides for Therapeutic Uses in Human Disease," *International Journal of Molecular Sciences*, vol. 17, no. 2, Art. no. 2, Feb. 2016, doi: 10.3390/ijms17020263.

[97]   M. Wang, K. Alberti, S. Sun, C. L. Arellano, and Q. Xu, "Combinatorially Designed Lipid-like Nanoparticles for Intracellular Delivery of Cytotoxic Protein for Cancer Therapy," *Angewandte Chemie International Edition*, vol. 53, no. 11, pp. 2893–2898, 2014, doi: 10.1002/anie.201311245.

[98]   J. B. Miller and D. J. Siegwart, "Design of synthetic materials for intracellular delivery of RNAs: From siRNA-mediated gene silencing to CRISPR/Cas gene editing," *Nano Res.*, vol. 11, no. 10, pp. 5310–5337, Oct. 2018, doi: 10.1007/s12274-018-2099-4.

[99]   Y. Li *et al.*, "Combinatorial library of chalcogen-containing lipidoids for intracellular delivery of genome-editing proteins," *Biomaterials*, vol. 178, pp. 652–662, Sep. 2018, doi: 10.1016/j.biomaterials.2018.03.011.

[100]   Q. Zheng, W. Li, L. Mao, and M. Wang, "Nanoscale metal–organic frameworks for the intracellular delivery of CRISPR/Cas9 genome editing machinery," *Biomaterials Science*, vol. 9, no. 21, pp. 7024–7033, 2021, doi: 10.1039/D1BM00790D.

[101]   D. E. Chafai, A. Mehle, A. Tilmatine, B. Maouche, and D. Miklavčič, "Assessment of the electrochemical effects of pulsed electric fields in a biological cell suspension," *Bioelectrochemistry*, vol. 106, pp. 249–257, Dec. 2015, doi: 10.1016/j.bioelechem.2015.08.002.

[102]   G. Pataro, M. Falcone, G. Donsì, and G. Ferrari, "Metal release from stainless steel electrodes of a PEF treatment chamber: Effects of electrical parameters and food composition," *Innovative Food Science & Emerging Technologies*, vol. 21, pp. 58–65, Jan. 2014, doi: 10.1016/j.ifset.2013.10.005.

[103] K. H. Schoenbach, S. J. Beebe, and E. S. Buescher, "Intracellular effect of ultrashort electrical pulses," *Bioelectromagnetics*, vol. 22, no. 6, pp. 440–448, 2001, doi: 10.1002/bem.71.

[104] C. A. Lissandrello *et al.*, "High-throughput continuous-flow microfluidic electroporation of mRNA into primary human T cells for applications in cellular therapy manufacturing," *Sci Rep*, vol. 10, no. 1, Art. no. 1, Oct. 2020, doi: 10.1038/s41598-020-73755-0.

[105] W. Kang *et al.*, "Microfluidic device for stem cell differentiation and localized electroporation of postmitotic neurons," *Lab on a Chip*, vol. 14, no. 23, pp. 4486–4495, 2014, doi: 10.1039/C4LC00721B.

[106] A. Valero, J. N. Post, J. W. van Nieuwkasteele, P. M. ter Braak, W. Kruijer, and A. van den Berg, "Gene transfer and protein dynamics in stem cells using single cell electroporation in a microfluidic device," *Lab on a Chip*, vol. 8, no. 1, pp. 62–67, 2008, doi: 10.1039/B713420G.

[107] J. Gehl, "Electroporation: theory and methods, perspectives for drug delivery, gene therapy and research," *Acta Physiologica Scandinavica*, vol. 177, no. 4, pp. 437–447, Apr. 2003, doi: 10.1046/j.1365-201X.2003.01093.x.

[108] D. R. Reyes *et al.*, "Accelerating innovation and commercialization through standardization of microfluidic-based medical devices," *Lab Chip*, vol. 21, no. 1, pp. 9–21, Jan. 2021, doi: 10.1039/D0LC00963F.

[109] G. N. McKay, T. L. Bobrow, S. Kalyan, S. C. Hur, and N. J. Durr, "Optimizing white blood cell contrast in graded-field capillaroscopy using capillary tissue phantoms," in *Imaging, Manipulation, and Analysis of Biomolecules, Cells, and Tissues XVIII*, Feb. 2020, vol. 11243, pp. 24–30. doi: 10.1117/12.2546995.

[110] G. N. McKay *et al.*, "A model for generating paired complete blood count and oblique back-illumination capillaroscopy data in tissue-realistic microfluidic chambers," in *Imaging, Manipulation, and Analysis of Biomolecules, Cells, and Tissues XX*, Mar. 2022, vol. 11964, pp. 97–103. doi: 10.1117/12.2609715.

[111] T. V. Johnson, N. D. Bull, and K. R. Martin, "Stem cell therapy for glaucoma: possibilities and practicalities," *Expert Rev Ophthalmol*, vol. 6, no. 2, pp. 165–174, Apr. 2011, doi: 10.1586/eop.11.3.

[112] M. Yamada, M. Nakashima, and M. Seki, "Pinched Flow Fractionation: Continuous Size Separation of Particles Utilizing a Laminar Flow Profile in a Pinched Microchannel," *Anal. Chem.*, vol. 76, no. 18, pp. 5465–5471, Sep. 2004, doi: 10.1021/ac049863r.

[113] A. A. S. Bhagat, H. Bow, H. W. Hou, S. J. Tan, J. Han, and C. T. Lim, "Microfluidics for cell separation," *Med Biol Eng Comput*, vol. 48, no. 10, pp. 999–1014, Oct. 2010, doi: 10.1007/s11517-010-0611-4.

[114] J. Siepmann, N. Faisant, J. Akiki, J. Richard, and J. P. Benoit, "Effect of the size of biodegradable microparticles on drug release: experiment and theory," *Journal of Controlled Release*, vol. 96, no. 1, pp. 123–134, Apr. 2004, doi: 10.1016/j.jconrel.2004.01.011.

[115] C. Tianshou, "Size separation for hard microparticles," *Materials Science and Engineering: A*, vol. 105–106, pp. 571–576, Dec. 1988, doi: 10.1016/0025-5416(88)90745-8.

[116] D. Klose, F. Siepmann, K. Elkharraz, and J. Siepmann, "PLGA-based drug delivery systems: Importance of the type of drug and device geometry," *International Journal of Pharmaceutics*, vol. 354, no. 1, pp. 95–103, Apr. 2008, doi: 10.1016/j.ijpharm.2007.10.030.

[117] R. Bhujel, R. Maharjan, N. A. Kim, and S. H. Jeong, "Practical quality attributes of polymeric microparticles with current understanding and future perspectives," *Journal of Drug Delivery Science and Technology*, vol. 64, p. 102608, Aug. 2021, doi: 10.1016/j.jddst.2021.102608.

[118] Y. Yoon *et al.*, "Clogging-free microfluidics for continuous size-based separation of microparticles," *Sci Rep*, vol. 6, no. 1, Art. no. 1, May 2016, doi: 10.1038/srep26531.

[119] A. Farahinia, W. J. Zhang, and I. Badea, "Novel microfluidic approaches to circulating tumor cell separation and sorting of blood cells: A review," *Journal of Science: Advanced Materials and Devices*, vol. 6, no. 3, pp. 303–320, Sep. 2021, doi: 10.1016/j.jsamd.2021.03.005.

[120] Z. Wu, B. Willing, J. Bjerketorp, J. K. Jansson, and K. Hjort, "Soft inertial microfluidics for high throughput separation of bacteria from human blood cells," *Lab on a Chip*, vol. 9, no. 9, pp. 1193–1199, 2009, doi: 10.1039/B817611F.

[121] H. Okano *et al.*, "Enrichment of circulating tumor cells in tumor-bearing mouse blood by a deterministic lateral displacement microfluidic device," *Biomed Microdevices*, vol. 17, no. 3, p. 59, May 2015, doi: 10.1007/s10544-015-9964-7.

[122] S. H. Holm, J. P. Beech, M. P. Barrett, and J. O. Tegenfeldt, "Separation of parasites from human blood using deterministic lateral displacement," *Lab Chip*, vol. 11, no. 7, pp. 1326–1332, Apr. 2011, doi: 10.1039/C0LC00560F.

[123] C. Henning, N. Aygül, P. Dinnétz, K. Wallgren, and V. Özenci, "Detailed Analysis of the Characteristics of Sample Volume in Blood Culture Bottles," *Journal of Clinical Microbiology*, vol. 57, no. 8, pp. e00268-19, Jul. 2019, doi: 10.1128/JCM.00268-19.

[124] J. M. Martel and M. Toner, "Inertial Focusing in Microfluidics," *Annu Rev Biomed Eng*, vol. 16, pp. 371–396, Jul. 2014, doi: 10.1146/annurev-bioeng-121813-120704.

[125] X. Wang and I. Papautsky, "Size-based microfluidic multimodal microparticle sorter," *Lab on a Chip*, vol. 15, no. 5, pp. 1350–1359, 2015, doi: 10.1039/C4LC00803K.

[126] H. Fallahi, J. Zhang, J. Nicholls, H.-P. Phan, and N.-T. Nguyen, "Stretchable Inertial Microfluidic Device for Tunable Particle Separation," *Anal. Chem.*, vol. 92, no. 18, pp. 12473–12480, Sep. 2020, doi: 10.1021/acs.analchem.0c02294.

[127] D. Stoecklein and D. Di Carlo, "Nonlinear Microfluidics," *Anal. Chem.*, vol. 91, no. 1, pp. 296–314, Jan. 2019, doi: 10.1021/acs.analchem.8b05042.

[128] W. Tong, X. Song, and C. Gao, "Layer-by-layer assembly of microcapsules and their biomedical applications," *Chemical Society Reviews*, vol. 41, no. 18, pp. 6103–6124, 2012, doi: 10.1039/C2CS35088B.

[129] Z. Gong, S. Penmetsa, Z. Zheng, Y. Lvov, and L. Que, "Encapsulation of microparticles and biomolecules based on layer-by-layer nanoassembly techniques with microfluidic droplet devices," in *TRANSDUCERS 2009 - 2009 International Solid-State Sensors, Actuators and Microsystems Conference*, Jun. 2009, pp. 1043–1046. doi: 10.1109/SENSOR.2009.5285967.

[130] N. N. Parayath and M. T. Stephan, "In Situ Programming of CAR T Cells," *Annual Review of Biomedical Engineering*, vol. 23, no. 1, pp. 385–405, 2021, doi: 10.1146/annurev-bioeng-070620-033348.

[131] A. I. Segaliny *et al.*, "Functional TCR T cell screening using single-cell droplet microfluidics," *Lab on a Chip*, vol. 18, no. 24, pp. 3733–3749, 2018, doi: 10.1039/C8LC00818C.

[132] B. Joo, J. Hur, G.-B. Kim, S. G. Yun, and A. J. Chung, "Highly Efficient Transfection of Human Primary T Lymphocytes Using Droplet-Enabled Mechanoporation," *ACS Nano*, vol. 15, no. 8, pp. 12888–12898, Aug. 2021, doi: 10.1021/acsnano.0c10473.

[133] C. Celebi, T. Guillaudeux, P. Auvray, V. Vallet-Erdtmann, and B. Jégou, "The Making of 'Transgenic Spermatozoa'1," *Biology of Reproduction*, vol. 68, no. 5, pp. 1477–1483, May 2003, doi: 10.1095/biolreprod.102.009340.

[134] M. Dhar *et al.*, "High efficiency vortex trapping of circulating tumor cells," *Biomicrofluidics*, vol. 9, no. 6, p. 064116, Nov. 2015, doi: 10.1063/1.4937895.

[135] U. Manna and S. Patil, "Encapsulation of Uncharged Water-Insoluble Organic Substance in Polymeric Membrane Capsules via Layer-by-Layer Approach," *J. Phys. Chem. B*, vol. 112, no. 42, pp. 13258–13262, Oct. 2008, doi: 10.1021/jp806140s.

[136] A. M. Leen, C. M. Rooney, and A. E. Foster, "Improving T Cell Therapy for Cancer," *Annual Review of Immunology*, vol. 25, no. 1, pp. 243–265, 2007, doi: 10.1146/annurev.immunol.25.022106.141527.

[137] C. H. June, "Adoptive T cell therapy for cancer in the clinic," *J Clin Invest*, vol. 117, no. 6, pp. 1466–1476, Jun. 2007, doi: 10.1172/JCI32446.

[138] L. Zhao and Y. J. Cao, "Engineered T Cell Therapy for Cancer in the Clinic," *Frontiers in Immunology*, vol. 10, 2019, Accessed: Aug. 29, 2022. [Online]. Available: https://www.frontiersin.org/articles/10.3389/fimmu.2019.02250

[139] S. Patel, R. B. Jones, D. F. Nixon, and C. M. Bollard, "T-cell therapies for HIV: Preclinical successes and current clinical strategies," *Cytotherapy*, vol. 18, no. 8, pp. 931–942, Aug. 2016, doi: 10.1016/j.jcyt.2016.04.007.

[140] T. G. Schuster, B. Cho, L. M. Keller, S. Takayama, and G. D. Smith, "Isolation of motile spermatozoa from semen samples using microfluidics," *Reprod Biomed Online*, vol. 7, no. 1, pp. 75–81, Aug. 2003, doi: 10.1016/s1472-6483(10)61732-4.

[141] F. (申峰) Shen, Z. (李宗鹤) Li, M. (艾明珠) Ai, H. (高宏凯) Gao, and Z. (刘赵淼) Liu, "Round cavity-based vortex sorting of particles with enhanced holding capacity," *Physics of Fluids*, vol. 33, no. 8, p. 082002, Aug. 2021, doi: 10.1063/5.0061481.

[142] F. Shen, M. Xu, Z. Wang, and Z. Liu, "Single-particle trapping, orbiting, and rotating in a microcavity using microfluidics," *Appl. Phys. Express*, vol. 10, no. 9, p. 097301, Sep. 2017, doi: 10.7567/APEX.10.097301.

[143] M. Jiang, S. Qian, and Z. Liu, "Fully resolved simulation of single-particle dynamics in a microcavity," *Microfluid Nanofluid*, vol. 22, no. 12, p. 144, Nov. 2018, doi: 10.1007/s10404-018-2166-x.

[144] A. J. Mach, J. H. Kim, A. Arshi, S. C. Hur, and D. D. Carlo, "Automated cellular sample preparation using a Centrifuge-on-a-Chip," *Lab Chip*, vol. 11, no. 17, pp. 2827–2834, Aug. 2011, doi: 10.1039/C1LC20330D.

[145] M. Chebbo *et al.*, "Platelets Purification Is a Crucial Step for Transcriptomic Analysis," *Int J Mol Sci*, vol. 23, no. 6, p. 3100, Mar. 2022, doi: 10.3390/ijms23063100.

[146] A. Frick *et al.*, "Immune cell-based screening assay for response to anticancer agents: applications in pharmacogenomics," *PGPM*, vol. 8, pp. 81–98, Feb. 2015, doi: 10.2147/PGPM.S73312.

[147] Y. Liao, D. He, and F. Wen, "Analyzing the characteristics of immune cell infiltration in lung adenocarcinoma via bioinformatics to predict the effect of immunotherapy," *Immunogenetics*, vol. 73, no. 5, pp. 369–380, Oct. 2021, doi: 10.1007/s00251-021-01223-8.

[148] S. R. Bailey and M. V. Maus, "Gene editing for immune cell therapies," *Nat Biotechnol*, vol. 37, no. 12, Art. no. 12, Dec. 2019, doi: 10.1038/s41587-019-0137-8.

[149] M. C. Aldhous, G. M. Raab, J. Y. Mok, K. V. Doherty, A. G. Bird, and K. S. Froebel, "CD4 and CD8 lymphocytes in diagnosis and disease progression of pediatric HIV infection," *Pediatr AIDS HIV Infect*, vol. 7, no. 1, pp. 20–30, Feb. 1996.

[150] D. Morshedi Rad, M. Alsadat Rad, S. Razavi Bazaz, N. Kashaninejad, D. Jin, and M. Ebrahimi Warkiani, "A Comprehensive Review on Intracellular Delivery," *Advanced Materials*, vol. 33, no. 13, p. 2005363, 2021, doi: 10.1002/adma.202005363.

[151] L. Wang, L.-L. Li, H. L. Ma, and H. Wang, "Recent advances in biocompatible supramolecular assemblies for biomolecular detection and delivery," *Chinese Chemical Letters*, vol. 24, no. 5, pp. 351–358, May 2013, doi: 10.1016/j.cclet.2013.03.018.

[152] F. Mo, K. Jiang, D. Zhao, Y. Wang, J. Song, and W. Tan, "DNA hydrogel-based gene editing and drug delivery systems," *Advanced Drug Delivery Reviews*, vol. 168, pp. 79–98, Jan. 2021, doi: 10.1016/j.addr.2020.07.018.

[153] F. Knipping *et al.*, "Genome-wide Specificity of Highly Efficient TALENs and CRISPR/Cas9 for T Cell Receptor Modification," *Molecular Therapy - Methods & Clinical Development*, vol. 4, pp. 213–224, Mar. 2017, doi: 10.1016/j.omtm.2017.01.005.

[154] D. S. Anson, "The use of retroviral vectors for gene therapy-what are the risks? A review of retroviral pathogenesis and its relevance to retroviral vector-mediated gene delivery," *Genetic Vaccines and Therapy*, vol. 2, p. 9, Aug. 2004, doi: 10.1186/1479-0556-2-9.

[155] J. T. Bulcha, Y. Wang, H. Ma, P. W. L. Tai, and G. Gao, "Viral vector platforms within the gene therapy landscape," *Sig Transduct Target Ther*, vol. 6, no. 1, Art. no. 1, Feb. 2021, doi: 10.1038/s41392-021-00487-6.

[156] M. J. Hope, B. Mui, S. Ansell, and Q. F. Ahkong, "Cationic lipids, phosphatidylethanolamine and the intracellular delivery of polymeric, nucleic acid-based drugs (Review)," *Molecular Membrane Biology*, vol. 15, no. 1, pp. 1–14, Jan. 1998, doi: 10.3109/09687689809027512.

[157] R. Koynova, "Lipid Phases Eye View to Lipofection. Cationic Phosphatidylcholine Derivatives as Efficient DNA Carriers for Gene Delivery," *Lipid�Insights*, vol. 2, p. LPI.S864, Jan. 2008, doi: 10.4137/LPI.S864.

[158] B. E. Henslee, A. Morss, X. Hu, G. P. Lafyatis, and L. J. Lee, "Electroporation Dependence on Cell Size: Optical Tweezers Study," *Anal. Chem.*, vol. 83, no. 11, pp. 3998–4003, Jun. 2011, doi: 10.1021/ac1019649.

[159] Z. Wu, H. Yang, and P. Colosi, "Effect of Genome Size on AAV Vector Packaging," *Mol Ther*, vol. 18, no. 1, pp. 80–86, Jan. 2010, doi: 10.1038/mt.2009.255.

[160] S. Basiouni, H. Fuhrmann, and J. Schumann, "High-efficiency transfection of suspension cell lines," *BioTechniques*, vol. 53, no. 2, pp. 1–4, Aug. 2012, doi: 10.2144/000113914.

[161] T. Montier *et al.*, "KLN-5: a safe monocationic lipophosphoramide to transfect efficiently haematopoietic cell lines and human CD34+ cells," *Biochimica et Biophysica Acta (BBA) - Biomembranes*, vol. 1665, no. 1, pp. 118–133, Oct. 2004, doi: 10.1016/j.bbamem.2004.07.009.

[162] M. Wang, O. Orwar, J. Olofsson, and S. G. Weber, "Single-cell electroporation," *Anal Bioanal Chem*, vol. 397, no. 8, pp. 3235–3248, Aug. 2010, doi: 10.1007/s00216-010-3744-2.

[163] J. L. Young and D. A. Dean, "Electroporation-Mediated Gene Delivery," *Adv Genet*, vol. 89, pp. 49–88, 2015, doi: 10.1016/bs.adgen.2014.10.003.

[164] Y. Qu, Y. Zhang, Q. Yu, and H. Chen, "Surface-Mediated Intracellular Delivery by Physical Membrane Disruption," *ACS Appl. Mater. Interfaces*, vol. 12, no. 28, pp. 31054–31078, Jul. 2020, doi: 10.1021/acsami.0c06978.

[165] T. Batista Napotnik and D. Miklavčič, "In vitro electroporation detection methods – An overview," *Bioelectrochemistry*, vol. 120, pp. 166–182, Apr. 2018, doi: 10.1016/j.bioelechem.2017.12.005.

[166] H. Potter and R. Heller, "Transfection by Electroporation," *Curr Protoc Mol Biol*, vol. CHAPTER, p. Unit-9.3, May 2003, doi: 10.1002/0471142727.mb0903s62.

[167] A. Nikyar and A. Bolhassani, "Electroporation: An Effective Method For In Vivo Gene Delivery," *Drug Delivery Letters*, vol. 12, no. 1, pp. 35–45, Mar. 2022, doi: 10.2174/2210303112666220127113328.

[168] S. Remy *et al.*, "Generation of gene-edited rats by delivery of CRISPR/Cas9 protein and donor DNA into intact zygotes using electroporation," *Sci Rep*, vol. 7, no. 1, Art. no. 1, Nov. 2017, doi: 10.1038/s41598-017-16328-y.

[169] A. K. Banga and M. R. Prausnitz, "Assessing the potential of skin electroporation for the delivery of protein- and gene-based drugs," *Trends in Biotechnology*, vol. 16, no. 10, pp. 408–412, Oct. 1998, doi: 10.1016/S0167-7799(98)01238-4.

[170] Y. Cao *et al.*, "Nontoxic nanopore electroporation for effective intracellular delivery of biological macromolecules," *Proceedings of the National Academy of Sciences*, vol. 116, no. 16, pp. 7899–7904, Apr. 2019, doi: 10.1073/pnas.1818553116.

[171] K. Kim, J. A. Kim, S.-G. Lee, and W. G. Lee, "Seeing the electroporative uptake of cell-membrane impermeable fluorescent molecules and nanoparticles," *Nanoscale*, vol. 4, no. 16, pp. 5051–5058, Jul. 2012, doi: 10.1039/C2NR30578J.

[172] C. Lombry, N. Dujardin, and V. Préat, "Transdermal Delivery of Macromolecules Using Skin Electroporation," *Pharm Res*, vol. 17, no. 1, pp. 32–37, Jan. 2000, doi: 10.1023/A:1007510323344.

[173] T. Blagus *et al.*, "In vivo real-time monitoring system of electroporation mediated control of transdermal and topical drug delivery," *Journal of Controlled Release*, vol. 172, no. 3, pp. 862–871, Dec. 2013, doi: 10.1016/j.jconrel.2013.09.030.

[174] D. Miklavčič *et al.*, "Electrochemotherapy: technological advancements for efficient electroporation-based treatment of internal tumors," *Med Biol Eng Comput*, vol. 50, no. 12, pp. 1213–1225, Dec. 2012, doi: 10.1007/s11517-012-0991-8.

[175] G. Sersa, D. Miklavcic, M. Cemazar, Z. Rudolf, G. Pucihar, and M. Snoj, "Electrochemotherapy in treatment of tumours," *European Journal of Surgical Oncology (EJSO)*, vol. 34, no. 2, pp. 232–240, Feb. 2008, doi: 10.1016/j.ejso.2007.05.016.

[176] K. Kim and W. Gu Lee, "Electroporation for nanomedicine: a review," *Journal of Materials Chemistry B*, vol. 5, no. 15, pp. 2726–2738, 2017, doi: 10.1039/C7TB00038C.

[177] S. Egloff, A. Runser, A. Klymchenko, and A. Reisch, "Size-Dependent Electroporation of Dye-Loaded Polymer Nanoparticles for Efficient and Safe Intracellular Delivery," *Small Methods*, vol. 5, no. 2, p. 2000947, 2021, doi: 10.1002/smtd.202000947.

[178] J. Lin *et al.*, "Rapid delivery of silver nanoparticles into living cells by electroporation for surface-enhanced Raman spectroscopy," *Biosensors and Bioelectronics*, vol. 25, no. 2, pp. 388–394, Oct. 2009, doi: 10.1016/j.bios.2009.07.027.

[179] S. Movahed and D. Li, "Microfluidics cell electroporation," *Microfluid Nanofluid*, vol. 10, no. 4, pp. 703–734, Apr. 2011, doi: 10.1007/s10404-010-0716-y.

[180] T. Geng and C. Lu, "Microfluidic electroporation for cellular analysis and delivery," *Lab on a Chip*, vol. 13, no. 19, pp. 3803–3821, 2013, doi: 10.1039/C3LC50566A.

[181] Q. Zhang, S. Feng, L. Lin, S. Mao, and J.-M. Lin, "Emerging open microfluidics for cell manipulation," *Chemical Society Reviews*, vol. 50, no. 9, pp. 5333–5348, 2021, doi: 10.1039/D0CS01516D.

[182] H. Yun, K. Kim, and W. G. Lee, "Cell manipulation in microfluidics," *Biofabrication*, vol. 5, no. 2, p. 022001, Feb. 2013, doi: 10.1088/1758-5082/5/2/022001.

[183] B. Xiong, K. Ren, Y. Shu, Y. Chen, B. Shen, and H. Wu, "Recent Developments in Microfluidics for Cell Studies," *Advanced Materials*, vol. 26, no. 31, pp. 5525–5532, 2014, doi: 10.1002/adma.201305348.

[184] J. M. Martel and M. Toner, "Inertial Focusing in Microfluidics," *Annu Rev Biomed Eng*, vol. 16, pp. 371–396, Jul. 2014, doi: 10.1146/annurev-bioeng-121813-120704.

[185] A.-S. Vander Plaetsen, J. Weymaere, O. Tytgat, M. Buyle, D. Deforce, and F. Van Nieuwerburgh, "Enrichment of circulating trophoblasts from maternal blood using laminar microscale vortices," *Prenatal Diagnosis*, vol. 41, no. 9, pp. 1171–1178, 2021, doi: 10.1002/pd.5901.

[186] M. Winter *et al.*, "Isolation of Circulating Fetal Trophoblasts Using Inertial Microfluidics for Noninvasive Prenatal Testing," *Adv. Mater. Technol.*, vol. 3, no. 7, p. 1800066, 2018, doi: https://doi.org/10.1002/admt.201800066.

[187] D. R. Gossett *et al.*, "Hydrodynamic stretching of single cells for large population mechanical phenotyping," *Proc Natl Acad Sci*, vol. 109, no. 20, pp. 7630–7635, May 2012, doi: 10.1073/pnas.1200107109.

[188] S. C. Hur, A. J. Mach, and D. Di Carlo, "High-throughput size-based rare cell enrichment using microscale vortices," *Biomicrofluidics*, vol. 5, no. 2, Jun. 2011, doi: 10.1063/1.3576780.

[189] S. C. Hur, J. Che, and D. C. Di, "Microscale Laminar Vortices for High-Purity Extraction and Release of Circulating Tumor Cells.," *Methods Mol Biol*, vol. 1634, pp. 65–79, 2017, doi: 10.1007/978-1-4939-7144-2_5.

[190] C. Delteil, J. Teissié, and M.-P. Rols, "Effect of serum on in vitro electrically mediated gene delivery and expression in mammalian cells," *Biochimica et Biophysica Acta (BBA) - Biomembranes*, vol. 1467, no. 2, pp. 362–368, Aug. 2000, doi: 10.1016/S0005-2736(00)00235-2.

[191] A. M. Bowman, O. M. Nesin, O. N. Pakhomova, and A. G. Pakhomov, "Analysis of Plasma Membrane Integrity by Fluorescent Detection of Tl+ Uptake," *J Membrane Biol*, vol. 236, no. 1, pp. 15–26, Jul. 2010, doi: 10.1007/s00232-010-9269-y.

[192] D. Luo and W. M. Saltzman, "Synthetic DNA delivery systems," *Nat Biotechnol*, vol. 18, no. 1, Art. no. 1, Jan. 2000, doi: 10.1038/71889.

[193] H. Gwak, J. Kim, L. Kashefi-Kheyrabadi, B. Kwak, K.-A. Hyun, and H.-I. Jung, "Progress in Circulating Tumor Cell Research Using Microfluidic Devices," *Micromachines*, vol. 9, no. 7, Art. no. 7, Jul. 2018, doi: 10.3390/mi9070353.

[194] D. Zhang, H. Bi, B. Liu, and L. Qiao, "Detection of Pathogenic Microorganisms by Microfluidics Based Analytical Methods," *Anal. Chem.*, vol. 90, no. 9, pp. 5512–5520, May 2018, doi: 10.1021/acs.analchem.8b00399.

[195] L. Marle and G. M. Greenway, "Microfluidic devices for environmental monitoring," *TrAC Trends in Analytical Chemistry*, vol. 24, no. 9, pp. 795–802, Oct. 2005, doi: 10.1016/j.trac.2005.08.003.

[196] D. C. Duffy, J. C. McDonald, O. J. A. Schueller, and G. M. Whitesides, "Rapid Prototyping of Microfluidic Systems in Poly(dimethylsiloxane)," *Anal. Chem.*, vol. 70, no. 23, pp. 4974–4984, Dec. 1998, doi: 10.1021/ac980656z.

[197] R. O. Rodrigues, R. Lima, H. T. Gomes, and A. M. T. Silva, "Polymer microfluidic devices: an overview of fabrication methods," *U.Porto Journal of Engineering*, vol. 1, no. 1, Art. no. 1, Oct. 2015, doi: 10.24840/2183-6493_001.001_0007.

[198] G. G. Morbioli, N. C. Speller, and A. M. Stockton, "A practical guide to rapid-prototyping of PDMS-based microfluidic devices: A tutorial," *Analytica Chimica Acta*, vol. 1135, pp. 150–174, Oct. 2020, doi: 10.1016/j.aca.2020.09.013.

[199] C.-W. Tsao, "Polymer Microfluidics: Simple, Low-Cost Fabrication Process Bridging Academic Lab Research to Commercialized Production," *Micromachines*, vol. 7, no. 12, Art. no. 12, Dec. 2016, doi: 10.3390/mi7120225.

[200] H. Becker and L. E. Locascio, "Polymer microfluidic devices," *Talanta*, vol. 56, no. 2, pp. 267–287, Feb. 2002, doi: 10.1016/S0039-9140(01)00594-X.

[201] B. M. D. C. Costa, S. Griveau, F. d'Orlyé, F. Bedioui, J. A. F. da Silva, and A. Varenne, "Microchip electrophoresis and electrochemical detection: A review on a growing synergistic implementation," *Electrochimica Acta*, vol. 391, p. 138928, Sep. 2021, doi: 10.1016/j.electacta.2021.138928.

[202] D. Erickson and D. Li, "Integrated microfluidic devices," *Analytica Chimica Acta*, vol. 507, no. 1, pp. 11–26, Apr. 2004, doi: 10.1016/j.aca.2003.09.019.

[203] K. Liu and Z. H. Fan, "Thermoplastic microfluidic devices and their applications in protein and DNA analysis," *Analyst*, vol. 136, no. 7, pp. 1288–1297, Apr. 2011, doi: 10.1039/c0an00969e.

[204] C. A. Lemaire *et al.*, "Fast and Label-Free Isolation of Circulating Tumor Cells from Blood: From a Research Microfluidic Platform to an Automated Fluidic Instrument, VTX-1 Liquid Biopsy System," *SLAS TECHNOLOGY: Translating Life Sciences Innovation*, vol. 23, no. 1, pp. 16–29, Feb. 2018, doi: 10.1177/2472630317738698.

[205] J. Che *et al.*, "Classification of large circulating tumor cells isolated with ultra-high throughput microfluidic Vortex technology," *Oncotarget*, vol. 7, no. 11, pp. 12748–12760, Feb. 2016, doi: 10.18632/oncotarget.7220.

[206] V. Murlidhar, L. Rivera-Báez, and S. Nagrath, "Affinity Versus Label-Free Isolation of Circulating Tumor Cells: Who Wins?," *Small*, vol. 12, no. 33, pp. 4450–4463, 2016, doi: 10.1002/smll.201601394.

[207] J. Paredes, K. D. Fink, R. Novak, and D. Liepmann, "Self-anchoring nickel microelectrodes for rapid fabrication of functional thermoplastic microfluidic prototypes," *Sensors and Actuators B: Chemical*, vol. 216, pp. 263–270, Sep. 2015, doi: 10.1016/j.snb.2015.04.041.

[208] J. Paredes, M. Chooljian, K. Fink, and D. Liepmann, "RAPID FABRICATION METHOD FOR PLASTIC MICROFLUIDIC DEVICES WITH EMBEDDED MICROELECTRODES AND ITS APPLICATION TO ELECTROPORATION AND CELL LYSIS ON CHIP," 2014. https://www.semanticscholar.org/paper/RAPID-FABRICATION-METHOD-FOR-PLASTIC-MICROFLUIDIC-Paredes-Chooljian/eec1602b05ff9bcb997a11e5a8d1e60742755d2b (accessed Aug. 19, 2022).

[209] H. Becker and U. Heim, "Hot embossing as a method for the fabrication of polymer high aspect ratio structures," *Sensors and Actuators A: Physical*, vol. 83, no. 1, pp. 130–135, May 2000, doi: 10.1016/S0924-4247(00)00296-X.

[210] M. B. Esch, S. Kapur, G. Irizarry, and V. Genova, "Influence of master fabrication techniques on the characteristics of embossed microfluidic channels," *Lab on a Chip*, vol. 3, no. 2, pp. 121–127, 2003, doi: 10.1039/B300730H.

[211] Z. Peng, L. Gang, T. Yangchao, and T. Xuehong, "The properties of demoulding of Ni and Ni-PTFE moulding inserts," *Sensors and Actuators A: Physical*, vol. 118, no. 2, pp. 338–341, Feb. 2005, doi: 10.1016/j.sna.2004.01.042.

[212] K.-J. Byeon, K.-Y. Yang, and H. Lee, "Thermal imprint lithography using sub-micron sized nickel template coated with thin SiO2 layer," *Microelectronic Engineering*, vol. 84, no. 5, pp. 1003–1006, May 2007, doi: 10.1016/j.mee.2007.01.102.

[213] S. R. Nugen, P. J. Asiello, and A. J. Baeumner, "Design and fabrication of a microfluidic device for near-single cell mRNA isolation using a copper hot embossing master," *Microsyst Technol*, vol. 15, no. 3, pp. 477–483, Mar. 2009, doi: 10.1007/s00542-008-0694-0.

[214] N. Okamoto, F. Wang, and T. Watanabe, "Adhesion of Electrodeposited Copper, Nickel and Silver Films on Copper, Nickel and Silver Substrates," *Materials Transactions*, vol. 45, no. 12, pp. 3330–3333, 2004, doi: 10.2320/matertrans.45.3330.

[215] P. S. Kirlin, S. R. Summerfelt, and P. McIntryre, "Diffusion barriers between noble metal electrodes and metallization layers, and integrated circuit and semiconductor devices comprising same," US6320213B1, Nov. 20, 2001 Accessed: Oct. 08, 2022. [Online]. Available: https://patents.google.com/patent/US6320213B1/en

[216] A. O. Ayeleso and R. R. van Zyl, "Photocurrents obtained from a triple planar probe sensor for in situ extreme ultraviolet (EUV) radiation measurements on low Earth orbiting CubeSats," *Journal of Engineering, Design and Technology*, vol. 14, no. 3, pp. 641–651, Jan. 2016, doi: 10.1108/JEDT-05-2014-0032.

[217] E. S. Güler, *Effects of Electroplating Characteristics on the Coating Properties*. IntechOpen, 2016. doi: 10.5772/61745.

[218] J. B. Marro, T. Darroudi, C. A. Okoro, Y. S. Obeng, and K. C. Richardson, "The Influence of Pulsed Electroplating Frequency and Duty Cycle on Copper Film Microstructure and Stress State," *Thin Solid Films*, vol. 621, pp. 91–97, Jan. 2017, doi: 10.1016/j.tsf.2016.11.047.

[219] K. C. Yung, T. M. Yue, K. C. Chan, and K. F. Yeung, "The effects of pulse plating parameters on copper plating distribution of microvia in PCB manufacture," *IEEE Transactions on Electronics Packaging Manufacturing*, vol. 26, no. 2, pp. 106–109, Apr. 2003, doi: 10.1109/TEPM.2003.817722.

[220] 雷明, "Anode baffle for electroplating," CN202881424U, Apr. 17, 2013 Accessed: Aug. 20, 2022. [Online]. Available: https://patents.google.com/patent/CN202881424U/en

[221] S.-W. Kuo, H.-C. Kao, and F.-C. Chang, "Thermal behavior and specific interaction in high glass transition temperature PMMA copolymer," *Polymer*, vol. 44, no. 22, pp. 6873–6882, Oct. 2003, doi: 10.1016/j.polymer.2003.08.026.

[222] K. T. L. Trinh, D. A. Thai, W. R. Chae, and N. Y. Lee, "Rapid Fabrication of Poly(methyl methacrylate) Devices for Lab-on-a-Chip Applications Using Acetic Acid and UV Treatment," *ACS Omega*, vol. 5, no. 28, pp. 17396–17404, Jul. 2020, doi: 10.1021/acsomega.0c01770.

[223] M. M. Faghih and M. K. Sharp, "Solvent-based bonding of PMMA–PMMA for microfluidic applications," *Microsyst Technol*, vol. 25, no. 9, pp. 3547–3558, Sep. 2019, doi: 10.1007/s00542-018-4266-7.

[224] E. M. C. Hillman *et al.*, "In vivo optical imaging and dynamic contrast methods for biomedical research," *Philosophical Transactions of the Royal Society A: Mathematical, Physical and Engineering Sciences*, vol. 369, no. 1955, pp. 4620–4643, Nov. 2011, doi: 10.1098/rsta.2011.0264.

[225] C. Wang *et al.*, "In Vivo Imaging of Histone Deacetylases (HDACs) in the Central Nervous System and Major Peripheral Organs," *J. Med. Chem.*, vol. 57, no. 19, pp. 7999–8009, Oct. 2014, doi: 10.1021/jm500872p.

[226] D. Fu, T. Ye, T. E. Matthews, B. J. Chen, G. Yurtserver, and W. S. Warren, "High-resolution *in vivo* imaging of blood vessels without labeling," *Opt. Lett., OL*, vol. 32, no. 18, pp. 2641–2643, Sep. 2007, doi: 10.1364/OL.32.002641.

[227] M. O. Culjat, D. Goldenberg, P. Tewari, and R. S. Singh, "A Review of Tissue Substitutes for Ultrasound Imaging," *Ultrasound in Medicine & Biology*, vol. 36, no. 6, pp. 861–873, Jun. 2010, doi: 10.1016/j.ultrasmedbio.2010.02.012.

[228] B. W. Pogue and M. S. Patterson, "Review of tissue simulating phantoms for optical spectroscopy, imaging and dosimetry," *Journal of Biomedical Optics*, vol. 11, no. 4, p. 041102, 2006, doi: 10.1117/1.2335429.

[229] J. Hwang, J. C. Ramella-Roman, and R. Nordstrom, "Introduction: Feature Issue on Phantoms for the Performance Evaluation and Validation of Optical Medical Imaging Devices," *Biomed Opt Express*, vol. 3, no. 6, pp. 1399–1403, May 2012, doi: 10.1364/BOE.3.001399.

[230] G. N. McKay, N. Mohan, and N. J. Durr, "Imaging human blood cells in vivo with oblique back-illumination capillaroscopy," *Biomed. Opt. Express, BOE*, vol. 11, no. 5, pp. 2373–2382, May 2020, doi: 10.1364/BOE.389088.

[231] L. Huang, G. N. McKay, and N. J. Durr, "A Deep Learning Bidirectional Temporal Tracking Algorithm for Automated Blood Cell Counting from Non-invasive Capillaroscopy Videos," in *Medical Image Computing and Computer Assisted Intervention – MICCAI 2021*, Cham, 2021, pp. 415–424. doi: 10.1007/978-3-030-87237-3_40.

[232] M. Lippeveld *et al.*, "Classification of Human White Blood Cells Using Machine Learning for Stain-Free Imaging Flow Cytometry," *Cytometry Part A*, vol. 97, no. 3, pp. 308–319, 2020, doi: 10.1002/cyto.a.23920.

[233] H. J. Jawad, M. Sarimollaoglu, A. S. Biris, and V. P. Zharov, "Dynamic blood flow phantom with negative and positive photoacoustic contrasts," *Biomed. Opt. Express, BOE*, vol. 9, no. 10, pp. 4702–4713, Oct. 2018, doi: 10.1364/BOE.9.004702.

[234] S. S. Klykov, I. V. Fedosov, and V. V. Tuchin, "Cell trapping in a blood capillary phantom using laser tweezers," in *Saratov Fall Meeting 2014: Optical Technologies in Biophysics and Medicine XVI; Laser Physics and Photonics XVI; and Computational Biophysics*, Mar. 2015, vol. 9448, pp. 57–62. doi: 10.1117/12.2179976.

[235] L. Luu, P. A. Roman, S. A. Mathews, and J. C. Ramella-Roman, "Microfluidics based phantoms of superficial vascular network," *Biomed Opt Express*, vol. 3, no. 6, pp. 1350–1364, May 2012, doi: 10.1364/BOE.3.001350.

[236] C. Chen, M. Ahmed, T. Häfner, F. Klämpfl, F. Stelzle, and M. Schmidt, "Fabrication of a turbid optofluidic phantom device with tunable µa and µ's to simulate cutaneous vascular perfusion," *Sci Rep*, vol. 6, no. 1, Art. no. 1, Jul. 2016, doi: 10.1038/srep30567.

[237] C. Chen *et al.*, "Preparation of a skin equivalent phantom with interior micron-scale vessel structures for optical imaging experiments," *Biomed. Opt. Express, BOE*, vol. 5, no. 9, pp. 3140–3149, Sep. 2014, doi: 10.1364/BOE.5.003140.

[238] R. B. Saager *et al.*, "In vivo measurements of cutaneous melanin across spatial scales: using multiphoton microscopy and spatial frequency domain spectroscopy," *J Biomed Opt*, vol. 20, no. 6, p. 066005, Jun. 2015, doi: 10.1117/1.JBO.20.6.066005.

[239] S.-H. Tseng, P. Bargo, A. Durkin, and N. Kollias, "Chromophore concentrations, absorption and scattering properties of human skin in-vivo," *Opt. Express, OE*, vol. 17, no. 17, pp. 14599–14617, Aug. 2009, doi: 10.1364/OE.17.014599.

[240] F. Ayers, A. Grant, D. Kuo, D. J. Cuccia, and A. J. Durkin, "Fabrication and characterization of silicone-based tissue phantoms with tunable optical properties in the visible and near infrared domain," in *Design and Performance Validation of Phantoms Used in Conjunction with Optical Measurements of Tissue*, Feb. 2008, vol. 6870, pp. 56–64. doi: 10.1117/12.764969.

[241] L. M. Richards, S. M. S. Kazmi, J. L. Davis, K. E. Olin, and A. K. Dunn, "Low-cost laser speckle contrast imaging of blood flow using a webcam," *Biomed. Opt. Express, BOE*, vol. 4, no. 10, pp. 2269–2283, Oct. 2013, doi: 10.1364/BOE.4.002269.

[242] G. J. Greening *et al.*, "Characterization of thin poly(dimethylsiloxane)-based tissue-simulating phantoms with tunable reduced scattering and absorption coefficients at visible and near-infrared wavelengths," *J Biomed Opt*, vol. 19, no. 11, p. 115002, Nov. 2014, doi: 10.1117/1.JBO.19.11.115002.

[243] A. Bollinger, P. Butti, J.-P. Barras, H. Trachsler, and W. Siegenthaler, "Red blood cell velocity in nailfold capillaries of man measured by a television microscopy technique," *Microvascular Research*, vol. 7, no. 1, pp. 61–72, Jan. 1974, doi: 10.1016/0026-2862(74)90037-5.

[244] S. Behtaj, A. Öchsner, Y. G. Anissimov, and M. Rybachuk, "Retinal Tissue Bioengineering, Materials and Methods for the Treatment of Glaucoma," *Tissue Eng Regen Med*, vol. 17, no. 3, pp. 253–269, Jun. 2020, doi: 10.1007/s13770-020-00254-8.

[245] M. H. Kuehn, J. H. Fingert, and Y. H. Kwon, "Retinal ganglion cell death in glaucoma: mechanisms and neuroprotective strategies," *Ophthalmol Clin North Am*, vol. 18, no. 3, pp. 383–395, vi, Sep. 2005, doi: 10.1016/j.ohc.2005.04.002.

[246] D. A. Lee and E. J. Higginbotham, "Glaucoma and its treatment: A review," *American Journal of Health-System Pharmacy*, vol. 62, no. 7, pp. 691–699, Apr. 2005, doi: 10.1093/ajhp/62.7.691.

[247] B. J. Fan and J. L. Wiggs, "Glaucoma: genes, phenotypes, and new directions for therapy," *J Clin Invest*, vol. 120, no. 9, pp. 3064–3072, Sep. 2010, doi: 10.1172/JCI43085.

[248] A. M. Miltner and A. La Torre, "Retinal Ganglion Cell Replacement: Current Status and Challenges Ahead," *Developmental Dynamics*, vol. 248, no. 1, pp. 118–128, 2019, doi: 10.1002/dvdy.24672.

[249] O. of the Commissioner, "Devices Used to Process Human Cells, Tissues, and Cellular and Tissue-Based Products (HCT/Ps)," *U.S. Food and Drug Administration*, May 12, 2021. https://www.fda.gov/regulatory-information/search-fda-guidance-documents/devices-used-process-human-cells-tissues-and-cellular-and-tissue-based-products-hctps (accessed Aug. 18, 2022).

[250] S. C. Hur, T. Z. Brinckerhoff, C. M. Walthers, J. C. Y. Dunn, and D. D. Carlo, "Label-Free Enrichment of Adrenal Cortical Progenitor Cells Using Inertial Microfluidics," *PLOS ONE*, vol. 7, no. 10, p. e46550, Oct. 2012, doi: 10.1371/journal.pone.0046550.

[251] X. Lu, C. Liu, G. Hu, and X. Xuan, "Particle manipulations in non-Newtonian microfluidics: A review," *Journal of Colloid and Interface Science*, vol. 500, pp. 182–201, Aug. 2017, doi: 10.1016/j.jcis.2017.04.019.

[252] F. Tian, Q. Feng, Q. Chen, C. Liu, T. Li, and J. Sun, "Manipulation of bio-micro/nanoparticles in non-Newtonian microflows," *Microfluid Nanofluid*, vol. 23, no. 5, p. 68, Apr. 2019, doi: 10.1007/s10404-019-2232-z.